Université catholique de Louvain
Ecole Polytechnique de Louvain
(Faculté des Sciences Appliquées)
LABORATOIRE DE TÉLÉCOMMUNICATIONS
ET
TÉLÉDÉTECTION

B - 1348 Louvain-la-Neuve Belgique

Low-profile Antennas based on Aperiodic and Compact Meta-Surfaces

Rosa M Mateos Navarro

Thesis presented for the Ph.D. degree
in Applied Sciences

Ph.D. committee:

Christophe CRAEYE (UCL-TELE) - Supervisor
Isabelle HUYNEN (UCL-EMIC)
Eduard ÚBEDA (Universitat Politècnica de Catalunya)
Steven BEST (Mitre Corp.)
Emmanuel FERNANDES (Multitel)
Luc VANDENDORPE (UCL-TELE) - Chairman

August 2009

Agradecimientos

Cette thèse n'a pas été pour moi qu'une expérience professionnelle mais aussi une expérience personnelle. Elle coïncide avec un séjour en Belgique qui m'a permis de découvrir une autre petite partie du monde différente de chez moi et d'avoir vécu une expérience unique. Réaliser une thèse de doctorat à l'étranger implique une remise en question de sa façon de réfléchir et de travailler. Durant ce parcours, on rencontre des gens qui, sans se rendre compte, font partie aussi de cette aventure personnelle et que je tiens à remercier ici.

Avant tout, je voudrais remercier Christophe Craeye pour son enthousiasme dans sa thématique de recherche, le temps qu'il consacre à ses chercheurs, et les moyens qu'il met en oeuvre pour trouver des financements afin de nous permettre de finir notre thèse. Merci également aux membres de mon jury, Isabelle Huynen, Eduard Úbeda, Steven Best et Emmanuel Fernandes, pour leur commentaires constructifs. Ma reconnaissance va également à l'ESA (European Space Agency), à la Région Wallonne et à Multitel pour avoir soutenu financièrement ce travail.

Mais une thèse sans collègues de travail avec qui partager les inquiètudes, les meilleurs et les moins bons moments, n'aurait pas donné un si beau travail. Je tiens à remercier ceux qui ne sont plus là, ceux qui continuent ou qui commencent, pour leur compagnie, leur soutien et les rires partagés. Je voudrais mentioner spécialement Bertrand, Xavier (alias Raf), Lyazid, Annabelle, Judith, Belén, Onur, David, Mohieddine, Tao, Jonathan, Valéry, Cédric et Harold. Je ne voudrais pas manquer d'encourager ceux qui sont en train de faire ou de finir leur thèse et de leur témoigner la joie finale qui récompense les moments plus durs. Ne perdez pas le courage !!

Quiero mencionar también a mis compañeros del D3 de la UPC: Bea, Raquel, Pere, Txema, Jordi, Stan ..., con quienes tan buenos momentos, risas y divertimentos varios :) pasé estando en Barcelona. Gràcies Eduard per la rebuda, i pels bons riures que vam passar junts. No quiero olvidar dar las gracias a Chema (José María González) por su ayuda y el tiempo que me dedicó.

Aussi je voudrais remercier mes chèrs amis Tang Chi, Alex et Marta pour les très bons moments vécus ensemble en Belgique et leur aide précieuse dans certains moments.

Muy especialmente, quiero dedicar unas líneas a mis padres y a mi hermana para agradecerles el esfuerzo que han hecho para acostumbrarse a mi ausencia. Sé que no ha sido siempre fácil! Muchas gracias por vuestro apoyo y nuestras charlas skyperas que tanto me han ayudado, especialmente al final. Creo que una parte de esta tesis la debo a la constancia y espíritu de lucha que me habéis enseñado a tener y os lo agradezco de todo corazón.

Merci également à Gisèle et Jo pour leur accueil et aide.

Finalement, je dédie cette thèse très particulièrement à Jérôme, qui m'a autant soutenue et encouragée à la fin. Partager cette fin de thèse avec lui a été un vrai cadeau. Merci beaucoup Jérôme pour ta patience, ta compréhension et ce qu'on partage tous les jours.

Muchas gracias a todos !

Abstract

Artificial magnetic ground planes enable the placement of horizontal antennas close to the ground plane. However, their behaviour as AMCs (Artificial Magnetic Conductor) is valid only over a small frequency band. Hence, their use in wideband antenna applications remains a challenge. The antenna-AMC combination can be optimized to maximize the impedance bandwidth, thanks to the coupling between the antenna and the AMC. However, we have observed that the radiation patterns split at broadside when we work close to the AMC resonance frequency. This limits the useful operation bandwidth, i.e. the bandwidth at which good radiation and matching conditions are achieved at the same time. In this thesis, a new non-periodic structure acting as an AMC and as a leaky-wave surface at the same time has been studied and designed to recover the broadside directivity near and beyond the AMC resonance. An antenna with broadside directivity better than 9.2 dB over a 32.65% impedance bandwidth is finally presented.

This thesis also focuses on the design of a low-profile RFID tag able to work on metallic objects. We have proved that including an AMC ground plane in the tag design avoids the tag antenna to be short-circuited when it is mounted on a metallic plane. But having a compact AMC is essential to obtain a competitive RFID tag. A new AMC surface of 42.6 mm $\times$ 42.6 mm size has been designed. It supports an inductively-fed meander dipole that provides the complex input impedance required to activate the microchip terminating the tag. A prototype has been fabricated in our laboratory to measure its input impedance. Very encouraging preliminary results have been obtained. The inductive coupling effect achieved with the feeding loop of the meander dipole is preserved in presence of the AMC ground plane.

Contents

Introduction

1

1.1 Objective of the dissertation

Over the last decade, a growing interest in a new kind of periodic structures, called "metamaterials" or "meta-surfaces", has been observed. These new artificial materials exhibit many new appealing properties, not found in nature, and open many new possibilities in the domain of antenna design. An overview of these metamaterials and of their most relevant properties can be found in the next section. According to the objectives of this work, our interests in this kind of structures are focused on their use as reflectors in ground plane configurations. Special attention has been paid to their use as surface-waves free ground planes. More concretely, the goals of this work concern the design of low-profile antennas for different kinds of applications: wide-band and RFID (radio frequency identification) applications. To this end, a new aperiodic and a new compact artificial structures acting as AMC (artificial magnetic conductor) ground planes have been studied and designed. The design guidelines and numerical techniques used and developed to perform this work are described along the text of this dissertation.

1.2 Metamaterials

1.2.1 Volumes: negative-index materials

The concept of metamaterial was originally connected to materials with negative refractive index [1]. Such materials are usually referred to as negative-index materials (NIMs). The refractive index of a material provides information about the factor by which the phase velocity of waves is decreased or increased in the material w.r.t. vacuum. A negative refractive index implies propagation of waves with phase and group velocities antiparallel between them. The refractive index is related to the relative dielectric permittivity ε_r and to the relative magnetic permeability μ_r as $n^2 = \varepsilon_r \mu_r$. Regarding the definition provided by Maxwell's equations $\nabla \times E = -\mu \frac{\partial H}{\partial t}$ and $\nabla \times H = \varepsilon \frac{\partial E}{\partial t}$, the permittivity ε and permeability μ are the most relevant parameters describing the electromagnetic waves propagation within a material. Fig. 1.1 presents a materials classification according to their permittivity and permeability features. Most known materials have both positive permittivity and permeability. There also exist materials with either, but not both, ε or μ negative. However, materials with both ε and μ less than zero do not appear in nature.

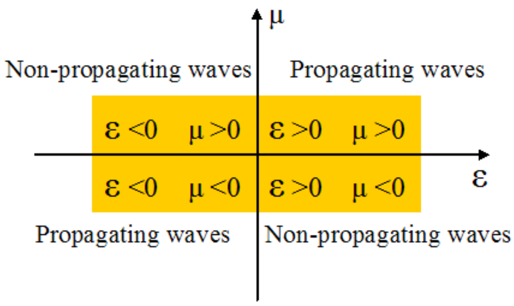

Figure 1.1 *Materials classification depending on their permittivity and permeability characteristics.*

It is revealed that when both ε and μ are negative (i.e. $\varepsilon_r < 0$ and $\mu_r < 0$), a negative square root for n has to be chosen [7]. Victor G. Veselago, a Russian physicist from the Lebedjev Physical Institute in Moscow, theoretically studied plane wave propagation in materials with simultaneously negative permittivity and permeability [7]. His study showed that the direction of the Poynting vector (energy flow) is antiparallel to the direction of phase velocity. It means that the wavevector $\vec{k}$, describing the propagation of waves in the media, forms a left-handed set with the vectors $\vec{E}$ and $\vec{H}$. NIMs are then often named as left-handed materials (LHMs) or double negative (DNG) materials.

According to Snell's law, a wave coming from a medium with a refractive index n_1 and an incident angle i with respect to the normal to the interface with a second medium with refractive index n_2, will be refracted in the second medium with an angle r. The following relation holds:

$$n_1 \cdot sin(i) = n_2 \cdot sin(r) \tag{1.1}$$

When one of the media has a negative refractive index, the refracted wave will make a negative angle r with the normal to the interface between the two media (Fig. 1.2). This phenomenon is called negative refraction and offers the possibility of creating perfect lenses, as described by John Pendry in [8]. A slab of material with a negative index of refraction n_2, placed in vacuum, is capable of perfect focusing, meaning that it can perfectly reproduce the electromagnetic radiation from the source plane to the image plane (see Fig. 1.3). A double focusing effect makes the rays transmitted through the slab of thickness d, to travel from a source point located at a distance d_s from the slab, to a focus point situated at $d_f = d - d_s$ from the slab.

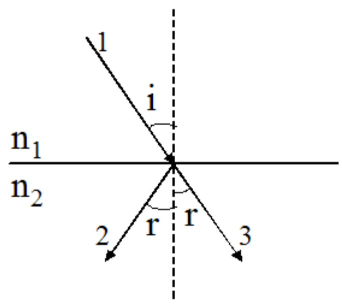

Figure 1.2 *Refraction of a ray passing through the boundary between two media. 1: Incident ray. 2: Refracted ray when the second medium is left-handed. 3: Refracted ray when the second medium is right-handed.*

A media with either ε or μ negative, enables amplification of the evanescent waves related to the source radiation, which improves the resolution of the image at the focus point [8]. Then, a negative-refractive-index slab with

$n_2 = -1$ (i.e. $\varepsilon_r = -1$ and $\mu_r = -1$) allows to achieve subwavelength focusing through the amplification of evanescent fields [8]. Subwavelength resolution and sensitivity to various slab parameters are studied in [9].

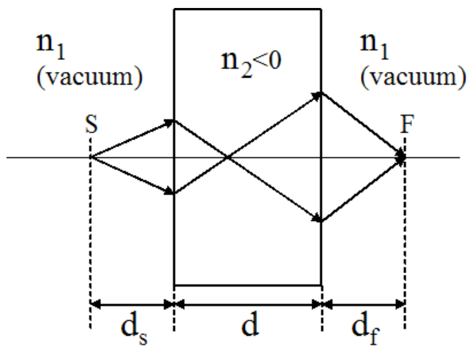

Figure 1.3 *Passage of a ray through a slab of negative refractive index material of thickness d. S: source plane. F: focusing or image plane.*

1.2.2 Surfaces: artificial materials

The concept of metamaterial has been broadened over the last several years. Metamaterials are nowadays widely known to be artificial structures presenting unusual properties, not found in natural materials. In electromagnetism, more concretely, there has been a huge interest, over the last few years, in creating artificial materials that allow to expand the range of electromagnetic properties already present in natural structures. In electromagnetism, metamaterials usually consist of periodic structures composed of electrically conducting elements with inductive and capacitive characteristics, which determine their electromagnetic properties. Different uses of such artificial materials have been found and studied in various areas. Bandgap structures against surface waves [4], [11], novel microwave guides [13], artificial magnetic conductor (AMC) ground planes [4], [14], leaky-wave structures [15] or slow-wave media [16], are some of their related applications that can be found in the literature. Concerning the goals of this work, our interest in metamaterials is focused on their use as ground planes for obtaining low-profile antenna designs, for wideband and RFID applications.

At the appropriate spacing, the presence of a ground plane below an antenna redirects the back-radiation into the opposite direction, improving the antenna gain and protecting possible electronic circuits on the backside of the antenna. The most straightforward ground plane is the Perfect Electric Conductor plane (PEC), simply made of a large metallic sheet.

PECs show some disadvantages when used as ground planes in antenna applications. The first drawback, directly connected with our goals, appears when considering low-profile designs because they do not allow radiating elements with horizontal currents to lay directly adjacent to the ground plane. In this case, image currents cancel the currents in the antenna, resulting in a very poor radiation. It occurs as result of the fact that the opposite polarity of the image currents reduces the antenna's radiation resistance, which approaches zero as the spacing approaches zero [3]. This results in a high impedance mismatch and reduced radiation efficiency [3]. To solve the problem, the antenna must be located at a certain distance (typically 0.25λ) above the ground plane to work properly, which increases the total height of the antenna. Another way to overcome the problem is to use an antenna with a high free space impedance [3], so that when it is closely spaced to the PEC ground plane it exhibits a matched impedance. More important is then the increase in the reactive energy surrounding the antenna when it is placed close ($< 0.25\lambda$) to the ground plane, which produces an increase in Q (quality factor) and a corresponding decrease in bandwidth [3]. This is the single major issue to resolve.

Secondly, PECs support surface currents that radiate into free space when reaching the edge or corner of a finite ground plane (the real case). The combined radiation from the antenna and the ground plane edges results in a kind of multi-path interference, seen as ripples in the radiation pattern. It is worth noting here that the size of a finite PEC ground plane has more effect on the antenna pattern if the antenna is a TM mode radiator -perpendicular to the ground plane-. For the case of a TE mode radiator -parallel to the ground plane-, the pattern does not really change as much with a change in the ground plane size.

Some of these problems would be solved if one could create Perfect Magnetic Conductors (PMC), which cannot naturally be found in nature. They are the electromagnetic dual surfaces with respect to perfect electric conductors.

In antenna and microwave applications it is mainly the reflection characteristics at the surface of such materials that are of interest. This is the reason why the differences in the electrical properties between an infinitely large PEC and PMC are described along the present work by the reflection coefficient for a uniform incident plane wave. The magnitudes of the reflection coefficient for both cases are the same and equal to one, while the phase differs by $180\,^{\circ}$. It means that if a PEC exhibits a reflection coefficient of $\Gamma = -1$, the reflection coefficient of a PMC is $\Gamma = +1$, meaning, in the latter case, that the phase of the reflected wave is $0\,^{\circ}$ compared to the phase of the incident wave. To summarize, a surface that shows a $180\,^{\circ}$ phase shift compared to a PEC surface and, at the same time, completely reflects an incident plane wave effectively can be considered as a PMC surface.

An equivalent way of looking at PMC surfaces is that the image of the antenna currents flowing parallel to a PMC are in phase with the currents in the antenna. This allows to use PMCs as reflectors in antennas and to place radiating elements very close to the PMC, even laying flat almost against the ground plane, resulting in low-profile antennas.

- Artificial magnetic conductors (AMC)

As described above, special ground planes, alternative to the traditional PEC, are necessary for achieving low-profile antenna configurations. As a PMC appears as an open circuit seen from the incoming plane wave, one way to design an artificial PMC (AMC) is to provide an open circuit condition by means of periodic structures. Each element of the periodic pattern provides an equivalent L and C parallel connection that changes the surface impedance. At the frequencies where the periodic loading becomes an open circuit, a magnetic surface is created. The phenomenon can be interpreted as a parallel LC resonance, at which the surface impedance is very high.

When looking at the reflection phase of an AMC surface vs. frequency (Fig. 1.4), at frequencies lower than the resonance frequency it is π, and the structure behaves like an ordinary flat metal surface - the surface has low impedance -. The reflection phase slopes down, and crosses zero at the resonance frequency (f_0 in Fig. 1.4). Above it, the phase returns to $-\pi$. In the literature, the bandwidth of an AMC is often defined as the frequency range where the reflection phase of an incident wave is within $0 \pm \pi/2$ [4], which theoretically corresponds to the frequency band where the AMC behaves as a PMC. However, when an antenna is placed above a finite AMC and is tuned to work near the AMC resonance, the surface waves travelling along the AMC may radiate when reaching the edges of the finite AMC, distorting the radiation patterns of the design with additional lobes and nulls at some angles. Yang and Rhamat-Samii propose to work in the range where the reflection phase of the AMC is $\pi/2 \pm \pi/4$ [17], which is said to be the useful operation bandwidth, that is the frequency band where good matching and radiation conditions are achieved at the same time. Then, one could question the importance of the reflection phase of the AMC surface in terms of the antenna impedance matching [5]. As seen in [17] or [5] the antenna can be matched over a wide range of reflection phase values, but with narrow bandwidths when working close to the PEC phase condition [5], i.e. 180°. Then, for bandwidth reasons, the designs presented in this dissertation have been tuned to work near the AMC resonance f_0, that is in the $0 \pm \pi/2$ reflection phase range, and some solutions have been proposed to overcome the radiation difficulties encountered in this operation range.

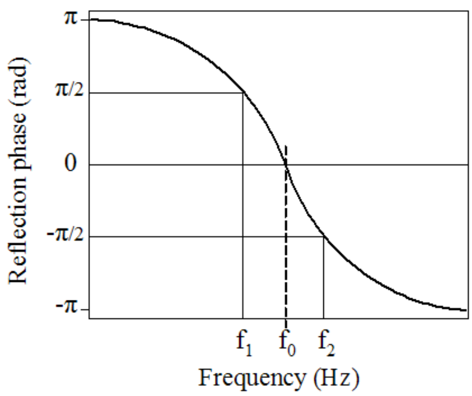

Figure 1.4 *Reflection phase curve related to an AMC surface.*

Many different designs of AMC surfaces have been recently developed. Multiband AMC surfaces are proposed in [18]. A genetic algorithm (GA) technique is applied to optimize the geometry and dimensions of the studied AMC designs. In [19], a very compact AMC, stable with respect to the incidence angle, is presented. It can be seen as a modified version of the well-known Jerusalem cross design [20]. An analytical study on the stability of the AMC resonance of a high impedance surface (HIS) is presented in [20]. Further work on a 2-layer configuration of Jerusalem crosses is provided in [21]. Compact AMC designs based on spiral geometries are studied in [21]. A four-arm spiral unit cell is finally designed to eliminate the cross-polar backscattering produced by the other spiral shapes proposed. Measurements of the PMC behaviour of an AMC surface based on spiral resonators are provided in [22].

- Electromagnetic bandgap structures (EBG)

Some AMC surfaces show other interesting properties that also make them suitable to act as special ground planes. As said above, AMCs provide high impedance surface (HIS) conditions [4]. If moreover, they can suppress surface currents, the interference of surface waves with the main radiation, as well as the associated edge effects on finite surfaces, can be reduced. The main characteristic of electromagnetic bandgap (EBG) structures is to forbid the propagation of the electromagnetic waves whose frequency lies within a specific frequency range, often called *bandgap* or *stopband*. A TM mode radiator (a vertical antenna) on a high-impedance ground plane, showing EBG characteristics, can produce a smoother radiation pattern than a similar antenna on a conventional metallic ground plane, with less power wasted in the backward direction [4].

Surface waves appear in many situations involving antennas. As already mentioned, ground planes are widely used in the design of antennas in order to redirect half of the radiation into the opposite direction, improving the gain. In addition to space waves, the back-grounded substrate can support surface waves. In the case of a finite ground plane, surface waves propagate until they reach an edge or corner, where they can radiate into free space. The combined radiation from the antenna and the ground plane edges results in ripples, additional lobes or nulls at various angles in the radiation pattern [4]. In the case of multiple antennas sharing the same ground plane, surface currents can cause undesired mutual coupling.

Then, the design of structures capable of avoiding the propagation of surface waves has awakened the interest of many research groups. To this end, electromagnetic band gap (EBG) structures have been designed for surface-wave suppression applications [4], [11], [23], [24].

1.2.3 AMC-EBG surfaces studied

As mentioned in the previous section, when using AMC surfaces as ground planes, surface waves may appear. Regarding the objectives of our work, surface waves are going to be a problem to design wideband antennas. Hence, we are interested in studying surfaces showing EBG characteristics that enable the suppression of surface waves. In the present section, some of the probably most known surfaces that combine AMC and EBG properties are presented. Their simple shapes also make them suitable for the design of RFID tags.

- AMC surface with vias: mushroom structure

Mushroom high-impedance electromagnetic surfaces have been studied by Sievenpiper [4]. In this approach, the proposed high-impedance surface consists of a lattice of hexagonal metallic plates, connected to a solid metal sheet by vertical conducting vias (see Fig. 1.5).

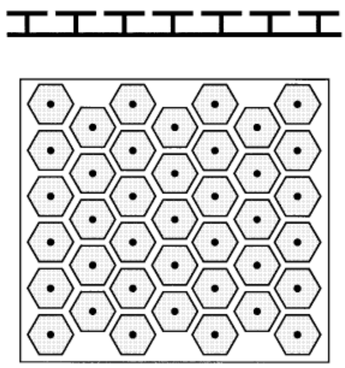

Figure 1.5 *Copied from [4]: Cross section (top) and top view (bottom) of a high-impedance surface that consists of a lattice of solid metal plates, connected to a solid metal sheet by vertical conducting vias.*

Unlike many grounded substrates, this surface does not support propagating surface currents in a certain frequency band, thanks to the presence of vias, and it also reflects electromagnetic waves with no phase reversal. It behaves as an artificial magnetic conductor in the frequency range where it also exhibits the EBG property. It is worth noticing that the resonance frequency and bandwidth of the AMC depends on the characteristic parameters of the surface. A parametric study is provided in [17] and it is shown that if the structure is made thinner, a higher resonance frequency, together with a bandwidth reduction, are obtained. When the gap width is increased, both the frequency band position and its bandwidth increase. It is also evidenced in [17] that bigger patches or higher substrate permittivities result in a smaller bandwidth and resonance frequency.

Antennas have been demonstrated to take advantage of the two important properties mentioned in the previous paragraph [4]. An improvement in the radiation pattern of a simple vertical monopole has been demonstrated, and a new class of low-profile antennas has been introduced, in which the radiating element lies directly adjacent to the AMC ground plane. One disadvantage of the presented structure is that the need for grounding vias makes it more difficult and more expensive to fabricate than other planar AMC structures. Hence, in order to simplify the fabrication process, other planar structures, not including vias, [12], [13] have been proposed.

- AMC surface without vias: array of closely spaced patches

An artificial PMC using a simple patch array has been studied in [12]. As seen in Fig. 1.6 the structure consists of square patches located on a homogeneous epoxy substrate backed by a ground plane. Such surface is demonstrated to have reflection properties that are in analogy with a perfect magnetic conductor, within a certain bandwidth. The resonant frequency of this AMC surface depends on the size of the patches, as well as on the separation between them [12]. Like for the mushroom structure, an increase of the patch length results in a lower resonant frequency. Larger gap widths produce a resonance shift towards higher frequencies. On the other hand, when increasing the thickness or the permittivity of the supporting substrate, the resonant frequency decreases [12].

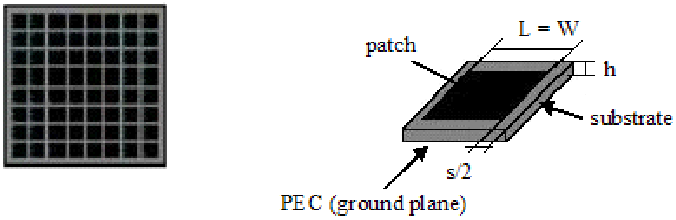

Figure 1.6 *To the left, a top view of the patch array surface with the dashed line showing a single element [12]. To the right, a more detailed drawing of the square patch single element from the whole array.*

The drawback, and main difference w.r.t. the mushroom AMC structure, is that the array of patches does not necessarily exhibit AMC and EBG features within the same frequency band [14]. This can deteriorate the benefits of the surface as an AMC. A further study provided in [14] evidences two different resonant phenomena related to the AMC and EBG properties. On the one hand, the AMC operation occurs mainly by virtue of the resonance of the cavity between the periodic patches array and the ground plane. On the other hand, the EBG characteristic appears more as a result of the array resonance. Nevertheless, from a study on the effect of the array parameters on both the EBG and AMC properties [14], it is shown how both properties can be tailored to appear over the same frequency band, by varying the array periodicity.

1.3 Outline of the dissertation

The work presented in this thesis can be divided in two different parts. Chapters 2, 3, 4 and 5 are dedicated to the design of wideband low-profile antennas with the help of AMC ground planes. Chapter 6 concerns the design of AMC surfaces for RFID applications.

Chapter 2 discuses the possibility of designing wideband low-profile antennas with the help of a ground plane with a reflection coefficient whose phase increases with frequency. Based on the Foster's reactance theorem, it is shown that this kind of ground plane does not exist except for strong cross-polar conditions. The possibility of using an AMC ground plane supporting an antenna with horizontal currents is also considered. Due to the narrow bandwidth of AMC surfaces, their application remains a challenge for wide-band antennas. A planar bow-tie dipole antenna placed above two different AMC surfaces (a mushroom-like EBG and an array of patches) is studied. Before going deeply into this study, some validations are done in order to ensure the correct use of the simulation tools used: the commercial Feko software and the MoM code developed at the UCL. The study of the planar bow-tie dipole placed close to an AMC shows that the directivity at broadside decreases considerably (the patterns split at broadside) near and beyond the frequency at which the AMC behaves as a PMC (the AMC resonance). This limits the useful achievable bandwidth for an antenna placed above an AMC. In order to have some insight on the coupling between the antenna and the AMC, the fields near the AMC surface, giving special attention to evanescent waves, are analysed.

Chapter 3 proposes to replace the planar bow-tie dipole studied in Chapter 2 by a double-dipole antenna placed vertically above the AMC surface, in order to overcome the problem of splitting patterns observed for the bow-tie antenna case. The double-dipole antenna consists of two dipoles, initially of different lenghts, stacked above the AMC ground plane. The largest dipole, resonating at the AMC resonance, will be placed close to the surface to obtain a lower profile than if it was placed on top. A chronologic description of the design work carried out towards a final design is provided, in order to give some insight into the antenna principle and into the phenomena observed.

The solution proposed in Chapter 3, to solve the splitting patterns problem, does finally not help to recover the broadside directivity over the whole input impedance bandwidth. Then, in Chapter 4, a new non-periodic surface acting as an AMC and, at the same time, as a leaky-wave structure is designed. Before presenting the new structure, the problem of poor broadside directivity when working close to the AMC resonance, is exposed in detail for the double-dipole antenna presented in Chapter 3, but this time placed horizontally above the AMC to reduce the profile of the design. A review of the theory related to the computation and representation of the modal features of a periodic structure will help us to understand and to interpret the modal analysis shown in the following sections for the original and the new AMC ground planes. Such analysis provides a better physical understanding of why the new structure helps to solve the broadside directivity problems, exposed at the beginning of the chapter. A final design, with its input-impedance and radiation performances, is presented at the end of the chapter.

Chapter 5 presents a very simple method developed to compute the periodic Green's function when dealing with complex phase shifts. It is worth noting that it can also be applied for real phase shifts, as needed to deal with leaky waves. First, we expose the problems found when trying to evaluate the periodic Green's function for complex phase shifts. After describing the new proposed method, a parametric analysis is provided. It gives an idea of the accuracies achievable for both complex and real phase shifts. The new method is combined with the UCL code, which is based on the numerical MoM technique, to carry out the modal analysis presented in Chapter 4. It has especially been developed to study the leaky waves supported by the AMC surfaces studied in Chapter 4.

Chapter 6 is dedicated to the design of AMC ground planes for RFID applications. More concretely, the goal is to design a new tag working on metallic objects without being short-circuited. First, a review of the operation principles of passive RFID systems is presented. Then, the usefulness of including an AMC in the tag design to isolate it from a metallic plate is proven experimentally. The following sections present the design of an AMC-tag. It consists of an inductively-fed meander dipole placed above an AMC ground plane. Once the meander dipole is proved to operate correctly above the AMC surface, the dimensions of the new tag are reduced to make the design competitive as a RFID tag, taking into account the low resistance and high capacitance of the RFID chip. Finally, measurements concerning the input-impedance of a final prototype fabricated in our laboratory are provided.

Conclusions are finally drawn in Chapter 7.

Wideband low-profile antennas

2

Some antennas exhibit a particularly large impedance bandwidth. This is the case for self-similar antennas [27], i.e. antennas whose enlarged copy is equal to the original antenna. The input impedance of such antennas is theoretically frequency-independent. This is generally the case for TEM horns, if they are bigger than λ, so the ends are not visible to the wave. Self-complementary antennas [28] are flat metallic antennas whose metallized and non-metallized surfaces are complementary. In this case, the input impedance is also theoretically frequency-independent and equal to half the free-space impedance. This principle can be extended to arrays. In this case, the elements of the array are not self-complementary, but the array structure is [29]. This is the case of the planar bicone antennas. The only limitations to the bandwidth of such antennas are, in the high-frequency end, the fabrication accuracy of the feed region and, more importantly, in the low-frequency end, the lateral size of the antenna or array. Roughly speaking, the impedance changes rapidly when the wavelength becomes larger than the antenna or array.

A major problem with such antennas is that they radiate on both sides of the antenna plane, and the feeding structure may also disrupt the self-complementarity of the structure [30]. A primitive solution consists of introducing a parallel ground plane at some distance from the antenna, to concentrate the radiation in one side. Unfortunately, the image of the antenna in the ground plane supports currents with opposite sign. In the direction perpendicular to the antenna plane, both antennas will radiate in opposition when the distance between antenna and ground plane is a multiple of half a wavelength (i.e. a multiple of the wavelength between the antenna and its image). This leads to a rapid variation of the radiation resistance versus frequency. In the case of infinite self-complementary arrays, the radiation resistance is exactly equal to zero when the distance to the ground plane is a multiple of half a wavelength.

A large research effort has recently been produced for the development of special ground planes. The impedance bandwidth of the antennas may be extended by developing three-dimensional ground planes whose phase center tends to move away from the antenna when the frequency decreases, such that the antenna-to-ground plane distance remains close to a quarter wavelength over a relatively broad range of frequencies. This requires a reflection coefficient with a phase that increases with frequency. In the following, we will show that these kinds of ground planes do not exist, except for strong cross-polar conditions, and we will shortly comment the consequences of this observation on the possible configuration of wideband antennas and arrays.

2.1 Extension of the Foster's reactance theorem

The Foster reactance theorem is known for its application to lossless one-port systems. It will be extended here to the case of the reflection of a plane wave by a perflectly conducting periodic ground plane. We will do this by referring to Section 5.2 of *Microwave Engineering* [31]. First, the Maxwell equations are derived with respect to frequency. The result is then used to obtain the following equation:

$$\nabla \cdot \left(\vec{E}^{\star} \times \frac{\partial \vec{H}}{\partial \omega} + \frac{\partial \vec{E}}{\partial \omega} \times \vec{H}^{\star} \right) = -j \left(\epsilon \left| \vec{E} \right|^2 + \mu \left| \vec{H} \right|^2 \right) \tag{2.1}$$

where the fields and media properties are denoted by $\vec{E}$ (electric field), $\vec{H}$ (magnetic field), ϵ (permittivity) and μ (permeability). Using the divergence theorem on the left-hand side and identifying the terms on the right-hand side with the stored electric and magnetic energies, we get [31]:

$$\oint_S \left(\vec{E}^{\star} \times \frac{\partial \vec{H}}{\partial \omega} + \frac{\partial \vec{E}}{\partial \omega} \times \vec{H}^{\star} \right) \cdot \hat{n}\, dS = -4\, j \left(W_e + W_m \right) \tag{2.2}$$

where the normal to the surface S is pointing outside the integration volume.

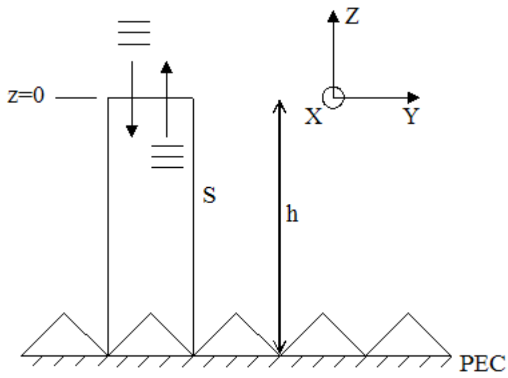

Figure 2.1 Special ground plane and surface of integration for the application of Foster's theorem.

In the following, we will assume that the fields are due to a plane wave normally incident on the periodic ground plane. The considered volume corresponds to a rectangular volume including a unit cell of the structure. The height h of the volume is large enough to have vanishing evanescent fields on the top surface (see Section 2.2.5). We assume that the element spacing between cells of the ground plane does not allow grating lobes, such that there is just one reflected propagating plane wave. Based on the periodicity of the structure, it can be shown that the integrals over the lateral surfaces vanish ($\vec{E}^\star \times \frac{\partial \vec{H}}{\partial \omega}$ and $\frac{\partial \vec{E}}{\partial \omega} \times \vec{H}^\star$) are identical on opposite points, while the unit normals are opposite). The integral over the bottom surface is zero because of the presence of the back-grounding PEC ground plane. The integral over the top surface is estimated below.

The $\hat{z}$ direction is normal to the ground plane, and the origin is located at height H. The incident and reflected electric fields are written as:

$$\vec{E}_i = \hat{x}\, E^\circ\, e^{jkz} \tag{2.3}$$
$$\vec{E}_r = \left(\hat{x}\,\Gamma_x + \hat{y}\,\Gamma_y\right)\; E^\circ\, e^{-jkz} \tag{2.4}$$

Energy conservation imposes that $|\Gamma_x|^2 + |\Gamma_y|^2 = 1$.

The total fields in the $z = 0$ plane can be written as:

$$\vec{E} = E^\circ\; \left(\hat{a}_x\,(1+\Gamma_x) + \hat{a}_y\,\Gamma_y\right) \tag{2.5}$$

$$\vec{H} \quad = \quad E^{\circ} \left(-\hat{a}_x \, \Gamma_y + \hat{a}_y \, (-1 + \Gamma_x) \right) / \eta \tag{2.6}$$

Equation (2.2) can be written as:

$$\frac{|E^{\circ}|^2 \, A}{\eta} \left[(1 + \Gamma_x^{\star}) \, \frac{d\Gamma_x}{d\omega} + \Gamma_y^{\star} \, \frac{d\Gamma_y}{d\omega} + (-1 + \Gamma_x^{\star}) \, \frac{d\Gamma_x}{d\omega} + \Gamma_y^{\star} \, \frac{d\Gamma_y}{d\omega} \right] = -4 \, j \, (W_e + W_m) \tag{2.7}$$

where A is the surface of the unit cell and η is the free-space impedance.

Writing the copolarized and cross-polarized reflection coefficients as $\Gamma_x = g_x \, e^{j \, \phi_x}$ and $\Gamma_y = g_y \, e^{j \, \phi_y}$ (with $g_x^2 + g_y^2 = 1$), we obtain:

$$2 \, j \, g_x^2 \, \frac{d \, \phi_x}{d\omega} + 2 \, j \, g_y^2 \, \frac{d \, \phi_y}{d\omega} + 2 \, g_x \, \frac{dg_x}{d\omega} + 2 \, g_y \, \frac{dg_y}{d\omega} = -4 \, j \, (W_e + W_m) \, \frac{\eta}{|E^{\circ}|^2 \, A} \tag{2.8}$$

$$g_x^2 \, \frac{d \, \phi_x}{d\omega} + g_y^2 \, \frac{d \, \phi_y}{d\omega} - j \, \frac{1}{2} \, \frac{d}{d\omega} (g_x^2 + g_y^2) = -(W_e + W_m) \, \frac{2 \, \eta}{|E^{\circ}|^2 \, A} < 0 \tag{2.9}$$

$$g_x^2 \, \frac{d \, \phi_x}{d\omega} + g_y^2 \, \frac{d \, \phi_y}{d\omega} = -\frac{(W_e + W_m)}{P_{in}} < 0 \tag{2.10}$$

where P_{in} is the power per unit cell of the incident plane wave.

Eq. (2.10) tells us that when there is no important cross-polarized component, the phase of the reflection coefficient must decrease with frequency, that is $\frac{d \, \phi_x}{d\omega} < 0$. A necessary condition for having a positive slope, i.e. $\frac{d \, \phi_x}{d\omega} > 0$, is a ground plane generating a strong cross-polarized component with a very strong negative slope of its phase versus frequency, that is $\frac{d \, \phi_y}{d\omega} << 0$. This would also mean that the two reflected polarization components have an opposite phase trend versus frequency, which would lead to a rapid change versus frequency in polarization state of the reflected field. Then, eq. (2.10) evidences that it is not possible to design a ground plane with a reflection coefficient whose phase increases with frequency, except for strong cross-polar conditions.

2.2 Wideband low-profile antennas based on AMCs

As mentioned in the previous section, low-profile wideband antennas might be obtained by designing a ground plane with a reflection coefficient whose phase increases with frequency. By extending the Foster's theorem to the reflection of a plane wave produced by a periodic perfectly-conducting ground plane, it has been shown that, except for strong cross-polar conditions, such ground planes do not exist. Alternatively, antennas supporting horizontal currents, flowing at larger heights for lower frequencies, may be good candidates for wideband antennas, because the source currents may be maintained at about half a wavelength from their image in the ground plane. AMC ground planes, which can support antennas placed horizontally above them, are an interesting potential solution for designing low-profile wideband antennas. Given the relatively narrow bandwidth of artificial magnetic surfaces (AMCs), their application remains a challenge for wideband antennas. As most AMC structures are known to be narrowband, the antenna-AMC combination can be optimized to obtain broad bandwidths. The present section describes the components (TEM horn antenna and AMC structures) that may compose a low-profile wideband design. The work here presented is performed with the help of the FEKO [6] software, a full-wave simulation tool also based on the Method of Moments (MoM). Some validations have been firstly performed by comparing intermediate results with the ones obtained with a code developed at the UCL [35], [36] (based on the MoM numerical technique). This has allowed us to ensure the correct use of Feko, and thus, to ensure the validity of the results obtained in the rest of our study. Both the FEKO software and the UCL code are based on the Method of Moments (MoM) technique [32], which is described in Section 2.2.1. In the UCL approach, the periodicity of the structures is taken into account with the help of periodic Green's functions (Section 2.2.2). After carrying out the validations, the combination TEM horn-AMC has been studied. The performances obtained, together with the most relevant phenomena observed due to the interaction between the antenna and the AMC have been analysed.

2.2.1 The Method of Moments

Let us consider an arbitrarily shaped conducting object, with its surface S discretized in non-overlaping sub-regions on which equivalent currents will be approximated. A very common discretization consists of triangles, but in order to reduce the number of sub-regions, the MoM code used in the context of this work includes also the possibility to use rectangular sub-regions. The current induced on the structure analyzed may be approximated by means of a set of N known basis functions $\vec{J}_n$ associated to the discretization. It can then be represented as the vector sum of the surface currents on the sub-regions in which S is divided:

$$\vec{J}(\vec{r}\,') = \sum_{n=1}^{N} x_n \vec{J}_n(\vec{r}\,') \tag{2.11}$$

The basis functions used in our numerical simulation code are the ones presented by Rao, Wilton and Glisson in [46], and denoted as RWG basis functions. The x_n's are the unknown current coefficients to be determined in the solution of the MoM problem.

An electric field $\vec{E}^i$ is incident on the conducting surface. It induces on the surface current $\vec{J}$, which produces a scattered (radiated) electric field $\vec{E}^s$. The scattered electric field $\vec{E}^s$ can be computed as follows:

$$\vec{E}^s = -j\omega\vec{A} + \frac{1}{j\omega\epsilon\mu}\nabla\nabla\cdot\vec{A} \tag{2.12}$$

with the magnetic vector potential defined as

$$\vec{A}(\vec{r}) = \mu \iint_S G_r(\vec{r})\vec{J}(\vec{r}\,')dS\,' \tag{2.13}$$

where μ and ϵ are the permeability and permitivity of the surrounding medium, $\vec{r}$ and $\vec{r}\,'$ denote the observation and source point locations on S, and $G_r(\vec{r})$ is the Green's function.

The integral equation for the surface current induced on a conducting scatterer is derived from the boundary conditions on the electric field. The electric field integral equation (EFIE) is obtained by enforcing the total tangential electric-field component to be zero on the conducting surface:

$$\vec{E}|_{tan} = \vec{E}^s|_{tan} + \vec{E}^i|_{tan} = 0 \tag{2.14}$$

$$\vec{E}^s|_{tan} = -\vec{E}^i|_{tan} \tag{2.15}$$

Substitution of the surface current (2.11), the magnetic vector potential (2.13) and the scattered electric field (2.12) into (2.15) yields a discretized version of the integral equation (EFIE), which depends on the unknown coefficients x_n.

$$[-j\omega + (1/j\omega\epsilon\mu)\nabla\nabla\cdot] \iint_S \mu\, x_n\, \vec{J}_n(\vec{r}\,')\, G_r(\vec{r})\, dS\,' = -\vec{E}^i \tag{2.16}$$

The EFIE can be solved by the Galerkin method [46], which consists of testing the integral equation with the help of the same set of basis functions used to approximate the surface current $\vec{J}$. A $N \times N$ system of linear equations results in the form

$$Z_{mn}\, x_n = -E^i_m \qquad m, n = 1, 2, ..., N \tag{2.17}$$

where Z_{mn} is a $N \times N$ matrix, called the MoM impedance matrix, and x_n and E^i_m are column vectors of length N. The elements of Z_{mn} result from the convolution between the basis and testing functions, with the Green's function (periodic in the study presented in this dissertation). The mth element of the excitation vector E^i_m is obtained as the inner-product of the incident electric field $\vec{E}^i$ with the testing function $\vec{J}_t$,

$$E^i_m = \iint_S \vec{E}^i \cdot \vec{J}_t(\vec{r}\,')\, dS \tag{2.18}$$

The incident field $\vec{E}^i$ is often taken as resulting from a Dirac-delta voltage source defined over the basis function composing the source. Hence, on transmission, only one elemenent of the excitation vector E^i_m will be non-zero. On reception, $\vec{E}^i$ corresponds to the fields associated with an incident plane wave. By combining (2.16) and (2.18), the impedance matrix Z_{mn} in (2.17) can be written as:

$$Z_{mn} = \iint_S \vec{J}_t(\vec{r}\,')[-j\omega + (1/j\omega\epsilon\mu)\nabla\nabla\cdot\,] \iint_S \mu\, x_n\, \vec{J}_n(\vec{r}\,')\, G_r(\vec{r})\, dS'\, dS, \tag{2.19}$$

which can be evaluated analytically.
Once the impedance matrix Z_{mn} is known, the current coefficients x_n can be obtained and useful information about the behavior of the scatterer, such as input impedance, input return loss or radiation patterns, can be provided.

2.2.2 Periodic Green's function computation

The periodic Green's functions are nothing else than a description of the fields radiated by a periodic array of current sources. Different formulations of the periodic Green's function are introduced in this section. Some of them are combined in Chapter 5 to obtain a new simple way to compute the periodic Green's function for complex propagating constants, as we have dealed with leaky waves in Chapter 4.

2.2.2.1 Spatial formulation

Let us consider an array of point sources infinite along $\hat{x}$ and $\hat{y}$ diretions. The related spatial Green's function can be written as

$$G_r(\vec{r}) = \sum_{n=-\infty}^{\infty} \sum_{m=-\infty}^{\infty} \frac{e^{-jkR_{mn}}}{4\pi R_{mn}} e^{-jm\psi_x} e^{-jn\psi_y} \tag{2.20}$$

where k is the free space wave number, and R_{mn} is the distance between the observation point $\vec{r} = (x, y, z)$ and the mnth source point $\vec{r}\,' = (md_x, nd_y, 0)$:

$$R_{mn} = \sqrt{(x - md_x)^2 + (y - nd_y)^2 + z^2} \tag{2.21}$$

The phase shift between adjacent elements in the x and y directions are denoted by ψ_x and ψ_y, respectively. They are related to the corresponding propagating constants, k_x and k_y, through $\psi_x = k_x\, d_x$ and $\psi_y = k_y\, d_y$. For radiation into or reception from visible space, we have:

$$\psi_x = kd_x \sin\theta \cos\phi \tag{2.22}$$

$$\psi_y = kd_y \sin\theta \sin\phi \tag{2.23}$$

where the pair (θ, ϕ) represents the incidence angles.
This spatial summation converges very slowly for most observation positions. Then, a faster formulation based on planar and cylindrical waves can been exploited [44].

2.2.2.2 Spectral formulation: sum of plane waves

It can be shown [45] that the spectral domain Green's function can be expressed as a sum of plane waves:

$$G_r(\vec{r}) = \frac{1}{2jd_x d_y} \sum_{m=-\infty}^{\infty} \sum_{n=-\infty}^{\infty} \frac{e^{-jk_x^m\, x} e^{-jk_y^n\, y} e^{-jk_z^{mn}\, |z|}}{k_z^{mn}} \tag{2.24}$$

with the following definitions for the wavenumbers :

$$k_x^m = \frac{\psi_x}{d_x} + m\,\frac{2\,\pi}{d_x} \tag{2.25}$$

$$k_y^n = \frac{\psi_y}{d_y} + n\,\frac{2\,\pi}{d_y} \tag{2.26}$$

$$(k_z^{mn})^2 = k^2 - (k_x^m)^2 - \left(k_y^n\right)^2 \quad \text{with} \quad \mathcal{I}m\,\{k_z^{mn}\} < 0\,, \tag{2.27}$$

where k is the free-space wavenumber, d_x and d_y are the spacings along $\hat{x}$ and $\hat{y}$, respectively, and ψ_x and ψ_y are the corresponding phase shifts.
This spectral formulation converges rapidly as long as $z \neq 0$ (called the "off-plane" case). This occurs because, as m and n increase, the plane-wave response changes from propagating waves to exponentially decaying evanescent waves. It is worth noticing that waves are propagating if (k_x^m, k_y^n) lie within a circle of radius k. When $z \simeq 0$ (the "on-plane" case), the convergence is slower because the exponential decay occurs with an exponent near zero. To overcome this problem, another spectral formulation, based on cylindrical waves, can be used.

2.2.2.3 Spectral formulation: sum of cylindrical waves

Let us first consider an array of point sources infinite only along the $\hat{x}$ direction (linear infinite array). The associated spatial Green's function is expressed as follows:

$$G_r(\vec{r}) = \sum_{m=-\infty}^{\infty} \frac{e^{-jkR_{mn}}}{4\pi R_{mn}} e^{-jm\psi_x} \tag{2.28}$$

where R_{mn} is in this case

$$R_{mn} = \sqrt{(x - md_x)^2 + y^2 + z^2} \tag{2.29}$$

As shown in [44], such Green's function can be expressed via the zero-order Hankel function of second kind $H_0^{(2)}$,

$$G_r(\vec{r}) = G(R, x) = \frac{1}{4jd_x} \sum_{m=-\infty}^{\infty} e^{-jk_m x} H_0^{(2)}(\gamma_m R) \tag{2.30}$$

where

$$R = \sqrt{y^2 + z^2} \tag{2.31}$$

$$\gamma_m^2 = k^2 - k_m^2 = k^2 - \left(\frac{\psi_x}{d_x} + m\frac{2\pi}{d_x}\right)^2 \tag{2.32}$$

For indices m leading to real values of γ_m ($\gamma_m^2 > 0$), we obtain propagating cylindrical waves described by the Hankel functions $H_0^{(2)}$. It is interesting to observe that the number of these waves corresponds to the number of main and grating lobes that appear in the visible region along $\hat{y}$. For an imaginary value of γ_m ($\gamma_m^2 < 0$), the Hankel function becomes a rapidly decaying modified Bessel function of the first kind (Eq. 2.33), which represents evanescent cylindrical waves,

$$H_0^{(2)}(\gamma_m R) = H_0^{(2)}(-j\alpha R) = \frac{2j}{\pi} K_0(\alpha R) \tag{2.33}$$

with attenuation coefficient $\alpha = \sqrt{-\gamma_m^2}$ real and positive.
For observation points far from the x axis, the summation converges rapidly. Contrary, for observation points close to the x axis, the convergence is slower because in this case, the summation does not benefit from the exponentially decaying behavior of the evanescent waves (like in the "on-plane" case for the plane-waves formulation).

The doubly periodic array of point sources can be seen as the superposition of an infinite number of infinite linear arrays along $\hat{x}$. Thus, the Green's function related to a planar infinite array of sources can be seen as the infinite superposition of the Green's functions associated to the infinite linear arrays along $\hat{x}$, with a phase shift ψ_y between successive linear arrays along the $\hat{y}$ direction. The expression for the doubly periodic Green's function then writes:

$$G_r(\vec{r}) = G(x, R_p) = \frac{1}{4jd_x} \sum_{p=-\infty}^{\infty} e^{-jp\psi_y} \sum_{m=-\infty}^{\infty} e^{-jk_m x} H_0^{(2)}(\gamma_m R_p) \tag{2.34}$$

where

$$\begin{aligned} R_p &= \sqrt{(y - pd_y)^2 + z^2} && (2.35) \\ \gamma_m^2 &= k^2 - k_m^2 = k^2 - \left(\frac{\psi_x}{d_x} + m\frac{2\pi}{d_x}\right)^2 && (2.36) \end{aligned}$$

Acceleration techniques can be applied [44] for accelerating the computation of the propagating part of the periodic Green's function G_r (the evanescent part converges exponentially by definition). However, despite the proposed accelerations, such computation can still be too time consuming. To overcome this problem, the Green's function is tabulated in a 3-D table of limited size, after extraction of its singularity. When the Green's function has to be evaluated, an interpolation technique is used on the values stored in the table, enabling a difficult-to-beat computation time.

2.2.3 Low-profile antenna elements and validations

The present section describes the components that may compose a low-profile wideband design: a TEM horn antenna and an AMC structure. Initially, we have focused our study on basic TEM horn antennas since they are known to be wideband thanks to their self-similar structure. Two different surfaces have been used as AMC: an array of patches on a dielectric substrate [12] and a mushroom-like ground plane [17]. Some validations are provided to ensure the correct use of the simulation tools employed in this dissertation: the Feko software [6] and the UCL code [35], [36].

- TEM Horn antenna

TEM horn antennas consist of a pair of triangular conductors forming a V structure that supports TEM waves. They are completely characterized by three parameters (Fig. 2.2) : s is the length of the antenna measured from the feeding point to a corner of the plate, φ is the angular width of each plate, and β is the angular separation between the two plates.

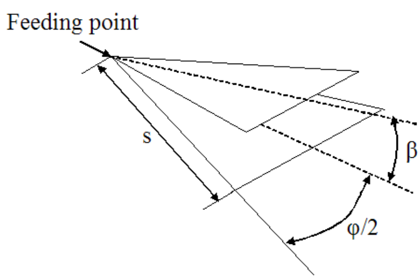

Figure 2.2 TEM horn antenna and its characteristic parameters.

When the antenna becomes infinitely long ($s \rightarrow \infty$), the characteristic impedance (Z_c) of the antenna can be defined. This is the impedance of the TEM mode along the infinite structure and it only depends on the angles φ and β. It means that Z_c is independent of frequency, and it is equal to $\eta/2$ (η being the free-space impedance) in the case of a self-complementary shape (φ = 90° and β = 180°). A graph with the relationship between the angles φ and β, and the characteristic impedance of the antenna can be found in [33]. For an antenna of finite length, but reasonably long with respect to the operating wavelength, the characteristic impedance of the antenna is a good approximation to the input impedance (Z_{in}) of the antenna [33]. In order to validate this statement, the input impedance of a TEM horn antenna with $Z_c = 100\,\Omega$ (φ = 47.30° and β = 20°) is calculated in [33] as a function of the electrical length, s/λ. Fig. 2.3 contains such Z_{in}, which is computed by using the feeding scheme shown in Fig. 2.5b. The input impedance is calculated at the location labeled T as $Z_{in} = V_T/I_T$. It is observed in Fig. 2.3 that for antennas at which $s/\lambda > 3$ the agreement between Z_c and Z_{in} is very good. Thus, by choosing the right values of φ and β, the input impedance can be chosen so that the antenna is matched according to the design requirements.

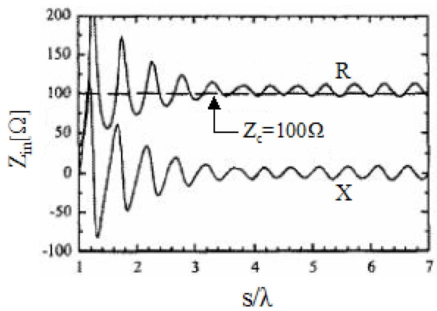

Figure 2.3 Copied from [33]: input impedance versus electrical length of the φ = 47.30° and β = 20° horn antenna.

We have tried to model, with the FEKO software, the same TEM horn antenna as the one simulated in [33]. The input impedance obtained is plotted in Fig. 2.4. The results are quite close to the expected values shown in [33] (see Fig. 2.3), a resistance around $100\,\Omega$ and an imaginary part around $0\,\Omega$. Furthermore, the zoom presented in the right column of Fig. 2.4 shows a good convergence for electrical lengths close to 3, as it was expected. This means that qualitatively, the results obtained with FEKO are good. However, some differences are observed when comparing the results from Fig. 2.3 and Fig. 2.4. They mainly differ from each other in terms of peak values, oscillation frequency and resonances. In [33], slightly lower peaks are obtained and a little shift of the resonances to higher frequencies is observed.

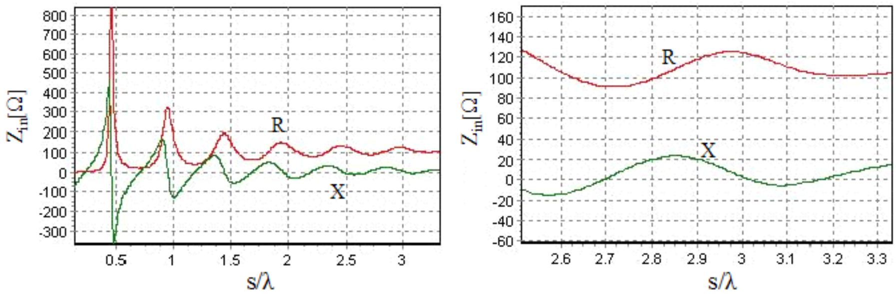

Figure 2.4 Input impedance versus electrical length of the φ = 47.30° and β = 20° horn antenna obtained with Feko.

One might expect differences between the results provided in [33] (Fig. 2.3) and the ones obtained with FEKO (Fig. 2.4), because the feed representation used is not the same for both cases. Fig. 2.5a shows the feed considered in the Feko computations, a delta-gap voltage source applied at the common edge between the two plates of the horn. In that case, the input impedance is obtained by direct calculation on the source. A two parallel-plate transmission line is proposed in [33] to feed the antenna. The feeding scheme is shown in Fig. 2.5b. Delta-gap voltage sources V_s are applied at the location marked S on both plates. The input impedance is calculated at the location labeled T and is then given by $Z_{in} = V_T / I_T$.

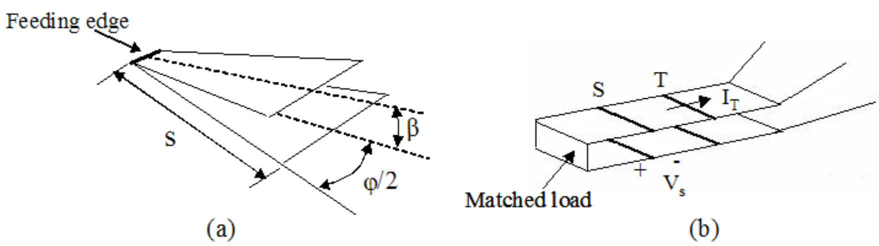

Figure 2.5 Details of the feeding schemes used to excite the TEM horn antenna: (a) Feko model (b) copied from [33]: model used in [33].

In order to valide the results obtained with Feko, we have analyzed the accuracy of our simulations making higher-density meshes and cross-validating with simulations obtained with the UCL code, a MoM code developed at our laboratory. Fig. 2.6 presents two different meshes applied near the feed. The mesh at the left is the one used in the previous simulations and the one to the right is the thinner new one. Fig. 2.7 compares the input impedances obtained with both meshes. A very good agreement is observed.

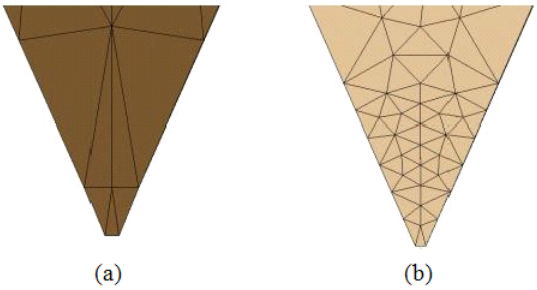

Figure 2.6 Meshes near the feed region used in the simulations of the φ = 47.30° and β = 20° TEM horn.

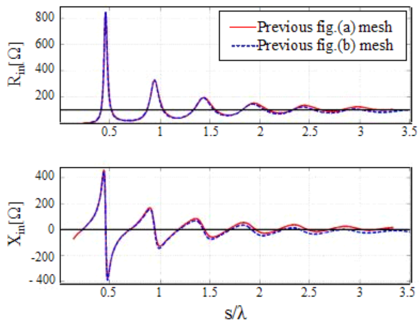

Figure 2.7 Input impedance versus electrical length of the φ = 47.30° and β = 20° horn antenna obtained with the meshes illustrated in Fig. 2.6.

Before continuing with the design of the low-profile antenna, a second validation to ensure the accuracy of the results obtained with the delta-gap feeding scheme has been done. The Z_{in} of a self-complementary antenna (φ = 90° and β = 180°) has been computed. As expected and shown in Fig. 2.8, oscillations around $\eta/2 \simeq 188\,\Omega$ have been obtained as well as a good convergence for $s/l > 3$. Moreover, a very good agreement is observed when comparing the results to the ones obtained with the UCL code (see Fig. 2.9). Then, the simple feeding scheme applied in the Feko simulations is chosen to carry out the rest of the study.

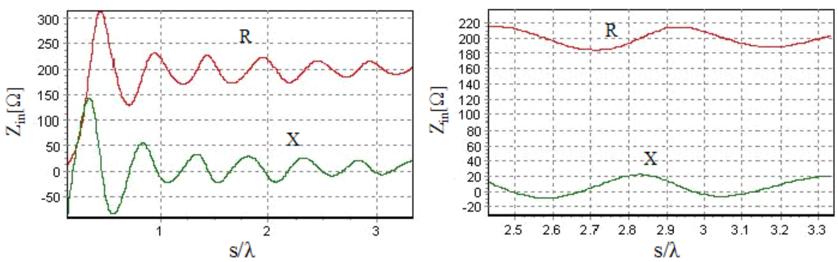

Figure 2.8 Input impedance versus electrical length of a self-complementary antenna computed with our feeding scheme.

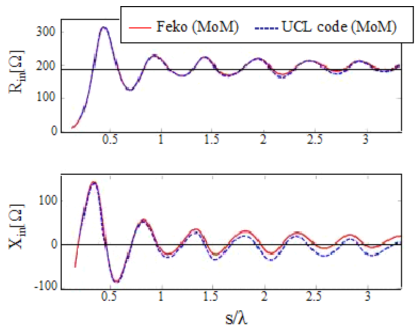

Figure 2.9 Input impedance versus electrical length of a self-complementary antenna ($\varphi = 90°$ and $\beta = 180°$), obtained with two different codes: Feko software and UCL code.

- AMC ground planes

Two different surfaces have been used as AMCs: a N×N array of square patches [12] and the mushroom-like electromagnetic band-gap (EBG) ground plane studied in [17]. A schematic representation of each surface is provided in Fig. 2.10. Both consist of a lattice of square metal patches placed at a certain distance from a metallic sheet. In the case of the mushroom structure the patches are connected to the back metal sheet by means of conducting vias, which are supposed to suppress the surface waves that may travel along the structure. The spacing between the patches g is 0.5 mm, while the length W of the patches is 36 mm. The length h and radius of the mushroom vias are equal to 1 mm and 0.125 mm, respectively. A dielectric substrate can fill the space between the plates and the ground plane. As stated in [17], the higher the permittivity of the substrate, the lower the operational band of the AMC. Thus, we have replaced the dielectric by the air ($\epsilon_r = 1$).

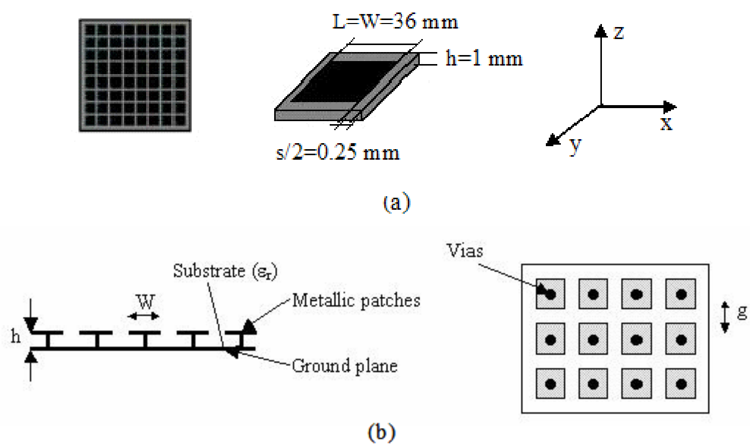

Figure 2.10 Reference geometry for the AMCs under study: (a) an array of square patches [12](b) a mushroom structure [17].

The Feko software has been used to determine the phase of the reflection coefficient associated with the AMC surfaces under study. To this end, the surface is illuminated by a plane wave polarized along y, incident from broadside, and the scattered E-fields are computed at a certain distance above the reflector. In a post-processing step carried out with Matlab, the reflection coefficient is computed from those scattered fields, knowing that the incident field corresponds to a plane wave. By correcting for the phase difference introduced by the height at which the fields are calculated, the reflection coefficient is obtained just on the plane that contains the AMC patches.

Before characterizing the surfaces under study, we have studied the dependence of the reflection coefficient phase characteristic on the AMC size and the height at which the fields are computed. Fig. 2.11 provides the results obtained for the AMC consisting of an array of square patches. In the case of Fig. 2.11(a), the fields have been computed at 1 cm above the reflector, and the phase of the reflection coefficient versus frequency is shown for different sizes of the AMC surface. The AMC dimensions do not affect very much the surface behavior. Only for the 2x2 reflector, where the surface is small enough to exhibit truncation effects at a 1 cm distance, a shift is observed. Fig. 2.11(b) also depicts the phase of the reflection coefficient versus frequency, but at different distances from a 6x6 reflector. At small distances, very close to the surface, the phase curve becomes distorted, as it can be seen for the 2mm case in Fig. 2.11(b). The same happens when the distance is high enough to obtain significant truncation effects of the finite AMC structure. So, the computation of the reflection coefficients provided in this work is performed from the fields computed at a distance between $\lambda/8$ and λ, neither too close nor too far from the AMC surface. It is important to notice, that the field computed with Feko to obtain the reflection coefficient, contains the evanescent waves scattered by the ground plane (see Section 2.2.5). These evanescent waves are going to alter the PMC behavior of the AMC surface. As seen, the results obtained for the phase of the reflection coefficient depend on the distance at which the fields are computed. Thus, the performances obtained for an antenna put close to an AMC structure will also depend on the proximity of the antenna to the AMC surface (Section 2.2.4). It is worth noting here that at small distances to the surface, the antenna performance is a function of the near-field interaction between the antenna and the surface.

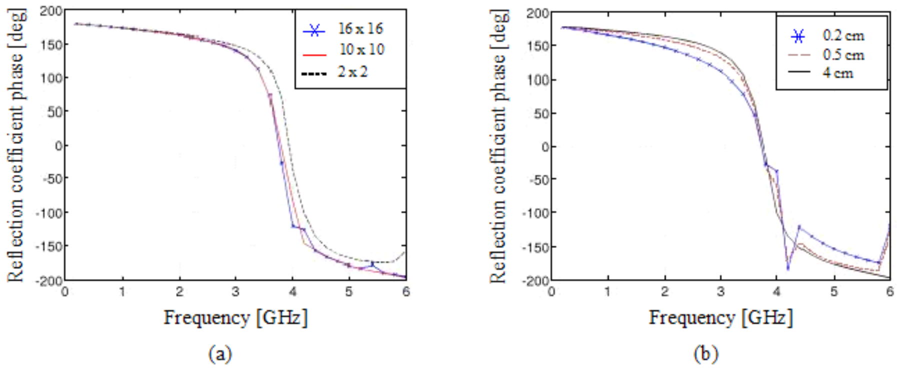

Figure 2.11 (a) Phase behavior of the reflection coefficient at 1 cm from several NxN elements AMC structures. (b) Phase behavior of the reflection coefficient at different distances from a 6x6 AMC.

Fig. 2.12 compares the reflection coefficient phase characteristic of both the array of patches AMC and the mushroom-like EBG structures shown in Fig. 2.10. We can see that both AMC surfaces, with or without vias, resonate at the same frequency, i.e. 3.7 GHz.

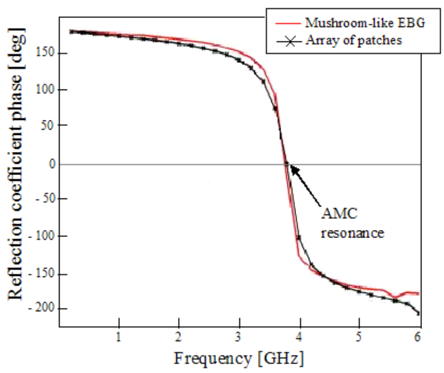

Figure 2.12 Reflection coefficient phase curve for a patches array AMC and a mushroom-like EBG structure, both resonating at 3.7 GHz.

Some validations have been carried out for the mushroom-like EBG structure. We have tried to reproduce some of the results provided in the Yang and Rahmat-Samii paper [17]. The free space wavelength at 12 GHz λ_{12GHz} is used in [17] as a reference length to define the dimensions of the different structures studied in it. The EBG structure used has now the following dimensions: a patch width of $0.12\lambda_{12GHz}$, a gap width of $0.02\lambda_{12GHz}$ and radius of the vias equal to $0.005\lambda_{12GHz}$. The space between the patches and the ground plane is filled with air. The distance between the patches and the metal sheet is equal to $0.04\lambda_{12GHz}$. A finite ground plane with $\lambda_{12GHz} \times \lambda_{12GHz}$ size is used. The phase of the reflection coefficient for the mushroom-like structure with the new dimensions has been computed. Fig. 2.13 shows the results presented in [17], and the ones obtained from our simulations. A 6x6 finite structure has been modeled with Feko and an infinitely periodic mushroom with the UCL code. The left picture in Fig. 2.13 shows the phase computed in [17] for dif-

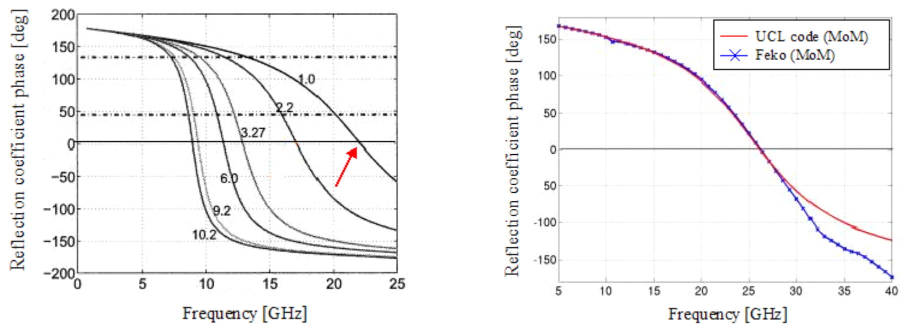

Figure 2.13 To the left, reflection coefficient phase for different substrate permittivities [17]. To the right, reflection coefficient phase computed with Feko and the UCL code, for a mushroom structure without dielectric.

ferent substrate permittivities. The right plot shows the reflection coefficient phase obtained with the Feko and the UCL codes for the mushroom structure described above. A significant shift of the AMC resonance to higher frequencies is observed when comparing the results from [17] with those obtained with Feko. However, a very good agreement is observed in terms of the curve slope and the AMC resonant frequency if we look at the results from Feko and the UCL code. It is at the highest frequencies that the two graphics differ from each other. It is worth noting that in the case of the UCL code, the propagating wave of the scattered electric field is isolated from the evanescent waves to compute the reflection coefficient, which is not the case for the Feko computations. The reflected field computed with Feko contains the evanescent waves scattered by the ground plane, which can alter the PMC behavior of the AMC surface. This is probably the phenomenon observed in Fig. 2.13 for the highest frequencies in the right picture. In Chapter 4 we will see that strong surface waves propagate on the AMC at around 35 GHz, which corresponds to the frequencies region where the reflection phase curves to the right in Fig. 2.13 differ from each other.

In addition to the validations presented here, some measurements concerning the phase of the reflection coefficient of an AMC consisting of an array of patches have also been carried out, and they confirm the validity of the results obtained with Feko. Such measurements are related to the work done in view of the design of the RFID tag based on the use of an AMC ground plane and they are shown in Section 6.3.3. Thus, despite the differences observed w.r.t. the Yang and Rahmat-Samii paper [17] (concerning the EBG mushroom surface) and the Lee and Smith contribution [33] (referring to the TEM horn), we consider the Feko software a reliable simulation tool and it has been used for carrying out the study presented in this dissertation.

2.2.4 Planar bow-tie dipole above an AMC

The different components described in Section 2.2.3 have been combined in order to create the whole antenna configuration. After chosing the TEM horn parameters, a ground plane is added below the horn antenna to see its effect on bandwidth and on radiation performances. A flat TEM horn antenna (i.e. β=180°) is chosen to reduce the profile of the design, which turns the TEM horn into a planar bow-tie dipole antenna. The use of a PEC is expected to reduce the impedance bandwidth but to improve the directivity achieved when it is placed close to the bow-tie dipole ($d < \lambda/4$, considering the AMC resonant frequency). So, the PEC is replaced by an AMC, and its effect on the impedance bandwidth and directivity performances is studied. It is worth noting that the distances d provided here refer to the total height of the design, i.e. from the bottom ground plane of the AMC to the planar bow-tie dipole. This gives a clear idea about the profile of the design under study.

- Input impedance characteristics

First of all, appropriate values of the angles φ and β have been chosen for the TEM horn antenna described in Section Section 2.2.3, in order to find the best trade-off between useful bandwidth and low-profile requirements. The angular separation β between the plates of the horn antenna plays an important role in the low-profile aspect of the complete configuration. Then a flat antenna, i.e. β=180°, is chosen and a parametric study of φ has been performed [34]. As mentioned before, a β=180° turns the TEM horn into a planar bow-tie dipole. The return loss coefficient w.r.t. 50Ω has been analyzed in the absence of a ground plane for a bow-tie antenna resonating around 1 GHz. A maximum value (16.10%) is reached around φ equal to 70°. This is then the value used to continue the study here presented. Nevertheless, it should be adjusted in the final configuration to optimize the final performances achieved.

Fig. 2.14 presents the input reflection coefficient of the planar bow-tie dipole (β=180°, φ=70°) placed at 1 cm distance from an ideal infinite PEC, a 4×4 mushroom-like EBG and an AMC consisting of an array of 6×6 patches. The ground plane below the patches of the AMC surfaces is also infinite. It is worth noticing that the results obtained with a 4×4 or a 6×6 AMC (with or without pins) were very similar in terms of input impedance bandwidth. The length of the antenna is equal to 1.5 cm to make it resonate at 3.7 GHz (the resonant frequency of the AMCs described in Section 2.2.3).

The input reflection coefficient is also provided when the antenna is at 3 cm from the different ground planes (see Fig. 2.15). It is clearly evidenced that the closer the antenna is to the PEC, the worse is the behavior in terms of bandwidth. For a distance d of 1 cm, which corresponds to $d < \lambda/4$ at the AMC resonance, the S_{11} does not even reach -10 dB. When adding the AMCs at distances close to the antenna, i.e. $d < \lambda/4$, the bandwidth behavior is improved with respect to the PEC case as was expected. However, many unexpected oscillations around 4 GHz are observed. If we compare Figs. 2.14 and 2.15, it is seen that the further the antenna is from the AMCs the fewer oscillations are obtained.

So, it has been shown that an AMC ground plane is useful in terms of impedance bandwidth when putting the antenna close to the ground plane.

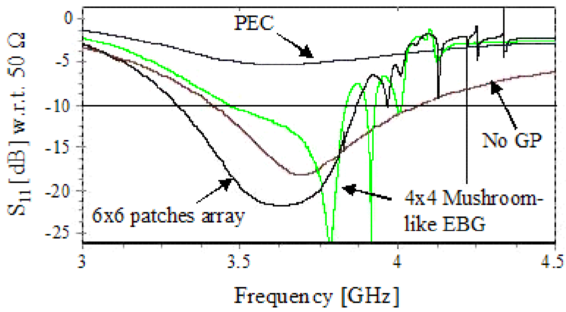

Figure 2.14 Input reflection coefficient for a planar bow-tie dipole antenna placed at 1 cm from a PEC, a mushroom-like EBG structure and an array of patches AMC.

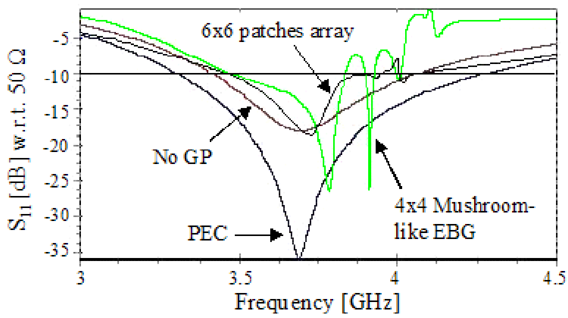

Figure 2.15 Input reflection coefficient for a planar bow-tie dipole antenna placed at 3 cm from a PEC, a mushroom-like EBG structure and an array of patches AMC.

However, the closer it is, the more oscillations we obtain near the AMC resonant frequency. In order to know more about these oscillations, the Z_{in} and the input reflection coefficient have been computed when placing the antenna at 1cm from a patches array AMC of different sizes. From Fig. 2.16, it is observed that the bigger the AMC, the more oscillations and peaks appear around 4 GHz. This is visible in both impedance and reflection coefficient forms. And as already evidenced before, the closer to the AMC the more oscillations observed. So, these oscillations may be due to resonances of the whole antenna-AMC structure.

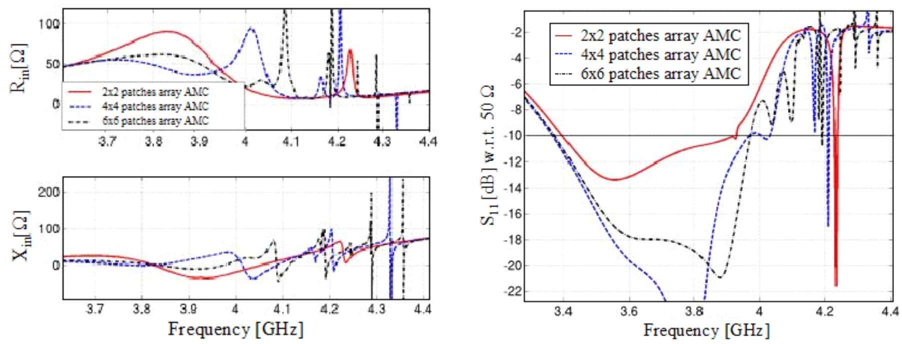

Figure 2.16 Input impedance (left) and input reflection coefficient (right) for a planar bow-tie dipole antenna located at 1 cm from an array of patches AMC of different sizes.

- Radiation performances

In order to study the radiation performances achievable when an antenna is backgrounded by an AMC, the directivity in the θ=0°, ϕ=0° direction has been plotted as a function of frequency for the planar bow-tie dipole (β=180°, φ=70°) alone and when putting it at 1cm ($d < \lambda/4$ at the AMC resonance) and 3cm ($d > \lambda/4$ considering the AMC resonance) from a PEC, the mushroom-like EBG and the array of patches AMC.

In Figs. 2.17 and 2.18, a directivity improvement is clearly evidenced when adding a ground plane on the backside of the antenna. When comparing the directivity obtained with the three different ground planes, we observe that the directivity decreases considerably if AMC ground planes are used. It is

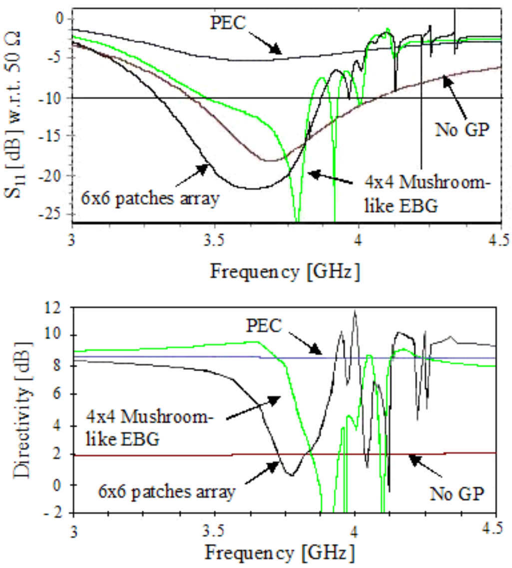

Figure 2.17 Input reflection coefficient (top) and broadside directivity (bottom) for a planar bow-tie dipole located at 1 cm from a PEC, a mushroom-like EBG structure and an array of patches AMC.

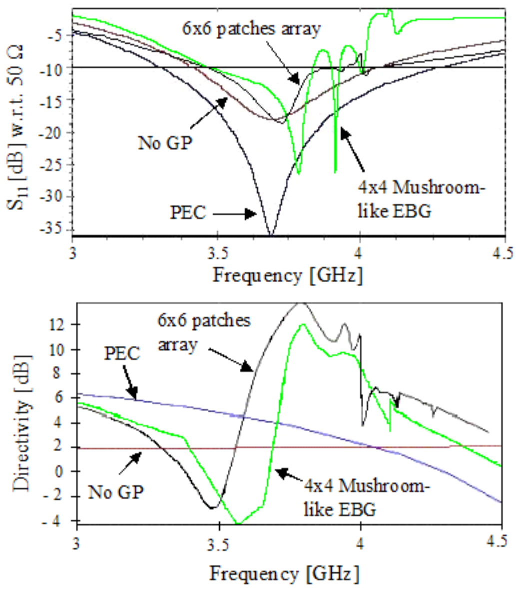

Figure 2.18 Input reflection coefficient (top) and broadside directivity (bottom) for a planar bow-tie dipole located at 3 cm from a PEC, a mushroom-like EBG structure and an array of patches AMC.

observed in Fig. 2.17 that the directivity decreases near and beyond the AMC resonance (3.7 GHz). Oscillations in the directivity also appear to the right of the useful input impedance operating bandwidth. If the bow-tie antenna is put further from the ground planes, at 3cm concretely in Fig. 2.18, less oscillations in the directivity curve are observed, as happens with the input reflection coefficient, and better directivity values may be achieved in the useful input impedance bandwidth (see Fig. 2.18). In Fig. 2.18, it can be seen that the directivity increases to 12 dB in a certain frequency range. Such directivity values are bigger than the maximum ones achievable with a PEC ground plane, that is 9 dB (see Fig. 3.31 or [3]). This is due to the fact that the distribution of reactive fields -related to the surface currents- across the surface of the AMC ground plane causes an increase in the effective area, and therefore an increase in directivity.

Figs. 2.17 and 2.18 also include the input reflection coefficient S_{11} in order to see if there is a concordance between the bands where a good reflection coefficient and directivity are achieved. We observe that good directivity values are not obtained in the whole useful input impedance bandwidth. Moreover, in contrast to the S_{11} behavior, the directivity improves with the distance of the bow-tie antenna to the AMC structures. Thus, a trade-off between directivity and impedance bandwidth requirements should be found.

2.2.5 Evanescent waves above an AMC surface

As mentioned and seen in Section 2.2.4, the performances achieved when an antenna is placed above an AMC depend on the distance at which the antenna is from the AMC surface. It is worth noticing that an AMC structure acts as PMC only for plane propagating waves, and for a limited range of incidence angles [37], which is not a fair approximation for an antenna close to an AMC. A further study about the fields near the AMC surface, with special attention given to evanescent waves, has been carried out and is presented in the next section. It has been shown that the reactive fields (evanescent waves) are stronger near the resonant frequency. So, they will certainly affect the reactance of an antenna placed above the AMC surface. In Section 2.2.4, a study on the bandwidth achieved for a flat horn antenna placed above an AMC ground plane of different dimensions has been presented. Some unexpected oscillations appear just to the right of the useful operating band. It has been seen that the bigger the AMC finite structure the more oscillations observed. A 2x2, 4x4 and 6x6 AMC were tested (left graph in Fig. 2.19). We have repeated the same simulations for an 8x8 AMC in order to verify this effect. Fig. 2.19 provides the results obtained. More oscillations are clearly evidenced when increasing the number of patches composing the AMC structure.

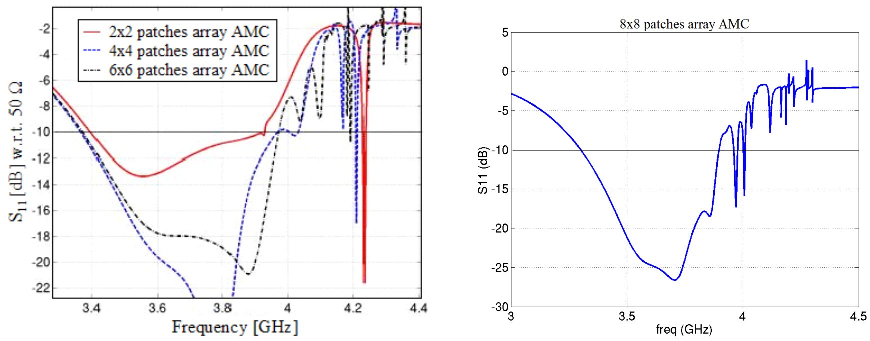

Figure 2.19 Input reflection coefficient for a flat, φ=70°, horn antenna above an AMC of different sizes. To the left, some results presented in Section 2.2.4. To the right, a verification for an 8 × 8 surface.

The presence of evanescent waves, and hence, reactive fields, near the AMC has not been analyzed in detail before. In this section, we present an effective numerical method to carry out a modal analysis in the infinite-array approach. Strong reactive fields, with a non-negligible vertical component, at the resonant frequency are evidenced. The same effects are observed for a finite array, in which evanescent waves are reflected by the edges, resulting in strong array truncation effects at the resonance. This work may lead to the establishment of new design criterion for artificial ground planes devoted to low-profile antennas.

2.2.5.1 Infinite AMC surface under study

The MoM code developed at the UCL [35], [36] has been used to compute the modes composing the E-field above an infinitely periodic structure. An infinite array of square patches has been studied. Its unit cell is shown in

Fig. 2.20. The spacing between patches is 0.5 mm, while the length of the patches is 19.5 mm. The patches are located 1.57 mm above the ground plane. The space between the patches and the ground plane is in this case filled with air, i.e. no dielectric substrate is used. The surface is illuminated by a plane wave polarized along $\hat{y}$, incident from broadside. Fig. 2.20 contains the phase of the reflection coefficient versus frequency for the propagation mode. The resonance, where the phase crosses 0 degrees, is 5.54 GHz. Here below, the propagating and successive evanescent modes above the surface, computed at different distances from the AMC for the resonant frequency, are identified.

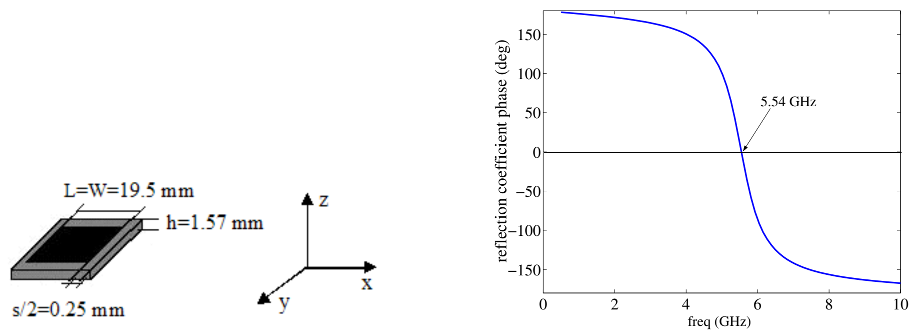

Figure 2.20 Reference geometry for a unit cell of the AMC under study (left). Phase behavior of the reflection coefficient computed at 1cm from an infinite AMC (right).

2.2.5.2 Numerical method applied

As has been shown in Section 2.2.2.2, the electric fields above an infinitely periodic surface can be written as a superposition of plane waves with horizontal and vertical wavenumbers: $k_x^m = \frac{\psi_x}{a} + m\frac{2\pi}{a}$, $k_y^n = \frac{\psi_y}{b} + n\frac{2\pi}{b}$ and $(k_z^{mn})^2 = k^2 - (k_x^m)^2 - \left(k_y^n\right)^2$, with $\mathcal{I}m\left\{k_z^{mn}\right\} < 0$. The free-space wavenumber is represented by k, a and b are the spacings along $\hat{x}$ and $\hat{y}$, respectively, and ψ_x and ψ_y are the corresponding phase shifts.

The electric field scattered by each mn-order harmonic can be computed as:

$$\vec{E}_{mn}(\vec{r}) = \frac{1}{j\omega\epsilon}\left(k^2\vec{A}_{mn}(\vec{r}) + \nabla\nabla\cdot\vec{A}_{mn}(\vec{r})\right), \qquad (2.37)$$

where $\vec{A}_{mn}(\vec{r})$ is the 2-D periodic magnetic vector potential (Section 2.2.2.2):

$$\vec{A}_{mn}(\vec{r}) = \iint \vec{J}(\vec{r}\,') \, \frac{e^{-jk_x^m(x-x')}\, e^{-jk_y^n(y-y')}\, e^{-jk_z^{mn}|z-z'|}}{2\,j\,a\,b\,k_z^{mn}} \, dS' \tag{2.38}$$

or, in a simpler way :

$$\vec{A}_{mn}(\vec{r}) = \hat{a}_p \, \frac{e^{-j\vec{k}\cdot\vec{r}}}{2\,j\,a\,b\,k_z^{mn}} \,, \tag{2.39}$$

where $\hat{a}_p = \iint \vec{J}(\vec{r}\,')\, e^{j\vec{k}\cdot\vec{r}\,'} dS'$ and $\vec{k} = \vec{k}_{mn} = (k_x^m, k_y^n, k_z^{mn}) = k\hat{u}_{mn} = k\hat{u}$, provided that $z > z'$. In this case, the absolute value from $|z - z'|$ can be removed in (2.38). Substitution of (2.39) into (2.37) yields the scattered electric field :

$$\vec{E}_{mn}(\vec{r}) = \frac{k^2}{j\omega\epsilon} (\hat{a}_p - (\hat{a}_p \cdot \hat{u})\hat{u}) \, \frac{e^{-j\vec{k}\cdot\vec{r}}}{2\,j\,a\,b\,k_z^{mn}} \,. \tag{2.40}$$

According to the MoM discretization, the surface current $\vec{J}(\vec{r}\,')$ can be expressed as a vector sum of the surface currents on the basis functions in which the surface is divided: $\vec{J}(\vec{r}\,') = \sum_{i=1}^{N} a_i \, \vec{J}_i(\vec{r}\,')$. Using the MoM's notation the electric field can be written as :

$$\vec{E}_{mn}(\vec{r}) = \frac{k^2}{j\omega\epsilon} \sum_{i}^{N} a_i \iint \frac{(\vec{J}_i - (\vec{J}_i \cdot \hat{u})\hat{u}))\, e^{-j\vec{k}\cdot(\vec{r}-\vec{r}\,')}}{2\,j\,a\,b\,k_z^{mn}} \, dS' \,, \tag{2.41}$$

where N is the number of basis functions. Now, the $e^{-j\vec{k}\cdot\vec{r}}$ factor can be placed out of the integral term :

$$\vec{E}_{mn}(\vec{r}) = \frac{-k^2}{2\,\omega\,\epsilon\,a\,b\,k_z^{mn}} \, e^{-j\vec{k}\cdot\vec{r}} \sum_{i}^{N} a_i \int (\vec{J}_i - (\vec{J}_i \cdot \hat{u})\hat{u}) \, e^{j\vec{k}\cdot\vec{r}\,'} \, dS' \,. \tag{2.42}$$

Finally, a sum of the electric field contributions of the different modes yields the total scattered electric field. The currents and integral in (2.42) are calculated with our MoM code for a given number of basis functions N. The $e^{-j\vec{k}\cdot\vec{r}}$ factor is added in a post-processing step. In this way, just one computation is needed for any observation point (x,y,z) provided that the observer's position is above the top of the surface $z > z'_{max}$.

2.2.5.3 Evanescent waves study

The scattered electric field above the infinite AMC described in Fig. 2.20 has been computed with our MoM code, as explained in the previous section. It consists of a propagating plane wave interfering with a number of evanescent waves. The first ($m = n = 0$ in (2.42)) is constant versus x and y coordinates if a and $b < \lambda/2$, the latter have a harmonic behavior versus horizontal coordinates. Fig. 2.21 represents the first modes of the y and z electric field components versus height for the frequency of resonance, that is 5.54 GHz. It clearly evidences the evanescent behavior when increasing the distance to the AMC. It can also be seen that, the higher the order mode, the lower the contribution to the total E-field. After the second order mode, the contributions rapidly become negligible. Hence, just the contribution of the first four modes has been taken into account to compute the total scattered E-field.

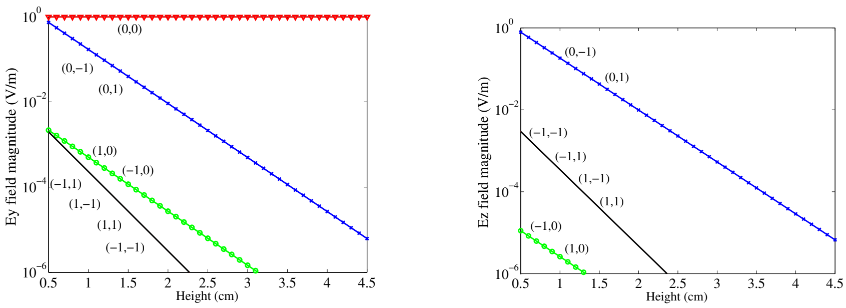

Figure 2.21 *The first four modes of the y (left) and z (right) E-field components for the frequency of resonance.*

The three components of the field computed at the resonant frequency (5.54 GHz) have been studied. The y and z components obtained at different distances are provided in Fig. 2.22. The graphics for the y component show magnitudes around 1 as expected, but they do not correspond to a single plane wave. The ripples correspond to the harmonic behavior of the higher-order modes. Close to the AMC (5 mm), the second-order harmonic is not negligible, resulting in small ripples at y = 0, ± 2 and ± 4 cm. It is worth noticing the huge ripples obtained close to the surface due to the presence of the evanescent waves. The z component magnitudes are also surprisingly big. The same study has been carried out for 4 GHz (out of the resonance region). Similar effects have been observed. However, the evanescent waves are very much stronger near the resonant frequency.

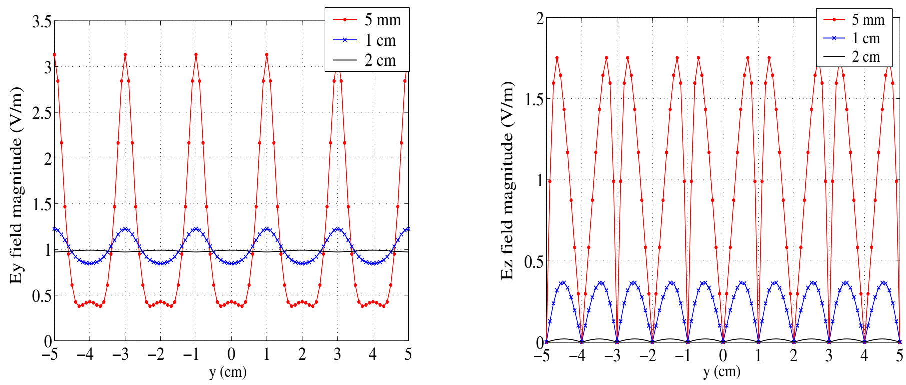

Figure 2.22 *XY-plane cut for the y (left) and z (right) components of the E-field scattered by an infinite AMC (computed with the UCL code).*

2.2.5.4 AMC truncation effect

The scattered electric field has been computed for a finite AMC surface. The commercial Feko software has been used. A 6x6 elements structure with the same unit cell as for the infinite case has been considered. It has also been illuminated by a plane wave polarized along $\hat{y}$, incident from broadside. The resonance frequency is now 5.87 GHz; the difference w.r.t. the infinite case may be due to the finiteness of the structure. Fig. 2.23 includes the y and z components of the total scattered field computed at different distances from the AMC. Compared to the infinite-array case, the uniformity of the scattered fields is broken. Also notice the similar orders of magnitude for both components. Given that the higher-order harmonics have a horizontal propagation component, they can be reflected by the edges of the array, making the effects of array truncation strongly visible near the resonant frequency. Indeed, truncation effects at 4 GHz have also been studied and observed; however they are stronger near the resonant frequency.

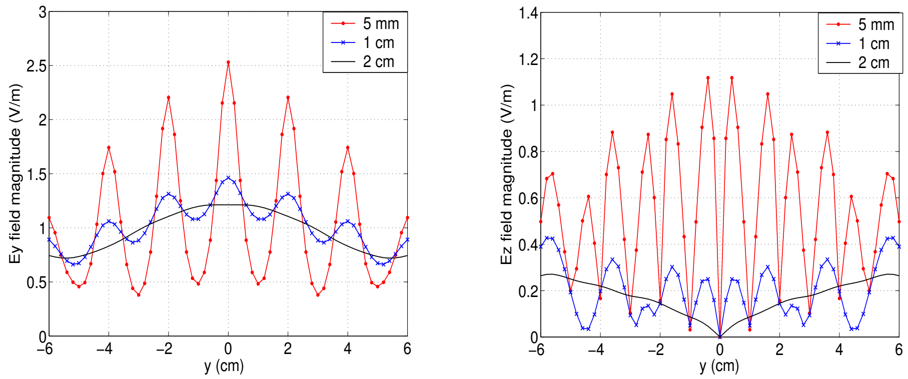

Figure 2.23 *XY-plane cut for the y (left) and z (right) components of the E-field scattered by a finite AMC (computed with Feko).*

2.3 Conclusion

Low-profile wideband antennas might be obtained by designing a ground plane with a reflection coefficient whose phase increases with frequency. Based on Foster's theorem, we prove that this is not possible if we consider the co-polar reflection on any lossless periodic structure. At first sight, the exploitation of the cross-polar components seems difficult for a reason related to polarization stability. AMC ground planes are an interesting solution since they allow antennas to be placed horizontally, very close above them. The study of a planar bow-tie dipole above two different AMC ground planes corroborates the interest of using an AMC surface w.r.t. a metallic plane. However, good directivity values are not obtained over the whole input impedance bandwidth. This limits the useful operating bandwidth of the antenna. The two following chapters propose two alternative antenna designs in order to overcome this limitation. We have also studied the fields near the AMC surface, with special attention given to evanescent waves present at small distances. A MoM-based code and the Feko software have been used to compute the fields scattered by an infinite and a finite AMC, respectively. It has been shown that the reactive fields are strong near the AMC resonant frequency, with a particularly strong $\hat{z}$ component. Truncation effects due to edge reflections are also stronger near the resonant AMC frequency. These reactive fields will certainly affect the antenna reactance. Then, the proximity of the antenna to the AMC surface plays an important role on the input impedance characteristics. Some additional resonances due to the whole antenna-AMC surface have been observed for the case of the bow-tie antenna. Therefore, when an antenna is placed above an AMC, the whole antenna-AMC combination has to be analysed instead of each single element independently.

3 Double-dipole antenna placed vertically above an AMC

When using AMC surfaces as ground planes for low-profile antenna configurations, working close to their resonance allows us to take advantage of their PMC features. However, as seen in Chapter 2, the directivity at broadside decreases as we approach the AMC resonance, limiting the useful operation bandwidth. This phenomenon is also visible in Best's work [38], also concerning the design of a bow-tie antenna above a mushroom-like EBG structure, and in the work presented in [39] and [40], where two different broadband dipole antennas, a diamond and a sleeve dipoles, are investigated.

It is evident in understanding that increased bandwidth will require a certain vertical extension. Hence, we initially propose here a dual-band antenna made of two dipoles stacked above the ground plane. The two narrow bandwidths would overlap to form one broader bandwidth. If the ground plane is a perfect electrical conductor, the dipole resonating at the lowest frequency end must be placed on top (see Fig. 3.1), which leads to a high profile. If the ground plane is an AMC resonating at the same frequency as the largest dipole, the latter can be placed close to the surface, i.e. beneath the shorter dipole (see Fig. 3.2).

At the frequency of resonance of the shorter dipole, the AMC is not resonating, and it appears as a perfect electric conductor. Hence, the shorter dipole must be maintained at a quarter wavelength from the ground plane. The advantage is that, besides the enlargement of the bandwidth, we are also considering a total height of a quarter wavelength at the highest frequency,

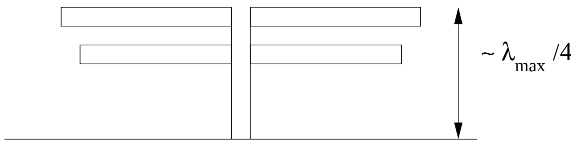

Figure 3.1 *Dual-band antenna consisting of two dipoles above a PEC.*

rather than at the lowest frequency. In the following sections, we will go

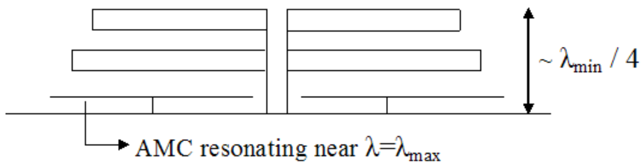

Figure 3.2 *Dual-band antenna consisting of two dipoles above an AMC.*

through an almost chronologic description of the hand-design work carried out, in order to provide some insight into the phenomena observed.

3.1 New antenna principle

The new antenna studied here consists of two planar dipoles resonating at two close frequencies at different distances from an AMC ground plane. In that way, the largest dipole takes advantage of the PMC properties of the AMC surface, providing an intermediate bandwidth and low-profile configuration at the same time. Besides this, the shorter dipole helps to enlarge the bandwidth and may contribute to the radiation performance providing better directivity levels over the whole useful band.

A picture of the proposed dipole design is provided in Fig. 3.3. The new antenna is single-fed at a central common point excited by means of a voltage gap. The dipoles width (w) and length (L_{top}, L_{bot}), along with the distance (s) between them are the design parameters. Together with the AMC parameters, they determine the resonances and both the impedance and directivity bandwidth achieved.

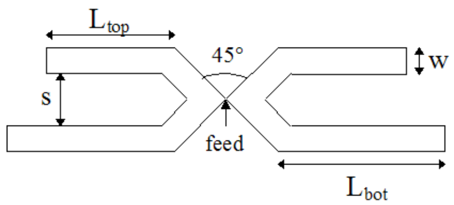

Figure 3.3 Design parameters (w, L_{top}, L_{bot} and s) of the newly proposed antenna. It consists of two plane dipoles fed at a common point.

A prototype with w equal to 0.41 mm and dipoles lengths equal to 2.2 mm (L_{top}) and 2.5 mm (L_{bot}) has been studied. The distance between dipoles is set to 0.4 mm. Fig. 3.4 contains the input reflection coefficient obtained for such design with respect to 50Ω and 75Ω. Two different resonances are clearly distinguished, as expected.

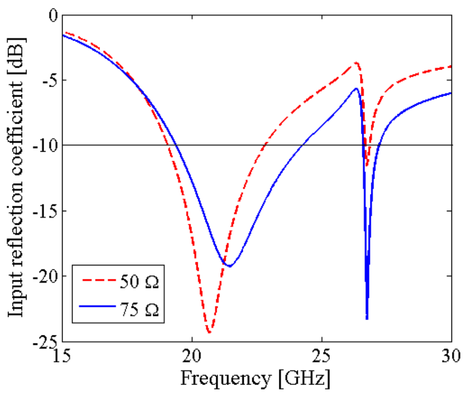

Figure 3.4 Input reflection coefficient of the prototype studied: w=0.41mm, L_{top}=2.2mm, L_{bot}=2.5mm and s=0.4mm.

The magnitude of the surface currents on the dipoles for the resonance frequencies are ploted in Fig. 3.5. It can be seen how currents are concentrated on the largest dipole for the lowest resonance and on the shorter one for the highest frequency. This fact supports the initial idea of having two dipoles which contribute independently to the design performances. The design parameters allow to tune the dual-band antenna in order to obtain the bandwidth and radiation performances desired.

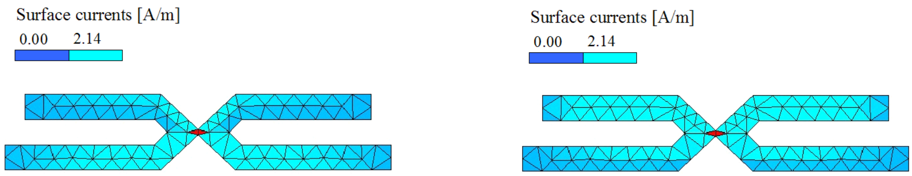

Figure 3.5 Magnitude of surface currents at 22.5 GHz (left) and 27 GHz (right). These are frequencies close to the resonance ones.

3.2 Effect of an AMC ground plane

Section 3.1 evidences the dual-band behavior of the proposed antenna. An EBG structure is now added as a ground plane, trying to obtain an intermediate bandwidth and low-profile configuration at the same time. Fig. 3.6 shows the antenna-AMC configuration studied. The mushroom-like EBG structure described in Section 2.2.3 is the one used in the following study, because the vias of the mushroom structure are supposed to suppress the surface waves that may travel along the AMC, contributing destructively to the radiation patterns of the antenna placed above the AMC. Initially, a substrate with permittivity equal to 2.2 (Fig. 2.13) fills the space between the patches and the ground plane, because using a substrate with permittivity bigger than 1 enables to reduce the profile of the design [17]. Then, the frequency at which the surface behaves as an AMC is 21.3 GHz instead of 26.3 GHz, when using the air (Section 2.2.3). In the whole design, the distance from the top edge of the shorter dipole to the bottom edge of the AMC ground plane is 2.8 mm (according to the $\lambda_{min}/4$ criterion illustrated in Fig. 3.2). An analysis of the impedance and radiation performances achievable with such antenna-EBG configuration are presented in the following sections.

3.2.1 Input impedance performances

The dual-band antenna presented in Section 3.1 is placed above the mushroom-like EBG surface specified before. A second prototype with a big-

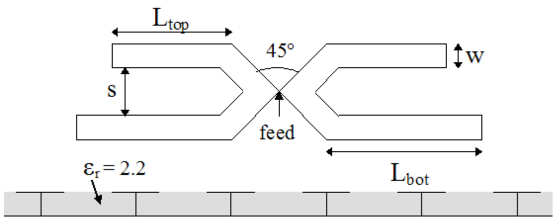

Figure 3.6 Dual-dipole antenna placed above a mushroom-like AMC.

ger difference between the dipoles length is also placed above the EBG structure and analysed. The designs studied are composed of dipoles with lengths equal to, on the one hand, 2.2 mm (L_{top}) and 2.5 mm (L_{bot}), and on the other hand, 2.1 mm (L_{top}) and 2.7 mm (L_{bot}). The input reflection coefficients obtained for both designs w.r.t. 50Ω and 75Ω are plotted in Fig. 3.7. A dual-band behavior, as for the antenna alone, is observed. The position of the two resonances w.r.t. the frequency at which the EBG surface behaves as a PMC (21.3 GHz for the mushroom structure here used), determines the performances achieved. By increasing the difference between the dipoles lengths, the frequency gap between their resonances is also increased (as seen in Fig. 3.7). As it was expected, a larger bandwidth is achieved with the configuration where the resonances are closer to each other.

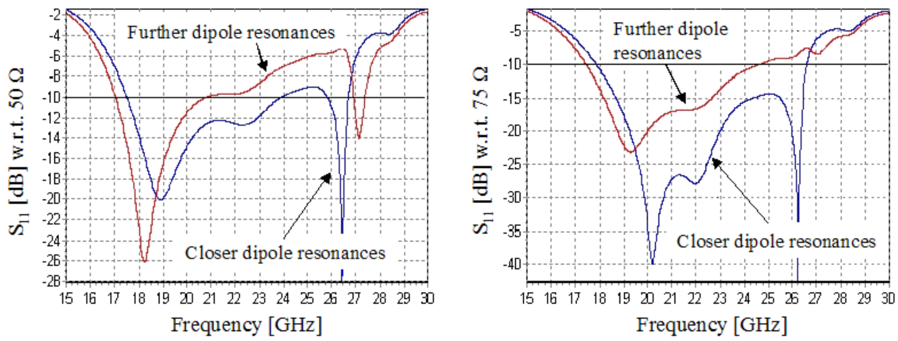

Figure 3.7 Input reflection coefficient w.r.t. 50Ω (left) and 75Ω (right) for two different dual-dipole antennas, with dipoles of different lengths, placed above a mushroom-like EBG structure.

3.2.2 Radiation performances

The directivity achieved at broadside ($\theta = 0°$, $\phi = 0°$) is here presented (see Fig. 3.8) for the two dual-dipole configurations analysed in Section 3.2.1. We observe values around 7 dB - 8 dB at the first resonance (18 GHz - 19 GHz), then a deep down to negative values, then a peak again. It is especially important to notice that the latter peak is produced at the frequency of the second resonance (beyond the AMC resonance). It confirms the contribution of the shorter top dipole to the radiation performance, as desired. However, Fig. 3.8 evidences that the narrower the gap between the two resonances, the smaller the peak obtained.

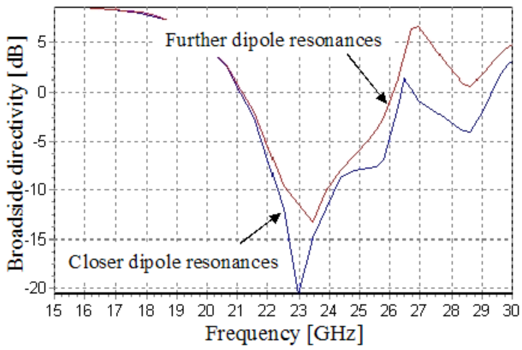

Figure 3.8 Broadside directivity achieved for two different dual-dipole antennas, with dipoles of different lengths, placed above a mushroom-like EBG surface.

To have an idea about the radiation performances obtained at the dipole resonances, Fig. 3.9 and Fig. 3.10 provide the radiation patterns for the dual-dipole antenna providing closer resonances ($L_{top} = 2.2$ mm and $L_{bot} = 2.5$ mm). The vertical cuts ($\phi = 0°$ and $\phi = 90°$) at f=18.75 GHz (left column) and f=26.48 GHz (right column) are ploted. A maximum is always observed at broadside ($\theta = 0°$) except in the H-plane for the second resonant frequency. A small dip appears in such a case. The performances obtained for configurations with other dipole lengths are very similar to the ones here shown. It is worth noticing that the broadside dip appearing in the H-plane is deeper when the frequency gap between the dipole resonances is smaller.

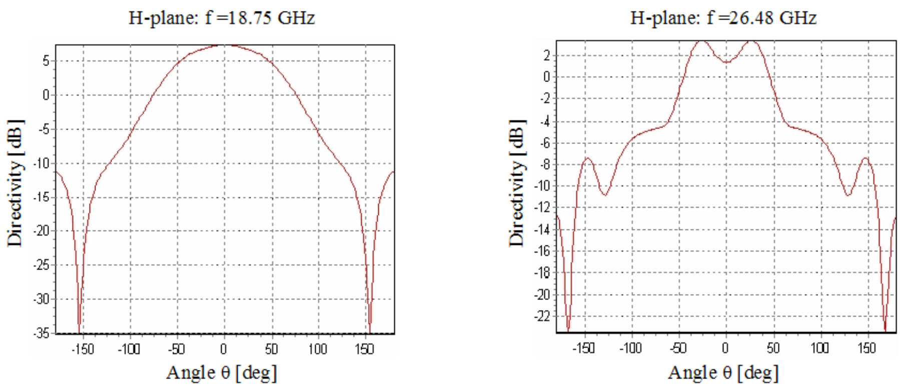

Figure 3.9 Radiation patterns at the $\phi = 0^\circ$ vertical cut for the dual-dipole antenna with closer resonant frequencies above a mushroom-like EBG surface.

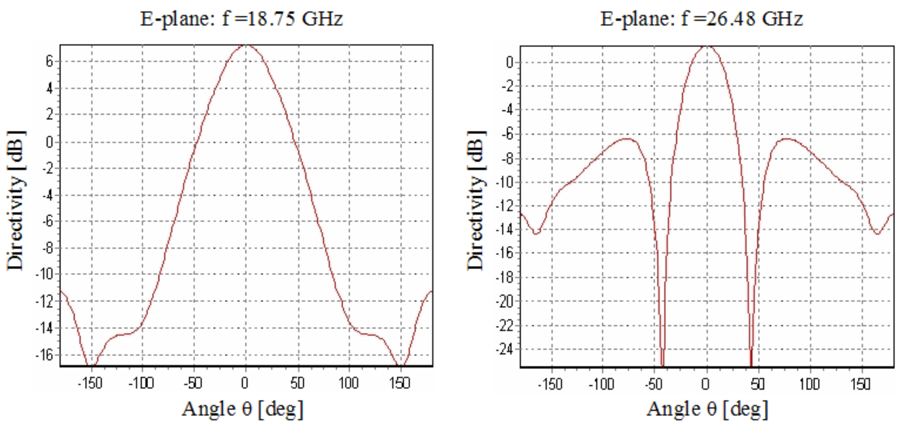

Figure 3.10 Radiation patterns at the $\phi = 90^\circ$ vertical cut for the dual-dipole antenna with closer resonant frequencies above a mushroom-like EBG surface.

3.3 Detailed study of the antenna performances

The two previous sections (Section 3.1 and Section 3.2) present the principles of operation of the new dual-band antenna. The present section provides a study on the impedance and radiation performances of a single planar dipole located above the EBG structure described in Section 2.2.3, and used in the study provided in Section 3.2. This has allowed us to better determine the contribution of each dipole composing the dual-band design to the performances achieved. Moreover, a parametric study on the planar dipole length and on its distance to the AMC surface has provided some basic rules for designing the dual-band antenna.

3.3.1 Performances comparison w.r.t. a single planar dipole

The performances obtained with a planar dipole located above the EBG presented in Section 2.2.3 are compared to the ones obtained for the dual-band antenna with closer resonances studied in Sections 3.2.1 and 3.2.2. The dimensions of the planar dipole and distance to the AMC ground plane are the same as the ones for the bottom dipole composing the dual-band antenna (see Fig. 3.11). This is, a planar dipole of 6.8 mm length and 0.41 mm width is placed at 1.58 mm from the bottom edge of the AMC.

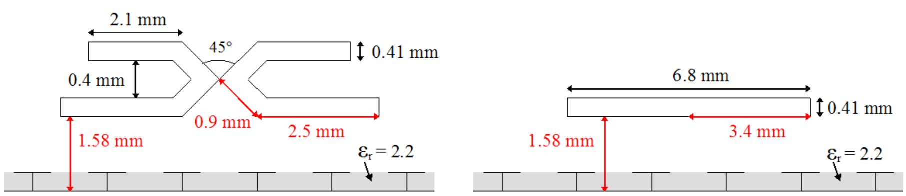

Figure 3.11 Dual-band antenna (left) and planar dipole (right) placed both at 1.58 mm from a mushroom-like EBG surface. The planar dipole has the same dimensions as the bottom dipole of the dual-band antenna.

Fig. 3.12 compares the input reflection coefficients obtained for the planar dipole and the dual-band configuration. The appearance of a second resonance along with a larger bandwidth is clearly evidenced for the latter antenna, as expected and desired. However, it is interesting to notice from a design point of view that the first resonance frequency is nearly the same for both antennas. The directivity performances achieved with the planar dipole

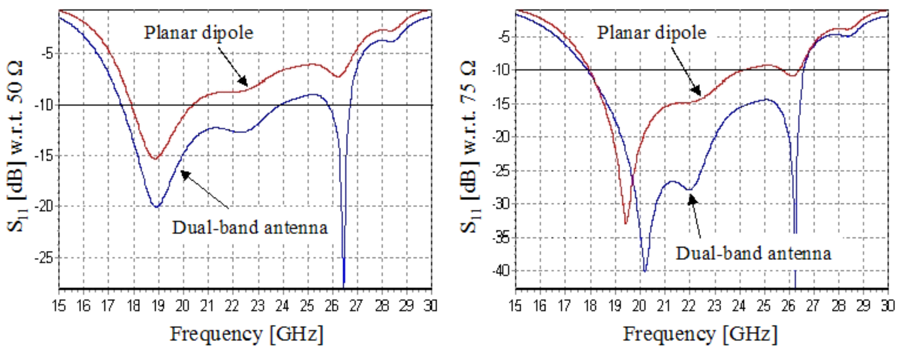

Figure 3.12 Input reflection coefficient for a dual-band antenna and a planar dipole with the same dimensions as the bottom dipole from the dual-band design.

and the dual-band antenna are compared in Fig. 3.13. It corroborates the directivity contribution of the top dipole at its resonant frequency ($\sim$ 26.5 GHz). On another hand, the directivity performance obtained at lower frequencies (< 21 GHz ($\sim$AMC resonance)) is nearly the same for the dual-band antenna as for the single dipole. We can then say that the bottom dipole contribution constitutes the basis of the directivity performance achieved with the dual-band antenna in the lower-frequency part.

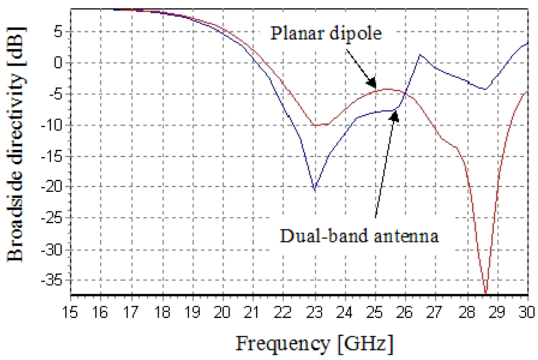

Figure 3.13 Directivity behavior vs. frequency for a dual-band antenna and a planar dipole with the dimensions of the bottom dipole from the dual-band design.

From the analysis presented above, one may say that the design of the bottom dipole should be the first step in the composition of the new antenna. Because of the similarity between its contribution and the performances obtained with a planar dipole placed at the same distance from the AMC, a parametric study of the latter has been carried out (see next section). Such a study provides some design rules that help to better determine the features of the new antenna designed.

3.3.2 Parametric study of a planar dipole above an AMC

The performances achieved with a planar dipole placed at a certain distance from an EBG surface depend on the position of the dipole resonance w.r.t. the frequency where the phase of the reflection coefficient is zero (AMC behavior). The dipole resonance is mainly determined by the dipole length and by its distance to the AMC ground plane. Thus, a study on the impedance and radiation performances of a planar dipole of varying length (*L*) placed at different distances (*d*) above a mushroom-like EBG structure has been carried out (see Fig. 3.14). The mushroom-like EBG surface with dielectric permittivity equal to 2.2 was used firstly to do the study. Afterwards, the same EBG surface, this time filled with air between the bottom ground plane and the mushroom patches, is tested. Only the results for the EBG without dielectric are provided here below, since the conclusions drawn are the same in both cases, and the EBG without dielectric (used in the following sections) will provide larger impedance bandwidths [17].

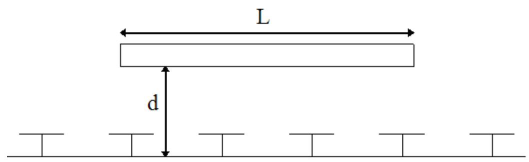

Figure 3.14 Parametric scheme under study. The air fills the space between the patches and the bottom ground plane of the mushroom structure.

The dipole length and distance from the AMC ground plane are chosen such that the dipole resonates close to the AMC resonance frequency (26.3

GHz). The dipole width is always equal to 0.41 mm. A dipole of 5.6 mm length is placed at 2 mm, 2.5 mm and 3 mm from the back ground plane of the EBG. The maximum height (3 mm) is $\lambda/4$ at the AMC resonant frequency. It has been chosen envisaging a profile smaller than $\lambda/4$. Fig. 3.15 provides the input reflection coefficient obtained w.r.t. 50Ω and 75Ω reference impedances. In both cases, the closer to the EBG surface, the smaller resonance frequency and the lower the profile. Fig. 3.16 contains a sweep in frequency of the directivity obtained at broadside. Since placing the planar dipole at smaller distances results in resonant frequencies further from the AMC resonance, the behavior of the EBG surface gets closer to a PEC behavior, and the closer the dipole is to the AMC ground plane, the better directivity values obtained (as seen in Fig. 3.16).

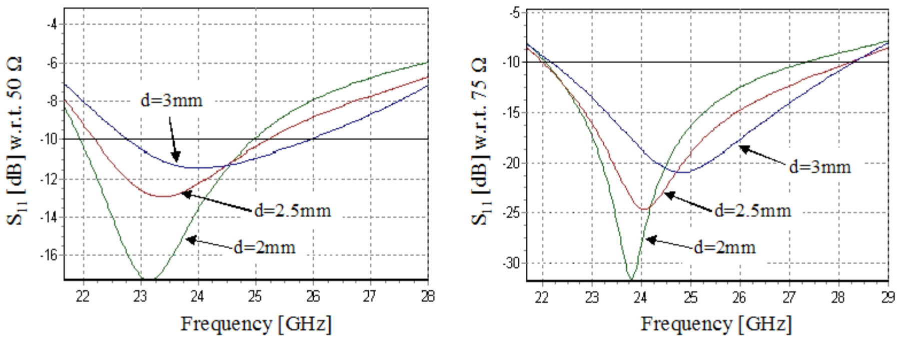

Figure 3.15 Input reflection coefficients for a planar dipole of 5.6 mm length placed at different distances from a mushroom-like EBG structure without dielectric.

The parametric study presented in this section, for a single dipole, reveals that the performances achieved strongly depend on the distance at which the dipole is placed from the AMC surface. Section 3.2 shows that the lengths of the dipoles composing the dual-band antenna need to be close one to each other in order to increase the impedance bandwidth. But, it has been seen (Section 3.2) that having closer dipole resonances does not help to improve the directivity achieved over the useful impedance bandwidth. Therefore, we can say that the determining parameter is not the lengths difference of the dipoles composing the dual-band design, but their distance to the AMC sur-

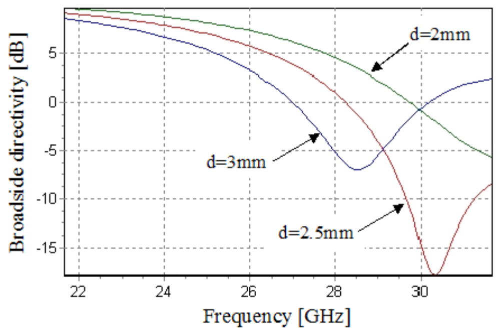

Figure 3.16 Directivity at broadside direction of a planar dipole of 5.6 mm length placed at different distances from a mushroom-like EBG without dielectric.

face. Then, we finally propose to design a dual-band antenna with dipoles of identical lengths. It is worth noting that if both arms of the dipole antenna have the same length, the antenna itself is not a dual-band dipole anymore. Nevertheless, when it is placed vertically above the AMC, the dipoles resonate at different frequencies because their distances to the AMC are different. The height at which the dipoles are placed above the AMC will be the main design parameter that will enable to achieve the desired performances.

3.4 Design of the double-dipole antenna

In this section, a double-dipole antenna is designed according to the operation principles observed in the previous sections. The analysis made previously has helped us to determine the relevant parameters in the design of the double-dipole antenna. The design of the bottom dipole is the first step in the design of the double-dipole antenna. Afterwards, the distances of the dipoles to the AMC surface are adjusted to fix an operating bandwidth with good directivity values over the whole band. A mushroom-like EBG filled with air is used as a ground plane since it provides larger impedance bandwidths [17]. At the end of the present section, we provide a comparison with the performances achieved when using a PEC as a ground plane in the proposed dual-band design.

3.4.1 Bottom dipole choice

The study presented in Section 3.3.2 shows that the closer to the AMC ground plane, the better directivity. In order to ensure a moderate directivity ($\geq$8 dB), we have chosen to initially place the bottom dipole of the double-dipole antenna presented in this section at 2 mm height, from the back ground plane of the EBG structure. A second dipole, with the same dimensions as the bottom one, is added on top. Thus, the double-dipole antenna designed here consists of two identical dipoles of length equal to 5.6 mm and width equal to 0.41 mm. The top dipole is located at 0.18 mm from the top edge of the first dipole in order to have a total antenna height equal to 3 mm ($\lambda_{min}/4$ maximum height criterion when envisaging a relative bandwidth around 20% ($f_{max} \approx$ 26.5 GHz and $f_{min} \approx$ 22 GHz)).

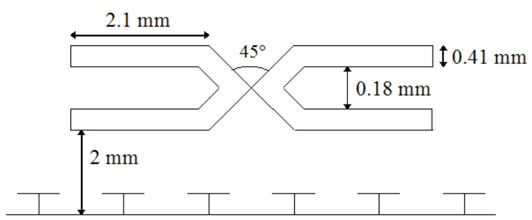

Figure 3.17 Double-dipole antenna with identical dipoles and a total antenna height equal to 3 mm.

The directivity and bandwidth performances achieved with such a configuration are compared to the ones obtained with a single dipole located at 2 mm height. The directivity obtained with the double-dipole structure is nearly the same as for the single dipole (see Fig. 3.18). However, the impedance bandwidth has considerably increased: from 13.22 % to 22.04 % for a 50Ω reference (left plot in Fig. 3.19), and from 22.22 % to 32.73 % for a 75Ω reference impedance (right plot in Fig. 3.19). Directivity values $\geqslant$ 5.25 dB are obtained in the 22.04 % 50Ω-impedance bandwidth.

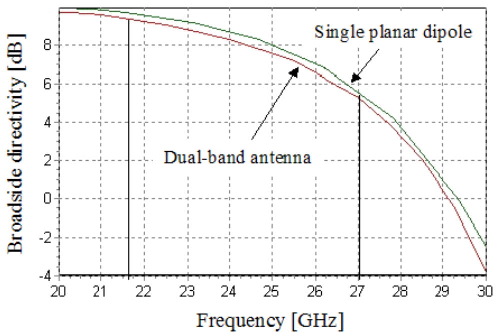

Figure 3.18 Directivity at broadside direction for both a double-dipole antenna consisting of two identical dipoles and a single dipole placed at 2 mm height from a mushroom-like EBG structure without dielectric.

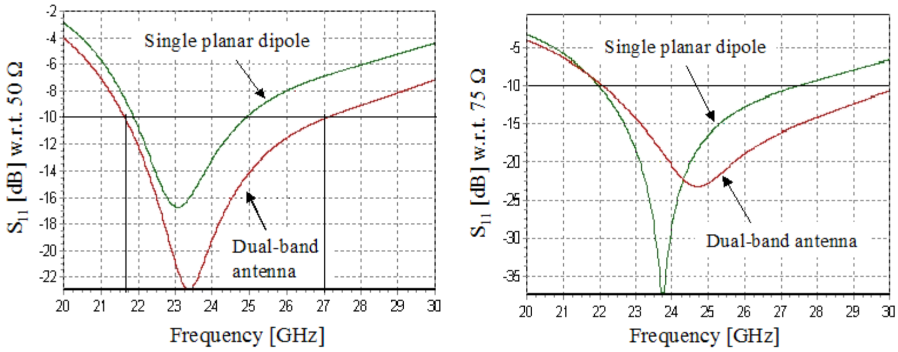

Figure 3.19 Input reflection coefficient w.r.t. 50Ω and 75Ω for both a double-dipole antenna consisting of two identical dipoles and a single dipole placed at 2 mm height from a mushroom-like EBG structure without dielectric.

But when enlarging the useful band without decreasing the height of the antenna, the profile factor becomes worse. So, the next step in this design (following section) consists of adjusting some parameters of the basic double-dipole configuration provided here, in order to achieve a lower profile ($\leqslant \lambda_{min}/4$) without losing directivity and impedance bandwidth.

3.4.2 Some parameter adjustments

According to the parametric study from Section 3.3.2, the distances of both dipoles to the AMC ground plane have been adjusted. First, a decrement of 0.5 mm has been applied to both distances, while keeping the separation (0.18 mm) between dipoles. The total height of the antenna is now 2.5 mm and the bottom dipole is located at 1.5 mm from the back edge of the EBG surface (see Fig. 3.20). With such dimensions, the useful band decreases (Fig. 3.21),

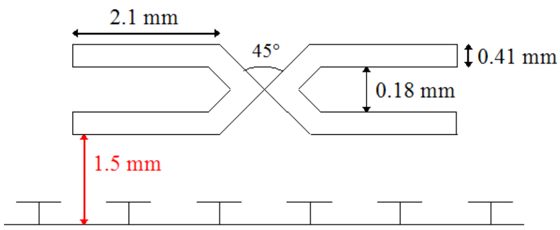

Figure 3.20 Double-dipole antenna with identical dipoles. The total antenna height is equal to 2.5 mm.

in contrast to the directivity performance, which experiments a considerable improvement (Fig. 3.22). Directivity values higher than 8.12 dB are obtained in a 17.15 % impedance bandwidth (relative to 50Ω). In such a case, the low profile factor is decreased from $\lambda_{min}/3.7$ to $\lambda_{min}/4.7$, where λ_{min} corresponds to the wavelength at the highest operation frequency.

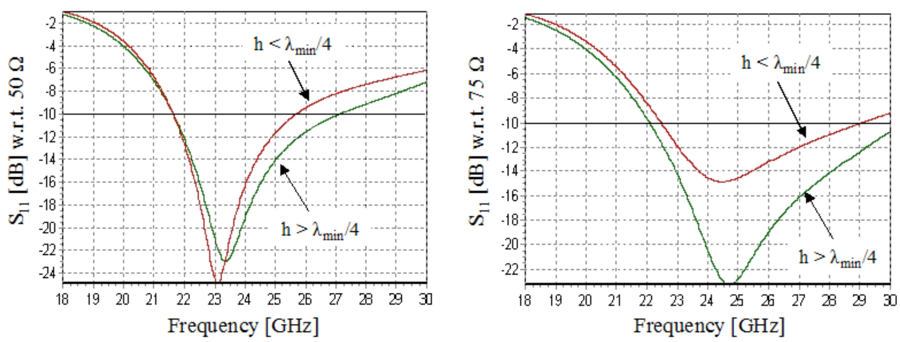

Figure 3.21 Input reflection coefficient w.r.t. both 50Ω and 75Ω obtained for two different antenna profiles (h) of a double-dipole configuration with identical dipoles.

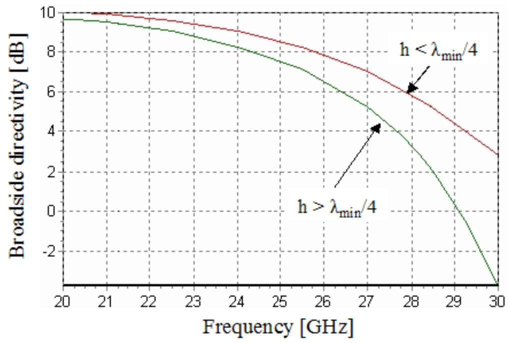

Figure 3.22 Directivity at broadside obtained for two different antenna profiles (h) of a double-dipole configuration with identical dipoles.

A second adjustment is applied so that the directivity values and the total antenna height of the previous configuration are maintained when trying to enlarge the impedance bandwidth. This time the bottom dipole is placed slightly closer to the top one, that is, the separation between dipoles is slightly decreased (set to 0.1 mm) (see Fig. 3.23). In such a way, a wider bandwidth

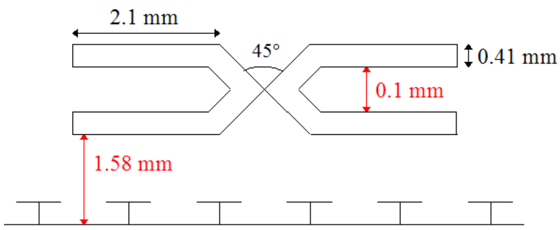

Figure 3.23 Double-dipole antenna with the bottom dipole placed at 1.58 mm from the bottom edge of the EBG surface. The total antenna height remains equal to 2.5 mm.

is achieved while keeping the directivity performance obtained after the first adjustment (Fig. 3.25). The useful band increases from 17.15% to 18.48% in the 50Ω reference case, as can be seen in Fig. 3.24. However, the directivity achieved at the highest useful frequency decreases from 8 dB to 7 dB. Thus, depending on the requirements, a tradeoff between the impedance bandwidth and the directivity achieved in the whole band should be found.

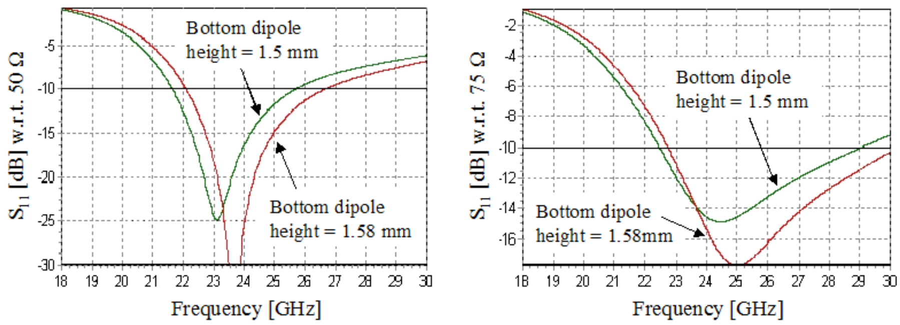

Figure 3.24 Input reflection coefficient w.r.t. both 50Ω and 75Ω for a double-dipole configuration with identical dipoles where the bottom one is placed at different distances from the EBG structure.

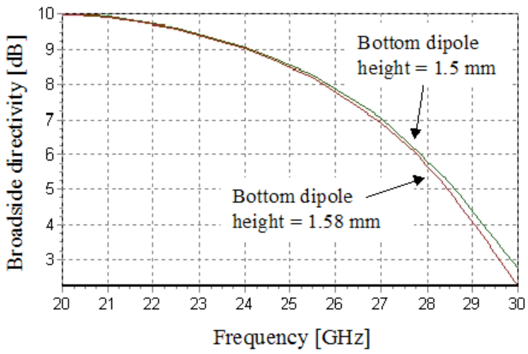

Figure 3.25 Directivity at broadside for a double-dipole configuration with identical dipoles where the bottom one is placed at different distances from the EBG structure.

3.4.3 Medium gain, medium bandwidth design

The dimensions and performances of a final double-dipole design proposed as medium gain, medium bandwidth antenna are summarized and presented here. A picture of the design is provided in Fig. 3.26. An EBG structure is used as AMC ground plane. It consists of square metal patches connected to a solid metal sheet by conducting vias. The spacing between the patches is 0.5 mm, while the length of the patches is 3 mm. The length and radius of the vias are equal to 1 mm and 0.125 mm, respectively. Like in the last previous sections, the space between the plates and the ground plane is filled with air ($\epsilon_r = 1$).

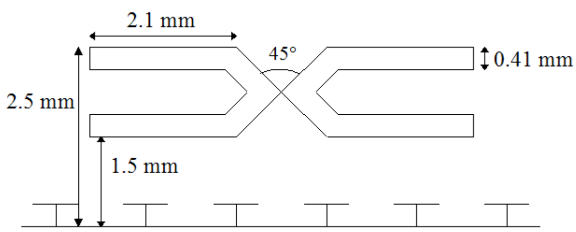

Figure 3.26 *Dimensions of the design proposed as medium gain prototype.*

Such a prototype provides more than 8.12 dB of broadside gain and a better than -10 dB reflection coefficient over a 17.15% bandwidth. Fig. 3.27 provides the performances achieved with such a design. Good directivity performances are obtained in the whole useful band. A $\lambda_{min}/4.64$ profile is achieved, where λ_{min} is again the wavelength at the highest operation frequency.

To have an idea about the radiation performances obtained at frequencies within the impedance bandwidth, some radiation patterns are provided. Fig. 3.28 and Fig. 3.29 plot the vertical cuts $\phi = 0\,^\circ$ (H-plane) and $\phi = 90\,^\circ$ (E-plane) at f=23.1 GHz (left column) and f=25.5 GHz (right column). A maximum is always observed at broadside ($\theta = 0\,^\circ$), except for the H-plane at f=25.5 GHz. A small deep appears in such a case. However, the directivity values remain acceptable and do not reach negative values as it did for the planar bow-tie dipole antenna case (see Section 2.2.4).

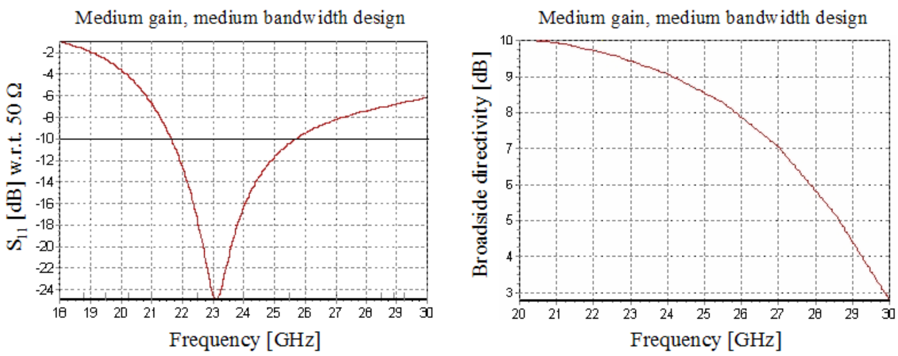

Figure 3.27 *Performances achieved with the medium gain prototype proposed.*

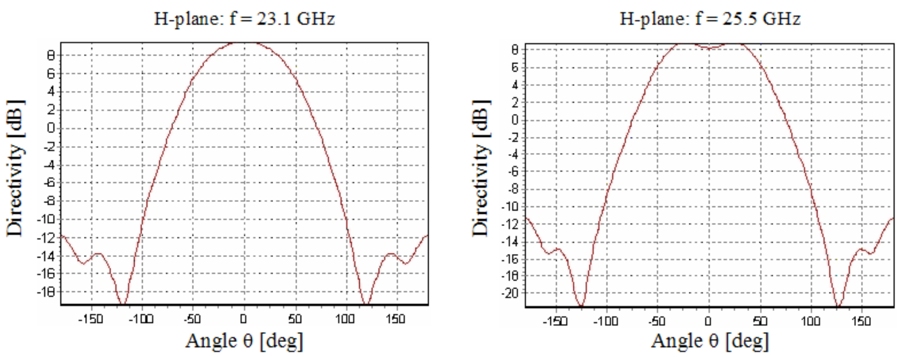

Figure 3.28 *Radiation patterns at the $\phi = 0^\circ$ vertical cut for the medium directivity design.*

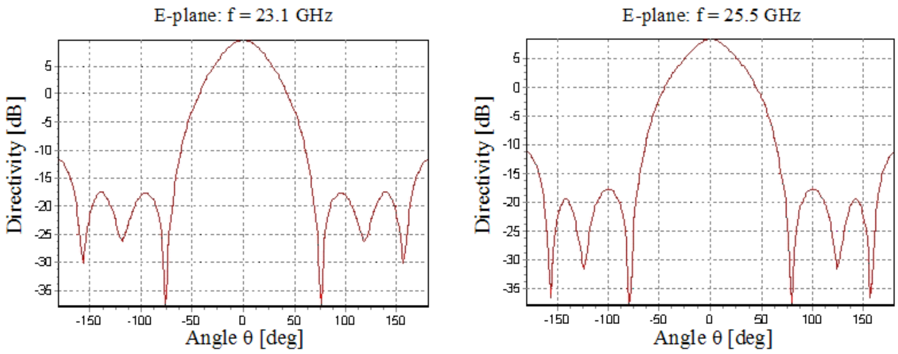

Figure 3.29 *Radiation patterns at the $\phi = 90°$ vertical cut for the medium directivity design.*

3.4.4 Interest of using an AMC instead of a PEC

A comparison of the performances obtained when using a PEC instead of the AMC surface as a ground plane for the double-dipole antenna proposed in Section 3.4.3 is carried out. The antenna is placed at a distance such that the profile factor is the same as the one obtained with the configuration presented in Section 3.4.3. That means, a profile equal to $\lambda_{min}/4.64$. Fig. 3.30 includes the results obtained with the two different ground planes. While an impedance bandwidth (left plot) equal to 10.97% is achieved with the PEC, a 17.15% bandwidth is obtained with the AMC consisting in a mushroom-like EBG surface. Directivity values (right plot) between 8.46 dB and 8.56 dB in the useful impedance band are observed for the PEC case, while directivities are comprised between 8.12 dB and 9.8 dB for the AMC configuration. Hence, better directivity and impedance bandwidth performances are achieved by using an AMC surface as a ground plane.

- Directivity of a dipole above a PEC

It is worth noticing that the directivities obtained in the previous comparisons with the PEC are very constant over the whole useful band. We would have expected a decreasing behavior when going up in frequency. So, in order to ensure the correction of our results, we have calculated and plotted the directivity of a short dipole placed horizontally above a PEC at different distances. The heights are expressed in terms of wavelengths in Fig. 3.31. It shows that,

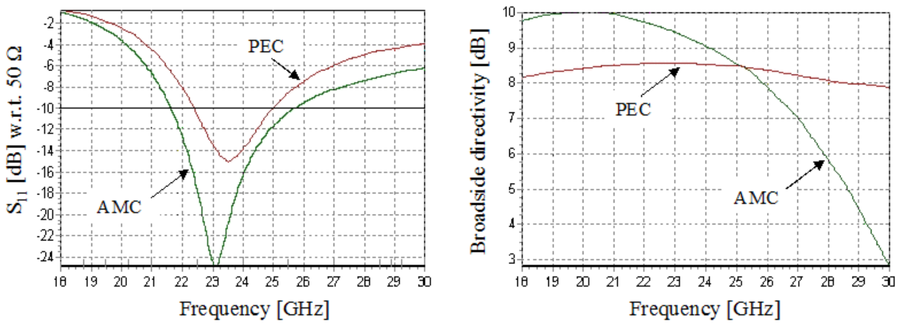

Figure 3.30 *Comparison of the input reflection coefficient and the broadside directivity obtained when using an AMC and a PEC as a ground plane for the double-dipole antenna from Section 3.4.3.*

for profiles smaller than $\lambda/4$, the slope of the directivity curve is quite smooth. This explains the small variation observed in the comparisons presented before, ensuring their validity.

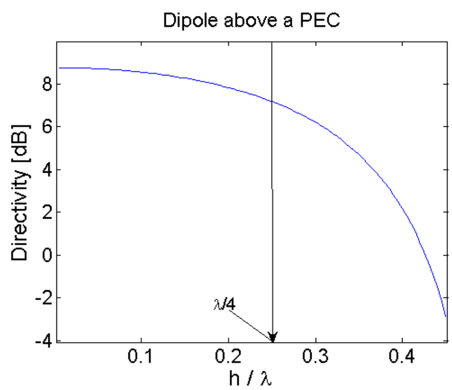

Figure 3.31 *Directivity of an horizontal dipole placed above a PEC versus electrical height (h/λ).*

3.5 Conclusion

A new antenna configuration has been proposed as an alternative to the planar bow-tie dipole antenna studied in Section 2.2.4. It consists of two planar dipoles resonating at two close frequencies at different distances from an AMC ground plane. The initial idea of having dipoles of different lengths does not finally help to improve the directivity and enlarge the impedance bandwidth at the same time. Then, a design of dipoles with identical lengths is proposed. The distance of the dipoles to the AMC determines the performances achieved. The closer to the AMC the higher directivities obtained, but narrower impedance bandwidths are achieved. Since the vertical separation between the dipoles is small, their directivity contributions are practically the same. The top dipole mainly helps to enlarge the impedance bandwidth. A prototype providing more than 8.12 dB over a 17.15% bandwidth is presented in Section 3.4.3. The profile of the design is $\lambda_{min}/4.64$, where λ_{min} corresponds to the wavelength of the highest operation frequency. The profile is defined from the ground plane backing the whole design, i.e. antenna and AMC combination, and measured as a factor of λ_{min} because it represents the worst profile of the operation bandwidth. Good radiation patterns are obtained over the whole useful band. However, the proposed solution does not help to solve the problem if designs with wider bandwidths are desired. The broadside directivity still decreases near and beyond the AMC resonance. It is also worth noting that the vias connecting the patches to the back ground plane of the AMC do not seem to help us either to avoid this problem. The next chapter proposes a new solution, based on the design of a new AMC surface (not including vias).

Double-dipole antenna above an aperiodic AMC

4

The solution proposed in Chapter 3, to enlarge the useful operating bandwidth obtained for an antenna placed above an AMC ground plane, provides bandwidths around 17% with broadside directivities higher than 8 dB in the whole bandwidth. Despite the improvements already achieved w.r.t. the planar bow-tie dipole antenna studied in Section 2.2.4, a decrease of the broadside directivity near and beyond the AMC resonance is still observed. Then, the useful achievable bandwidth is still limited. Moreover, it would be interesting to obtain lower profiles than the ones provided by the vertical double-dipole antenna proposed in Chapter 3. Thus, a new solution, concerning the design of a new AMC surface, is studied in the present chapter. The double-dipole antenna presented in Chapter 3 is placed this time horizontally above the AMC in order to achieve lower profiles.

In this chapter, we firstly expose the problem of splitting patterns in detail. In order to have a further physical insight into this splitting effect, a modal analysis using a home-made code based on the Method of Moments (MoM) technique is provided in Section 4.3 and Section 4.4. An original extension of this code has been developed (see Chapter 5) to study the leaky-modes supported by the AMC surface. Section 4.2 sets the numerical computation basis of the eigenmode analysis presented in the later sections. The directivity improvement achieved with the new AMC design is presented in Section 4.4. A final design together with its performances is finally provided in Section 4.5.

4.1 The problem of splitting patterns

The prototype here studied consists of a double planar dipole antenna located above an artificial PMC. Figure 4.1 shows the double-dipole antenna studied, which is fed at a central common point by means of a voltage gap. The dipoles width w and length L, along with the distance s between them are the design parameters.

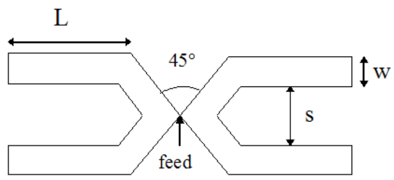

Figure 4.1 *Design parameters (w, L and s) of the double-dipole antenna studied.*

The AMC is a finite array made of 6×6 metal square patches placed on a grounded dielectric substrate. Fig. 4.2 provides the dimensions of the unit cell. The length of the patches is equal to 3 mm and the space between them is 0.5 mm. In order to achieve the largest possible bandwidth, air ($\varepsilon_r = 1$) fills the space between the patches and the ground plane. The patches are located 1 mm above the metal sheet. There are not vias connecting the patches to the back ground plane since they do not seem to improve the radiation performance of the design (see Chapter 2 and Chapter 3) and they are difficult to fabricate.

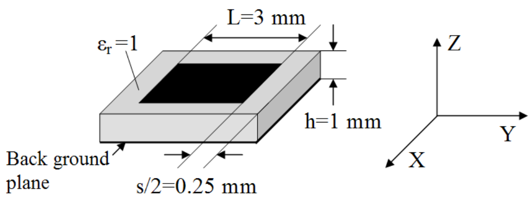

Figure 4.2 *Unit cell of the 6×6 AMC considered.*

Fig. 4.3 shows the phase of the reflection coefficient versus frequency, obtained when the surface is illuminated from broadside by a plane wave polarized along $\hat{y}$. The resonance frequency of the AMC, for which the phase crosses $0\,^{\circ}$, is 27.4 GHz. The reflection coefficient is computed with Matlab, from the scattered E-fields obtained with FEKO at 1 cm distance above the surface. The phase difference introduced by the height at which the fields are calculated is corrected to compute the phase just on the plane that contains the AMC patches.

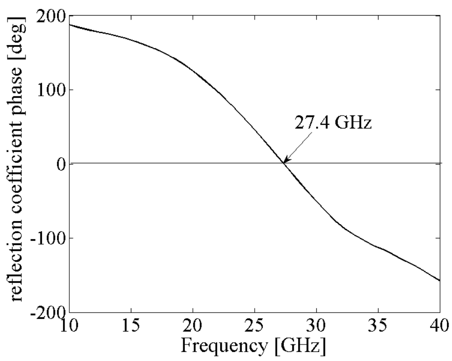

Figure 4.3 *Phase behavior of the reflection coefficient obtained when illuminating the 6×6 finite AMC, consisting of an array of square patches.*

The antenna is placed horizontally at 1.5 mm from the bottom surface of the AMC (Fig. 4.4). We have computed the input reflection coefficient w.r.t. 50 Ω and the radiation patterns for configurations with double-dipole antennas of different lengths L, all of them resonating close to the AMC resonance (27.4 GHz). The dipoles width and the distance between them are always 0.41 mm and 0.185 mm. Impedance bandwidths (S_{11} $<$ -10 dB) around 20%-30% can be achieved. However, we observe that the radiation patterns split at broadside near and beyond the AMC resonant frequency, reducing the real useful band. The input reflection coefficient and the broadside directivity for an antenna with dipoles of length equal to 1.7 mm are shown in Fig. 4.5. A relative impedance bandwidth equal to 18.7% is achieved in that case. When observing the broadside directivity versus frequency, we see that it dramatically decreases when approaching the AMC resonance, reaching even deep negative values (in dB) at higher frequencies -a strong dip is observed at 35.5 GHz-. This means that the degradation of the broadside radiation performances is gradual as the frequency increases beyond the AMC resonance, getting the worst at 35.5 GHz.

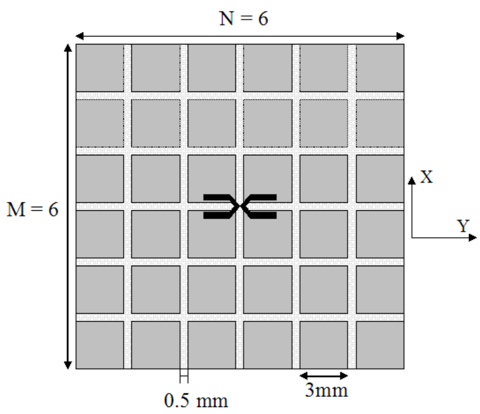

Figure 4.4 *Double-dipole antenna placed horizontally above the square 6×6 AMC.*

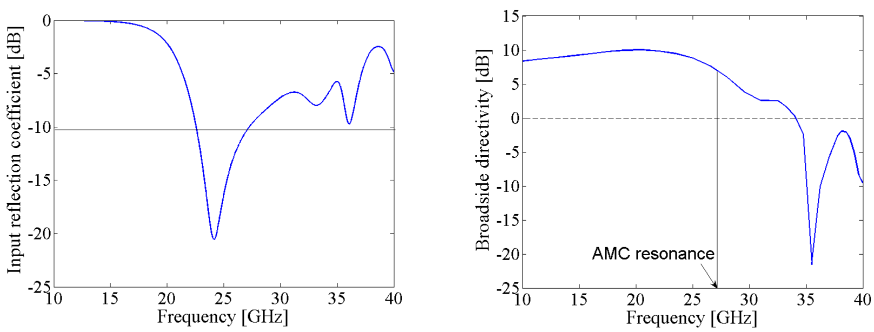

Figure 4.5 *Reflection coefficient w.r.t. 50 Ω (left) and broadside directivity (right) for a double-dipole antenna of 1.7 mm dipoles length horizontally placed above the 6×6 AMC.*

Fig. 4.6 shows vertical cuts in the E-plane and in the H-plane of the radiation patterns obtained for 35.5 GHz. It is clearly seen how the patterns split at broadside in both planes.

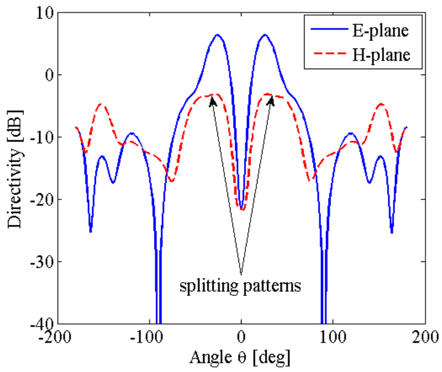

Figure 4.6 *Radiation patterns in both the E-plane and the H-plane at f=35.5 GHz, obtained for the double-dipole antenna of 1.7 mm dipoles length placed above the 6×6 AMC.*

4.2 Modal analysis of the AMC surface

Knowing the modal features of the AMC ground plane will provide us a better understanding about what is happening at the frequencies where the patterns split. To this end, an eigenmodes analysis has been carried out by using the home-made code developed at our laboratory [35], [36]. An extension of it (see Section 5), based on the theory for the periodic Green's function reviewed in Section 2.2.2, has been elaborated to analyse the leaky-modes supported by the AMC surface under study. Before exposing the results of the eigenmodes analysis in Sections 4.3 and 4.4, we provide here a description of the dispersion diagram representation for a periodic structure, together with a brief review about leaky waves, in order to help to the reader to better understand the results obtained and discussed later.

4.2.1 Computation of eigenmodes

As described in Section 2.2.1, the MoM system of equations reads:

$$Z\,I = V \tag{4.1}$$

where Z is the $N \times N$ MoM impedance matrix, I is the column vector containing the N unknowns describing the currents and V is the excitation vector (fields E^i impressed on the N basis functions). The MoM impedance matrix Z

can also be used for computing the eigenmodes of a structure. If we look for the resonances of a structure, all elements of V are zero (no excitation) and the solution of the equations system (4.1) becomes an eigenvalues problem. For a two-dimensional periodic structure, the impedance matrix Z depends on the frequency f and on the phase shifts between successive unit cells, ψ_x and ψ_y, it is $Z(f, \psi_x, \psi_y)$. The values of f, ψ_x and ψ_y that make the determinant of Z equal to zero correspond to the eigenmodes of the structure. The dispersion relation $f = f^{on}(\vec{k}_s)$, described in more detail in Section 4.2.2, can then be obtained. The dispersion relation gives the frequencies for which the wave modes travel along the structure, as well as their corresponding propagation directions described by the vector $\vec{k}_s$.

4.2.2 Dispersion diagram

The present section provides a description of the dispersion diagrams representing the modal features of a periodic structure. According to the Floquet wave decomposition associated to plane waves supported by periodic structures (see Section 2.2.2.2), the wave vectors of the resulting set of plane waves, for a two-dimensional periodic structure, are related by:

$$k_x^m = k_x + m\frac{2\,\pi}{d_x} \qquad k_y^n = k_y + n\frac{2\,\pi}{d_y} \tag{4.2}$$

in the x and y directions, respectively. This means that the wave vector $\vec{k}_s$, related to the wave modes travelling along the structure, is a periodic function with periodicity $(2\pi)/d_x$ and $(2\pi)/d_y$ in the x and y directions, respectively. Consequently, the dispersion relation $f = F(\vec{k}_s)$ associated to a periodic structure is also a periodic function F of $\vec{k}_s$. Thanks to this periodicity, the search for the eigenmodes of a periodic structure only needs to be carried out in a unit cell of the periodic structure, which corresponds to the so-called first Brillouin zone [43]. Besides this, the first Brillouin zone may be redundant because of symmetries. Then, the redundant regions can be eliminated to avoid the $\vec{k}_s$ redundancy and further simplify the eigenmodes search. The smallest region within the Brillouin zone for which the $\vec{k}_s$ directions are not related by symmetry is called the *irreducible* Brillouin zone. For example, the irreducible Brillouin zone related to a periodic structure with a doubly-symmetric square lattice, is a triangle, with 1/8 the area of the full Brillouin zone, defined by the Γ, X and M points (see Fig. 4.7). The rest of the Brillouin zone contains redundant copies of the irreducible zone.

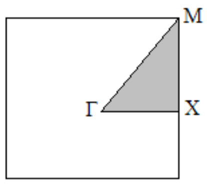

Figure 4.7 Brillouin zone of a periodic structure with a square lattice. The irreducible Brillouin zone is shown in darker color.

The dispersion relation associated with the irreducible Brillouin zone of a periodic structure with a square lattice is represented in a dispersion diagram like the one shown in Fig. 4.8. The ΓX, XM and MΓ paths represent all the possible planar directions of propagation (k_x, k_y) contained in the area of the irreducible Brillouin zone. We remind that the propagation vectors (k_x, k_y) are related to the phase shifts between the elements of the periodic structure as $(\psi_x = k_x\, d_x, \psi_y = k_y\, d_y)$.

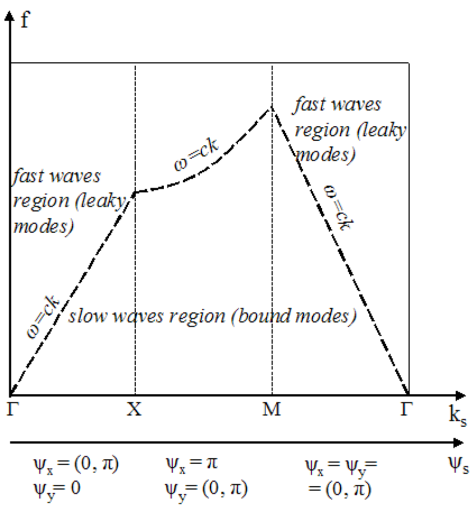

Figure 4.8 General representation of the $f - \psi_s$ dispersion diagram corresponding to the irreducible Brillouin zone of a periodic structure with a square lattice.

The light line in Fig. 4.8, which corresponds to the relation $\omega = c\,k$, where k is the free-space wave vector, divides the diagram in two regions: the slow waves and the fast waves regions. When $\omega < c\,k_s$, it means that $k_s > k$ and there are no angles (θ, ϕ) for which the relations (4.3) below are satisfied. Hence, radiation into free space cannot occur. The modes corresponding to such k_s values are called bound modes. Bound modes propagate across the structure without radiating, but on a finite structure they may reach the edges, resulting in a free space multi-path radiation.

$$k_x = k \sin\theta \cos\phi \qquad k_y = k \sin\theta \sin\phi \tag{4.3}$$

On the contrary, when $k_s < k$, which means $\omega > c\,k_s$, energy can be radiated into free space, in the direction (θ, ϕ). The related modes satisfying $k_s < k$ are known as leaky modes. Modes with wave vectors near $k_s = 0$ radiate perpendicular to the structure, while modes near the light line, $k_s = \omega/c$ (see Fig. 4.8), radiate in a transversal direction, i.e. $\theta = 90\,°$.

4.2.3 Leaky wave modes

Leaky waves propagate transversely with a complex propagation constant $k_{LW} = \beta - j\alpha$ (Fig. 4.9), with β and α standing for the phase and the attenuation constants [47], [49]. The main characteristic of a leaky wave is that $\beta < k$ so that the wave velocity is faster than light, i.e. $\omega > c\,k_s$. The wave may radiate at a specified angle into space, depending on β. Small values of α result in large effective radiating apertures, and then narrow beamwidth patterns. Another well-known property of leaky waves is that they are *improper* [47], [48], which means having a field amplitude that increases exponentially away from the surface that guides them (see Fig. 4.9). On the contrary, modes bound to the surface are *proper*, with a field decreasing exponentially away from the surface.

Radiation from leaky waves is often considered as undesired leakage that produces power losses. However, leaky-waves radiation can also be advantageous for some kind of antennas and applications. In our concern, having leaky-waves propagating along the AMC surface that radiate at broadside can help us to overcome the problem of splitting patterns presented in Section 4.1. From there, our interest in studying leaky-wave antennas (LWA). Leaky-wave

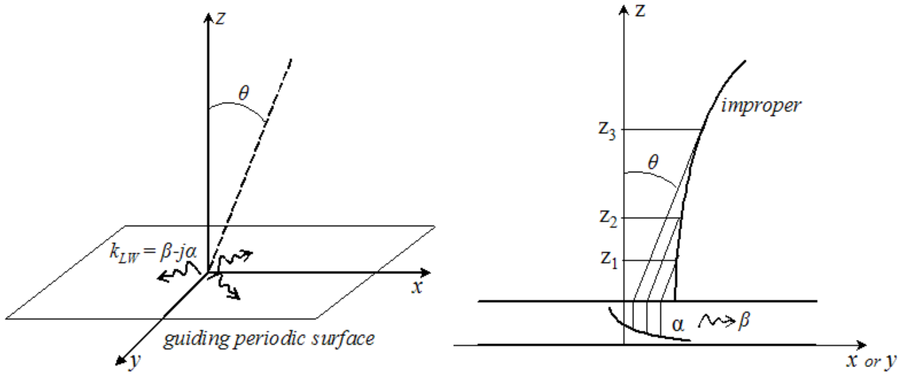

Figure 4.9 Leaky waves propagate transversely.

antennas generally consist of a structure capable of guiding leaky waves, and a simple source that excites them [49]. The launched leaky waves can determine the radiation behavior of the antenna. If a weakly attenuated (small α) leaky wave is dominant on a guiding surface, the total radiation pattern will be determined by the radiation from the leaky wave. It is important to note that two leaky waves traveling in opposite directions will appear if the structure is symmetrical, which is the case for the AMC surfaces we are studying. Then, the radiation pattern due to those leaky waves will be the superposition of two beams, symmetric w.r.t. the broadside direction (see Figs. 4.10 and 4.11).

Broadside radiation from a leaky-wave antenna can be obtained for small values of β [49]. By decreasing β, θ becomes smaller since $\beta = k\, sin\theta\, cos\phi$, and when the two beams are close enough to each other, depending on their beamwidths, a total pattern pointing at broadside may be obtained. The beamwidth of the lobes depends on the attenuation constant α with an inversely propportional relation [49]. Small values of α produce narrow beams. Then, a single beam pointing at broadside can be obtained with small radiation angles, i.e. small values of β, and wide beams (big α) so that their superposition results in a maximum at broadside (see Fig. 4.10). On the contrary, if β is big and weak attenuation constants are present, a beam with two distinct narrow peaks away from broadside will be observed (see Fig. 4.11). It can be proven [49] that the condition $\beta = \alpha$ represents the splitting condition

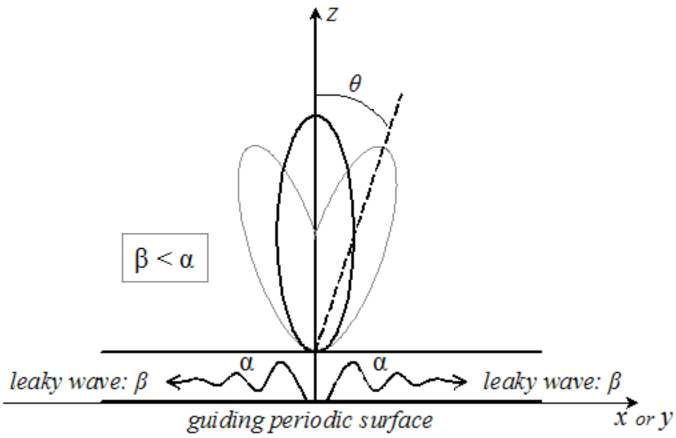

Figure 4.10 Radiation pattern with a single beam pointing at broadside ($\beta < \alpha$).

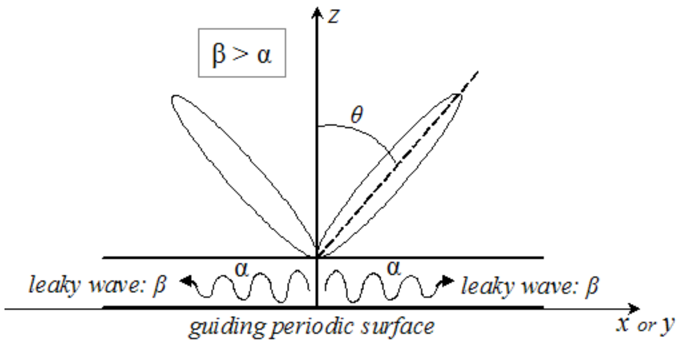

Figure 4.11 Radiation pattern with two beams away from broadside ($\beta > \alpha$).

between the case of a beam pointing at broadside ($\beta < \alpha$) and two distinct beams close to, but away from broadside ($\beta > \alpha$). The $\beta \simeq \alpha$ condition means that the beams width have to be at least equal to their tilt in order to be superimposed. As mentioned before, this superpositon may result in a single beam pointing at broadside when β will be small enough w.r.t. α. The particular geometry of the guiding structure will determine the propagation constants β and α.

4.3 Infinitely periodic AMC

An eigenmode analysis based on the Method-of-Moments (MoM) technique described in Section 2.2.1 is here performed to study the wave modes supported by an AMC consisting of a backgrounded array of square patches. The geometry of the array of grounded square patches under consideration is shown in Fig. 4.12. It is an infinite array in x and y directions with inter-element spacings denoted by d_x and d_y, respectively. L_p stands for the patches length.

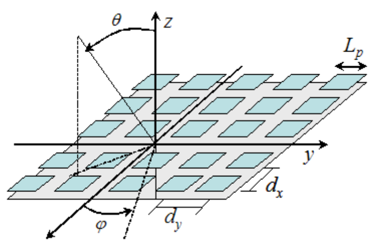

Figure 4.12 Geometry of the infinite array of grounded patches under study.

4.3.1 Eigenmodes analysis

As explained in Section 4.2.1, searching the roots of the determinant of the MoM impedance matrix $Z(f, \psi_x, \psi_y)$ provides the dispersion diagram of the modes supported by the structure. We have obtained the dispersion diagrams for the planar patch array described in Fig. 4.12, composed of patches with two different sizes: 3 mm (Fig. 4.13) and 2.5 mm (Fig. 4.14). In both cases the patches are at 1mm from the ground plane, separated by a gap equal to

0.5 mm in both directions. The space between the patches and the ground plane is filled with air. So far, only modes corresponding to real propagation wavenumbers (bound modes, outside the light cone, i.e. $k_{x,y} > k$) have been searched for. For the 3mm patches (Fig 4.13), a mode corresponding to a 180

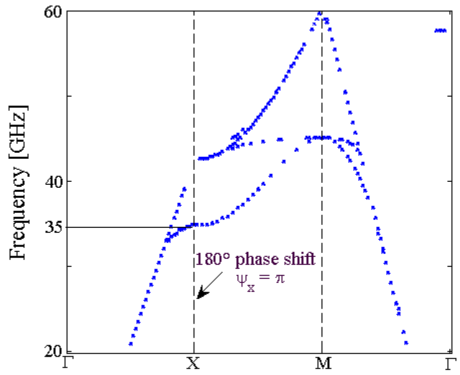

Figure 4.13 The $f - \psi$ dispersion diagram (only bound modes) for a planar periodic patch array with patches of 3 mm length.

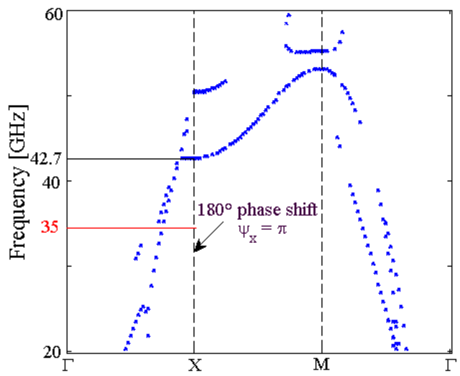

Figure 4.14 The $f - \psi$ dispersion diagram (only bound modes) for a planar periodic patch array with patches of 2.5 mm length.

degrees inter-element phase shift exists at a frequency around $f_0 = 35$ GHz. It is worth noticing that a strong pattern dip at broadside has been observed at $f = 35.5$ GHz (Section 4.1). From the dispersion diagram obtained for patches of 2.5 mm (Fig. 4.14), it is seen that the frequency at which such a mode appears is moved to 42.7 GHz. Such effect is clearly seen if we plot $|Z|$ at the X point of the dispersion curves (Fig. 4.15).

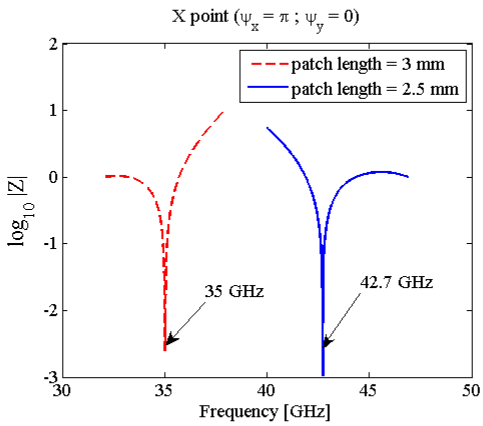

Figure 4.15 Determinant of the Z matrix vs. frequency obtained for infinite AMC surfaces with patches of different sizes.

4.3.2 Surface currents

After the modal analysis presented in Section 4.3.1, it is worth paying attention to the currents induced on the antenna-AMC combination. The double-dipole antenna with dipoles of 1.7 mm length (Section 4.1) is placed above a 6×6 AMC composed of patches of length equal to both 3 mm and 2.5 mm. The other AMC dimensions are the same as the ones used in the previous sections (see Section 4.1 or Section 4.3.1). Fig. 4.16 contains the current density observed when working at 35.5 GHz, the frequency at which the pattern splitting at broadside is most dramatic (see Section 4.1). For the AMC with patches of 3 mm, surface currents, revealing the presence of surface wave modes, appear on the patches perpendicular to the polarization of the antenna ($\hat{y}$ coordinate). When the AMC patches are smaller, the induced currents are mostly concentrated on the four central patches just below the antenna, which suggests the absence of bound modes travelling along the AMC surface. These phenomena support the eigenmode analysis presented in Section 4.3.1.

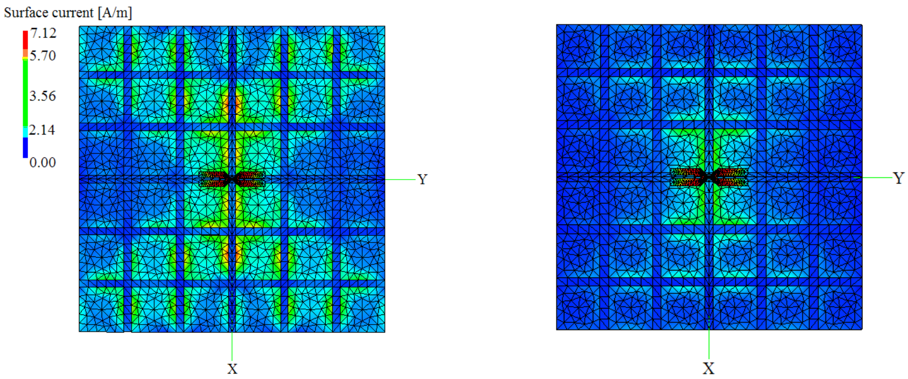

Figure 4.16 Current density on the antenna-AMC configuration when operating at f = 35.5 GHz. A 6x6 array of square patches with length 3 mm (left) and 2.5 mm (right) is used as a ground plane.

4.3.3 Summary

An eigenmode analysis based on the Method-of-Moments (MoM) technique has been carried out to study the wave modes supported by an AMC consisting of a backgrounded array of square patches. It reveals the existence of a bound mode whose propagation constant corresponds to a 180 $^\circ$ phase shift, at the frequency at which the splitting pattern problem is most dramatic. The excitation of such a bound mode results in surface currents induced on the AMC patches that can destructively contribute to the radiated E-field, producing secondary lobes or nulls in the radiation pattern. Besides this, it is shown that reducing the patches length of the AMC causes such trapped mode to appear at higher frequencies. It is worth noting that if an AMC with smaller patches is used to support the antenna, we will approach the range where the AMC reflection phase is $90^\circ \pm 45^\circ$ [17], instead of working with a reflection phase in the range $0^\circ \pm 90^\circ$. This explains why the patterns do not split [17] when working in the $90^\circ \pm 45^\circ$ range. In the following section we propose a surface that avoids the propagation of bound modes in the H-plane direction, and that allows us, at the same time, to tailor the propagation of the characteristic modes in the E-plane direction by adjusting the dimensions of the patches. This will allow us to work with a reflection phase in the $0^\circ \pm 90^\circ$

range without having bound modes distorting the radiation patterns. It will be shown that the new surface acts as a leaky-wave structure.

4.4 Rectangular non-periodic AMC

The problem of having surface waves propagating along an AMC ground plane has usually been solved by designing structures with simultaneous AMC and EBG characteristics at the operation frequency band [4], [14], [17]. The problems caused by the radiation produced when bound modes reach the edges of a finite structure, can also be minimized by using non-uniform tuning methods, as described in [50]. Here, a new surface acting as an AMC and, at the same time, as a leaky-wave structure with homogeneous phases along successive elements, is proposed (see Fig. 4.17). It consists of a rectangular array of patches with different lengths along the E-plane direction ($\hat{y}$ in Fig. 4.17). As shown below, truncating the surface in the H-plane ($\hat{x}$ direction in Fig. 4.17) avoids the propagation of surface waves in this direction. The central patches allow us to take advantage of the AMC properties to create a low-profile design, and the patches of different sizes away from the center help to create the guiding structure. This surface does not contain vias, making it easy to fabricate, and shows smaller dimensions than other conventional AMC structures.

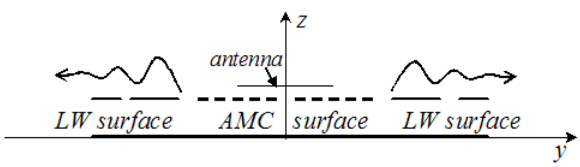

Figure 4.17 Combination of the AMC (central patches) and leaky mode (patches away from the center) phenomena in the same structure.

Section 4.4.1 shows how the modal features of the AMC ground plane studied in Section 4.3, can be easily modified in order to avoid the propagation of bound modes and take advantage, at the same time, of the radiation of the leaky modes traveling along the surface. Then, it is shown how with the new structure the radiation performances of the antenna-AMC group are strongly improved (Section 4.4.2).

4.4.1 Eigenmodes analysis

- Rectangular structure

According to the eigenmodes and currents study presented in Sections 4.3.1 and 4.3.2 respectively, a reduction of the AMC size in the direction perpendicular to the polarization of the antenna (H-plane) may avoid the propagation of the existing bound modes along this direction, avoiding the corresponding surface currents to appear. It is worth noting that, apart from the radiation problems related to surface waves, having trapped modes traveling along the AMC surface implies evanescent fields near the AMC that affect the input impedance of an antenna placed above the surface (see Section 2.2.5).
The Method-of-Moments approach described in Section 2.2.1 is applied again to perform the modal analysis of a linearly infinite array of backgrounded square patches. The geometry of the $\infty \times 2$ rectangular surface studied is shown in Fig. 4.18. Like in the infinite-by-infinite array studied in Section 4.3, L_p corresponds to the patches length and, d_x and d_y denote the distance between the array elements in the x and y directions, respectively. The dimensions of the elements composing the rectangular array are the same as the ones for the infinite by infinite surface from Section 4.3, i.e. the patches are 3 mm in length and the gap between them is equal to 0.5 mm.

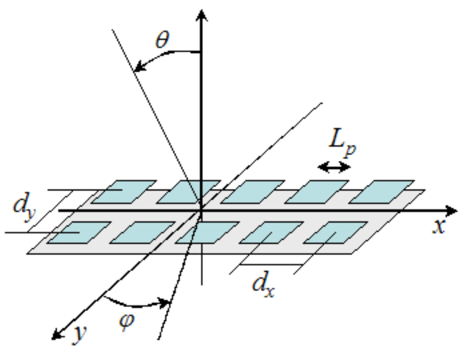

Figure 4.18 Geometry of the $\infty \times 2$ array of grounded patches under study.

The effect on the modal characteristics of the AMC produced when cutting the AMC surface in the H-plane direction, can be noticed from the dispersion diagrams shown in Fig. 4.19. It contains the dispersion diagram of the infinite-by-infinite array studied in Section 4.3 and the dispersion diagram in the ΓX path of the Brillouin zone for the rectangular array. Only the propagation in the ΓX path is analysed for the $\infty \times 2$ array because of the truncation in the $\hat{y}$ direction. The analysis for the linearly infinite array has been carried out with the MoM code developed at our laboratory [35], [36], in combination with the method described in Chapter 5 for the computation of the periodic Green's function. In Fig. 4.19, we observe that the bound mode corresponding to a 180 degrees inter-element phase shift appears at $f = 37GHz$ instead of $f = 35GHz$ when the array is truncated. Moreover, in the hypothesis of leaky waves (see the red line in the graph to the right in Fig. 4.19) propagating at around 35.5 GHz, frequency at which a strong dip in the pattern was observed at broadside (see Section 4.1), broadside leaky-wave radiation could be produced. It would help to solve the problem of splitting patterns observed in Section 4.1.

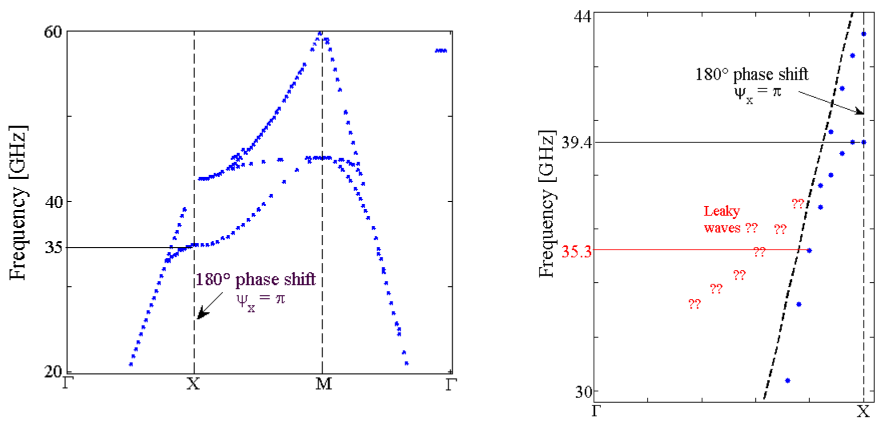

Figure 4.19 The $f - \psi$ dispersion diagrams for both a 2D-periodic (left) and a 1D-periodic (right) arrays of square patches of 3 mm length. Only the ΓX path is considered for the rectangular one.

- Aperiodic rectangular structure

As has been seen in Section 4.3.1, by changing the periodicity at which the patches are arranged in the array configuration, the modal characteristics of the AMC can be tailored. The geometry of a rectangular array with different periodicities along $\hat{x}$ and $\hat{y}$ is shown in Fig. 4.20. The different periodicities are obtained by using patches with different sizes along $\hat{x}$ and $\hat{y}$.

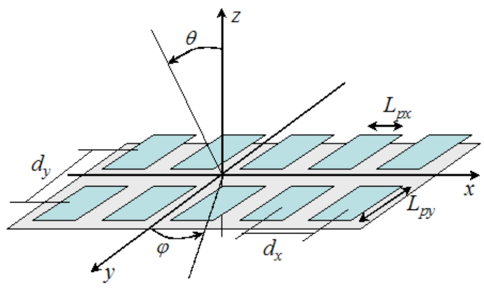

Figure 4.20 Geometry of the $\infty \times 2$ array of grounded patches of different lengths along the $\hat{x}$ and the $\hat{y}$ directions.

The dispersion diagrams in the ΓX path of the Brillouin zone, for the rectangular surface of square patches ($L_{px} = L_{py}$ =3 mm) (Fig. 4.18) and the one composed of patches of different sizes along $\hat{x}$ and $\hat{y}$ (L_{px} =2.5 mm, L_{py} =3 mm) (Fig. 4.20), are provided in Fig. 4.21. For the array of patches with length equal to 2.5 mm in the $\hat{x}$ direction, we observe two bound modes corresponding to a 180 degrees phase shift, which appear at higher frequencies than the 180 degrees bound mode supported by the array of 3 mm square patches. These dangerous trapped modes are moved again further from the useful antenna operation band around the AMC resonance (see Section 4.1).

The leaky waves supported by both structures have been studied (hypothetic interrogation lines in Fig. 4.21). Due to the truncation of the surfaces in the $\hat{y}$ direction (Fig. 4.18 and Fig. 4.20), only the ΓX path has been analysed. We remind that the ΓX path represents the propagation in 1D-periodic direction, i.e. $\psi_x = (0, \pi)$ and $\psi_y = 0$. The computation method described in Chapter 5 has been used in combination with the MoM code developed at

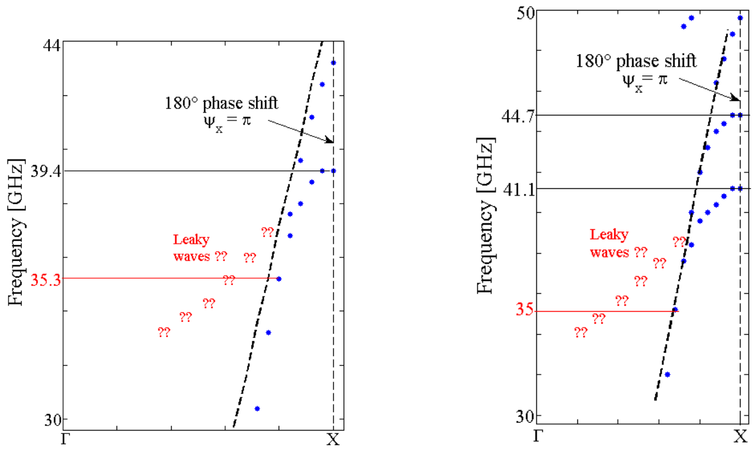

Figure 4.21 The $f - \psi_x$ dispersion diagrams in the ΓX path for a planar $\infty \times 2$ array of both square patches ($L_{px} = L_{py} = 3\,mm$) and patches of different sizes along the $\hat{x}$ and the $\hat{y}$ directions ($L_{px} = 2.5\,mm$ and $L_{py} = 3\,mm$).

our laboratory [35], [36]. When dealing with complex propagation constants, $k_{LW} = \beta - j\alpha$, the MoM impedance matrix Z (see Section 2.2.1) depends on the frequency f, the real and the imaginary parts of the phase shifts ($\psi_x = k_x d_x$, $\psi_y = k_y d_y$) between successive unit cells: $\beta_x\, d_x$, $\beta_y\, d_y$, and $\alpha_x\, d_x$, $\alpha_y\, d_y$, respectively. So, one more parameter, that is the imaginary part of the phase shifts $\alpha_x\, d_x$ or $\alpha_y\, d_y$, has to be taken into account in the computation of the eigenmodes of the structure (Section 4.2.1). The values of f, $\beta_x\, d_x$, $\beta_y\, d_y$ and $\alpha_x\, d_x$, $\alpha_y\, d_y$ that make the determinant of $Z(f, \beta_x\, d_x, \beta_y\, d_y, \alpha_x\, d_x, \alpha_y\, d_y)$ equal to zero correspond to the leaky eigenmodes of the structure. The $f - \beta_x d_x$ and the $f - \alpha_x d_x$ relations related to the ΓX path are plotted in Fig. 4.22 for the rectangular surface of square patches ($L_{px} = L_{py}$ =3 mm) (Fig. 4.18) and the one composed of patches of different sizes along $\hat{x}$ and $\hat{y}$ (L_{px} =2.5 mm, L_{py} =3 mm) (Fig. 4.20). It is seen that when the patches size is decreased along the $\hat{x}$ direction, the attenuation constants of the propagating leaky-waves are bigger for a given frequency. On the contrary, the phase constant β_x and therefore, the phase shift $\beta_x d_x$ between successive patches, becomes smaller for smaller patches. This means (see Section 4.2.3) that two wider beams, closer to each other, will appear in the radiation pattern. This will result in the merge of those beams, and in turn, lead to a higher directivity at broadside. As mentioned in Section 4.2.3, a single beam pointing at broadside can be reached when the ratio β/α is less or equal to 1. It is observed in Fig. 4.22 that the ratio obtained for the leaky waves propagating at around 35 GHz has decreased from 21.6 to 3.57, when the length of the patches has been reduced from 3 mm to 2.5 mm in the $\hat{x}$ direction. Although β is still bigger than α for the 2.5 mm case, the ratio rapidly approaches the condition $\beta/\alpha \leq 1$. A study of the leaky waves supported by a rectangular non-periodic surface of patches with lengths equal to 2 mm and 3 mm along $\hat{x}$ and $\hat{y}$, respectively, is being carried out. Some preliminary results show that the ratio β/α is even closer to the $\beta/\alpha \leq 1$ condition (single beam pointing at broadside) than for the rectangular array with patches 2.5 mm $\times$ 3 mm. This leads to think that reducing the dimensions of the patches of the non-periodic surface in the $\hat{x}$ direction will help us to obtain radiation patterns with a single beam pointing at broaside.

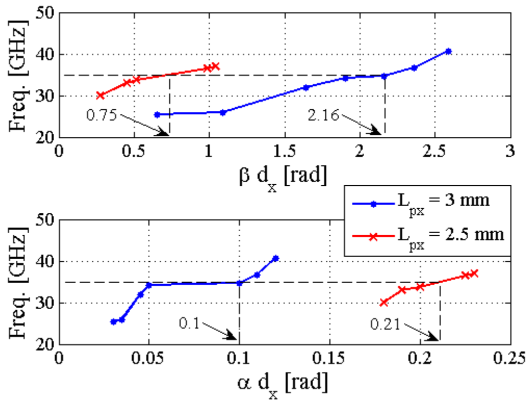

Figure 4.22 *The $f - \beta_x d_x$ and $f - \alpha_x d_x$ relations for a planar $\infty \times 2$ array of both square patches ($L_{px} = L_{py} = 3\,mm$) and patches of different sizes along the $\hat{x}$ and the $\hat{y}$ directions ($L_{px} = 2.5\,mm$ and $L_{px} = 3\,mm$).*

4.4.2 Directivity improvement at broadside

In view of the modal study carried out in Section 4.4.1, the double planar dipole presented in Section 4.1 is located above a rectangular AMC, which is afterwards made non-periodic, in order to overcome the problem of splitting patterns (Section 4.1). As it was mentioned at the beginning of this section, the new aperiodic surface acts as an AMC and as a leaky wave structure at the same time. The patches just below the antenna provide the AMC properties and the patches away from the center help to create a leaky wave surface.

Fig. 4.23 provides a top view of the double-dipole antenna placed above the 2×6 AMC obtained after reducing its dimensions in the H-plane. The patches length and the spacing between them are 3 mm and 0.5 mm respectively, with 1 mm space between the patches and the metal sheet.

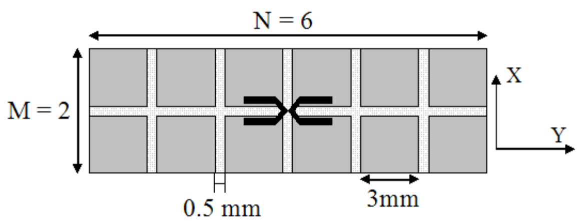

Figure 4.23 *Double-dipole antenna placed horizontally above a rectangular 2×6 AMC.*

When the 2×6 AMC is made non-periodic, the design shown in Fig. 4.24 results. The AMC consists now of patches of different sizes along the E-plane direction. The patch length is gradually decreased from the center of the structure along the $\hat{y}$ coordinate, and it remains the same along $\hat{x}$. The gap between the patches does not change and is equal to 0.5 mm (as in the previous AMCs). The central patches are square and their size L_c is fixed, depending on the desired AMC resonance frequency. In a first instance, it is 3 mm (the same as the patches length of the previous AMCs). The difference between sizes of contiguous patches L_{dec} is taken constant.

Reducing the AMC size in the direction perpendicular to the polarization of the antenna significantly improves the directivity achieved at broadside, especially at frequencies close to the AMC resonance (27.4 GHz). This is clearly observed in Fig. 4.25, which compares the input reflection coefficient and the directivity obtained when placing the dual-antenna with dipoles of $L = 1.7$ mm length above different AMCs: a square 6×6 AMC, a rectangular 2×6 AMC and two non-periodic AMCs. When comparing the 6×6 and the 2×6

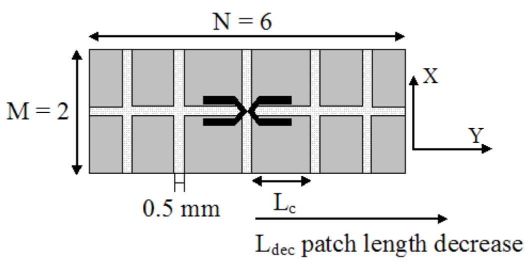

Figure 4.24 *Double-dipole antenna placed horizontally above a non-periodic 2×6 AMC.*

cases, an improvement of the directivity values achieved in the useful band is observed. While directivities from 9.7 dB (at the lowest useful frequency) to 6.7 dB (at the upper frequency end) were obtained over the 18.7% impedance bandwidth when using the 6×6 AMC, now values from 9 dB (at the lowest frequency) to 8.7 dB (at the highest frequency) are achieved over a 24.1% impedance bandwidth with the 2×6 AMC.

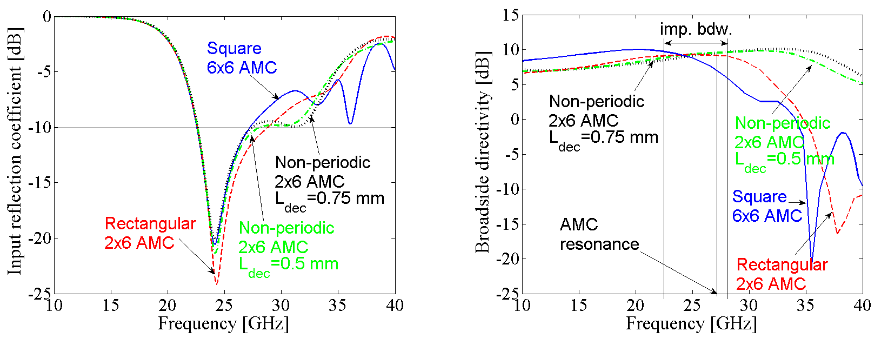

Figure 4.25 *S_{11} coefficient w.r.t. 50Ω (left) and broadside directivity (right) for a double-dipole antenna of 1.7 mm dipoles length horizontally placed above different AMCs.*

Fig. 4.25 (right plot, labeled 'non-periodic') also shows that breaking the periodicity of the AMC in the E-plane strongly improves the directivity achieved at frequencies beyond the AMC resonance. It is also observed that for bigger differences between patches, higher directivities are obtained. The double-dipole antenna put above the non-periodic AMC is always the one with dipoles of 1.7 mm length. When looking at the input reflection coefficient we observe some oscillations to the right of the antenna resonance when it is placed above the periodic 6×6 AMC surface, as evidenced for the planar bow-tie dipole antenna in Section 2.2.4. It is worth noting that these oscillations are not so strong when the antenna is located above the rectangular 2×6 AMC and above the aperiodic 2×6 surface. Because these AMC surfaces avoid the propagation of some of the bound modes travelling along the 6×6 AMC, at frequencies close to and beyond the AMC resonance, weaker evenescent waves may appear near the rectangular and the aperiodic AMCs, and therefore less oscillations may be observed in the input reflection coefficient according to the study carried out in Section 2.2.5. Nevertheless, we can say that the input impedance characteristics are not especially affected in terms of bandwidth. However, the directivity achieved at broadside is strongly improved.

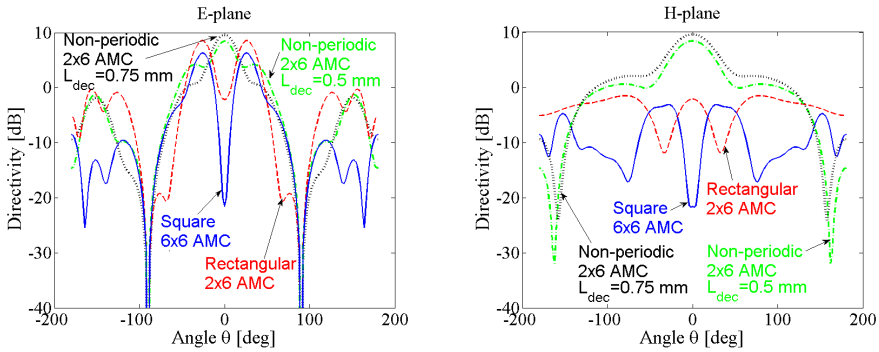

Figure 4.26 *Radiation patterns in the E-plane (left) and H-plane (right) at f=35.5 GHz, obtained for the double-dipole antenna of 1.7 mm dipoles length placed above different AMCs.*

The vertical cuts in both the E-plane and the H-plane at $f = 35.5$ GHz, when using the different AMCs for back-grounding the double-dipole antenna, are provided in Fig. 4.26. As presented in Section 4.1, the worst broadside directivity values are obtained at $f = 35.5$ GHz, when the antenna is placed above the 6x6 AMC. If the number of patches perpendicularly to the antenna are reduced, a clear improvement is observed at broadside, reducing the splitting effect. When looking at the cuts obtained with the non-periodic surfaces, we can see that the problem of splitting patterns is solved, reaching a quite high maximum at broadside. The same recovering effect is observed at frequencies between the AMC resonance (27.4 GHz) and 35.5 GHz, which will allow us to enlarge the useful bandwidth of the design (see Section 4.5).

4.4.3 Summary

A new ground plane acting as an AMC and, at the same time, as a leaky-wave structure with homogeneous phases along successive elements is shown to help to overcome the problem of splitting patterns at broadside. The new surface consists of a rectangular finite array of patches with decreasing length along the direction of the current flow in the antenna. The central patches allow to take benefir from the AMC features of the surface to create a low-profile design, and the patches of different sizes away from the center help to create the guiding structure. An eigenmodes analysis shows that the bound mode corresponding to a 180° phase shift, supported by the initial square periodic surface at the frequency at which the patterns split, is shifted to higher frequencies (out of band) when the AMC surface is truncated and made non-periodic. In addition, leaky-waves radiating at small angles from the broadside direction are supported by the non-periodic surface. They contribute constructively to the broadside directivity, producing patterns with one single main lobe pointing at broadside.

4.5 Final wideband low-profile design

In Section 4.4.2, the input-impedance characteristics obtained when placing a double-dipole antenna above different non-periodic and periodic AMCs have been provided. In a first instance, limited bandwidths, around 20%, have been obtained. Once the splitting problem is overcome, the antenna can be tuned closer to the AMC resonance (reflection phase in the $0^\circ \pm 90^\circ$ range [4]) in order to increase the input-impedance bandwidth. To do so, we can vary either the length of the dipoles of the antenna or the dimensions of the AMC patches. Here, the size of the square central patches of a non-periodic design has been increased from 3 mm to 3.25 mm in order to bring the AMC resonance closer to the antenna resonance. The length difference between the successive patches along the antenna polarization direction is 0.5 mm. They are all equally spaced, with a 0.5 mm gap. A distance equal to 1 mm separates the patches from the bottom metal sheet. The double-dipole antenna is placed at 1.5 mm from the metal sheet.

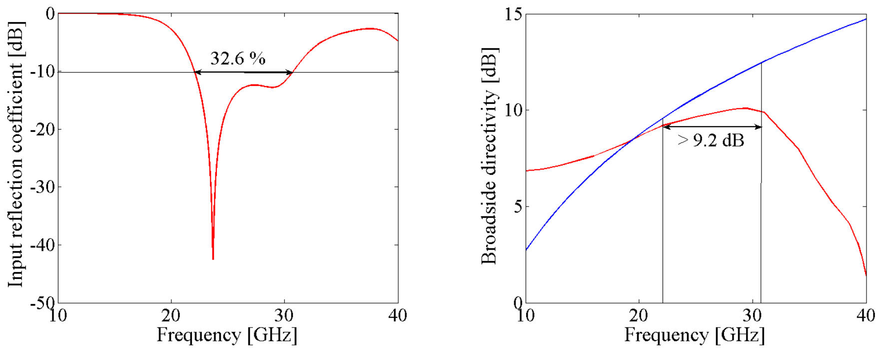

Figure 4.27 *S_{11} coef. w.r.t. 50Ω (left) and broadside directivity (right) for the final design (red line). The blue curve in the right plot is the theoretical directivity achievable with such a final design.*

Fig. 4.27 provides the performances obtained with such a design. It provides more than 9.2 dB of broadside directivity and a reflection coefficient better than -10 dB over a 32.65% bandwidth. The total antenna height is $0.15\lambda_{min}$, where λ_{min} corresponds to the wavelength at the highest frequency (the worst case).

Fig. 4.28 shows vertical cuts in the radiation patterns at f=23.6 GHz (frequency of minimum S_{11}) and f=28 GHz for the final proposed design. Good directivity performances are achieved in the whole useful band, with a maximum always observed at broadside.

Finally, Fig. 4.27 compares the directivity obtained (red line) with the theoretical one (blue line) achievable with such a physical area ($1.9\lambda_{min} \times 0.7\lambda_{min}$), as given by the expression $D = A_{eff}\, 4\,\pi/\lambda^2$. The directivity obtained over the useful band is almost flat. It can be seen that, at the lowest frequency, the directivity is very close to the maximum achievable, while a 2.5 dB lag is observed at the upper frequency end.

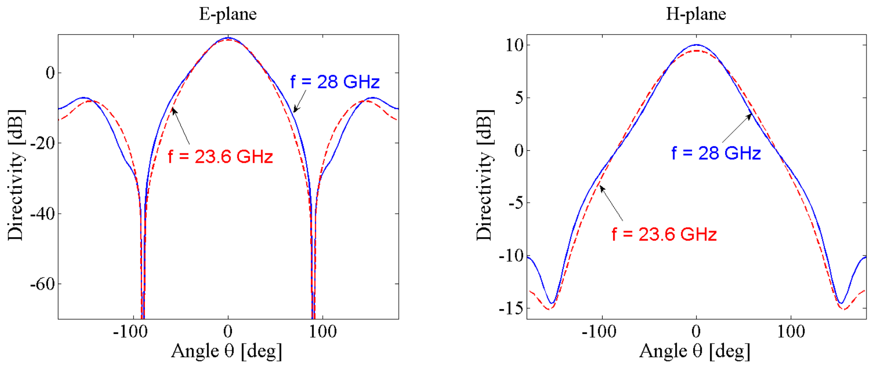

Figure 4.28 *Radiation patterns in vertical planes at two frequencies comprised in the useful band provided by the final proposed design.*

To end, we would like to notice that the new aperiodic surface has also been used to improve the broadside directivity of a Tulip antenna [51]. The patterns also split at broadside when the Tulip antenna is placed above a periodic AMC consisting of an array composed of square patches. The rectangular non-periodic structure has helped to avoid this problem.

4.6 Influence of the AMC's ground plane size

It is interesting to study the influence of the size of the AMC's ground plane on the performances achieved. Fig. 4.30 provides the input impedance characteristics and the broadside directivity obtained for the design presented in Section 4.5, with a ground plane larger than the area taken by the patches of the AMC. The results for a ground plane of size equal to 6×6 times the central patches length (3.25 mm in this case), and for an infinite ground plane are presented. The meshes of such designs are shown in Fig. 4.29.

The performances obtained (see Fig. 4.30) are compared with the ones for the design presented in Section 4.5, which contains a ground plane of size equal to the area taken by the AMC patches. We observe that the input impedance characteristics do not change substantially after enlarging the AMC's ground plane. When looking at the broadside directivity obtained at frequencies smaller than 35 GHz, we see that enlarging the ground plane results in higher directivity values at those frequencies. However, smaller direc-

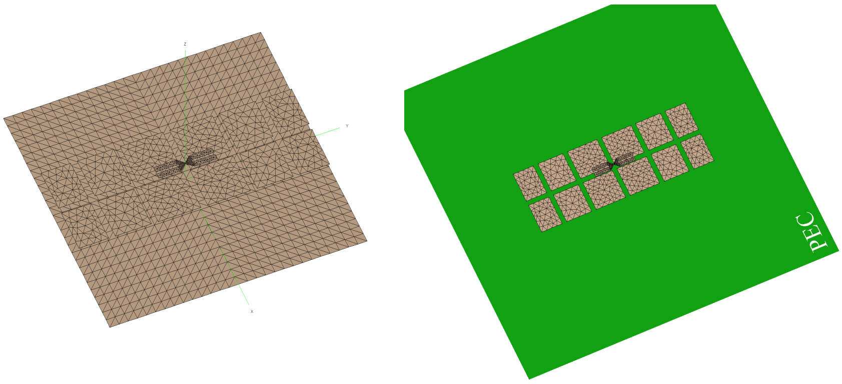

Figure 4.29 *Double-dipole antenna placed above an aperiodic AMC with: a ground plane of size equal to 6×6 times the central patches length (left), and an infinite ground plane (right).*

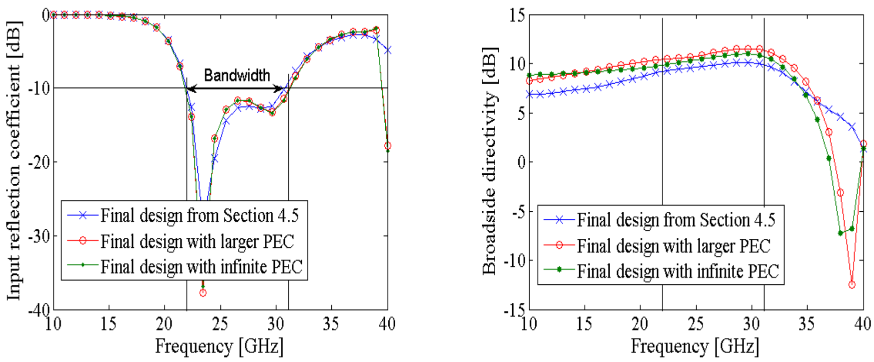

Figure 4.30 *S_{11} coefficient w.r.t. 50Ω (left) and broadside directivity (right) for a double-dipole antenna placed above an aperiodic AMC with a ground plane of different sizes.*

tivity values are obtained at higher frequencies when the ground plane is enlarged. A strong dip is observed around 39 GHz. It is worth saying that a dip also appears for the original design (the one from Section 4.5), but at higher frequencies (around 41 GHz). This means that the dip has been shifted down in frequency when enlarging the ground plane, but it is still out of the useful band. The directivity values obtained in the useful impedance bandwidth (which remains almost the same) are better with a bottom ground plane larger. The minimum broadside directivity obtained in the useful band has increased from 9.2 dB, for the original design, to around 10 dB when the metallic bottom ground plane is larger. The relative impedance bandwidth has been slightly enlarged from 32.6% to 33.9%.

A simple new method to compute the periodic GF

5

5.1 Introduction

It is well known that the scalar Green's function associated to a periodic planar array of sources represents a challenge in terms of convergence of series, especially if treating complex wave modes. We present a novel solution based on the observation that, once the contribution of the nearest dipoles is extracted, the remaining part of the Green's function must be a very smooth function of spatial coordinates. Hence, on-plane or near-plane solutions can be extrapolated from solutions obtained further away from the dipole plane. The resulting method is extremely simple to implement and can be applied to both real and imaginary phase shifts, the latter being important for the analysis of leaky wave structures.

Traditional techniques devoted to the simulation of periodic structures difficultly accomodate complex-wave modes, often represented by complex wave numbers $k_{LW} = \beta - j\alpha$. This is mainly due to the difficulty of computing the related Green's function, which may be very slowly convergent in the case of the spectral solution and divergent for the spatial one. To our knowledge, very little information concerning the evaluation of the periodic Green's function for complex phase shifts, is found in literature. This problem has recently be tackled by [52]. An overview of the main acceleration techniques is provided in [52] and [53], and the possibility of treating complex phase shifts with the different existing techniques is discussed. The case of 3-D problems with 1-D periodicity has been studied in detail in [52]. The

Kummer-Poisson's decomposition [54] is optimized and accelerated with the Shank's transformation in [54], [55] and with the ρ-algorithm in [56]. A comparison with the Ewald's method [57] and the Veysoglu integral representation [58] reveals that the Kummer-Poisson's solution proposed in [52] is more efficient when dealing with accuracies lower than 10^{-5}. For higher accuracies, the Ewald method works better. For 3-D problems with 2-D periodicity, Ewald's method is shown to be more efficient for errors smaller than 10^{-3}. In the present work, we propose a new very simple method for evaluating the periodic Green's function for real and complex phase shifts in 3-D problems with 2-D and 1-D periodicity. We first expose the problems found when trying to solve the periodic Green's function for complex phase shifts. In Section 5.3 we describe the new method proposed, which is followed in Section 5.4 by a discussion regarding the accuracy of the results obtained. A parametric analysis provides an idea of the expected accuracy. Accuracies of the order of $10^{-7.5}$ and around 10^{-11} are easily achieved for complex and real phase shifts, respectively. A conclusion is drawn at the end of the chapter.

5.2 Problem statement

- 3-D problems with 2-D periodicity

We consider a two-dimensional array of sources repeated periodically (see Fig. 5.1). The distance between the sources is d_x and d_y along the $\hat{x}$ and $\hat{y}$ directions, respectively. The propagating constants of the waves travelling in these directions are denoted by k_{x0} and k_{y0}, respectively.

The spatial Green's function related to an infinite array along $\hat{x}$ and $\hat{y}$ can be written as

$$G_r(\vec{r}) = \sum_{n=-\infty}^{\infty} \sum_{m=-\infty}^{\infty} \frac{e^{-jkR_{mn}}}{4\pi R_{mn}} e^{-jmk_{x0}d_x} e^{-jnk_{y0}d_y} \tag{5.1}$$

where k stands for the free-space wave-number, and R_{mn} is the distance between the observation point $\vec{r} = (x, y, z)$ and the mnth source point $\vec{r}\,' = (md_x, nd_y, 0)$. The phase shift between two adjacent cells in the x and y directions are represented by ψ_x and ψ_y, respectively. They are related to the corresponding propagating constants, k_{x0} and k_{y0}, as $\psi_x = k_{x0}\, d_x$ and $\psi_y = k_{y0}\, d_y$.

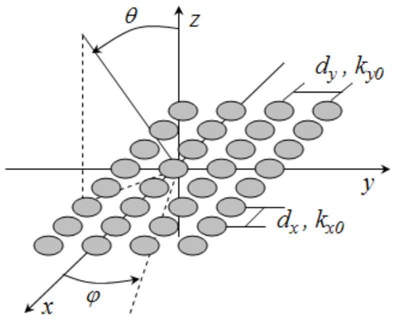

Figure 5.1 *Geometry of the 2-D infinite array of sources under study.*

When k_{x0} and k_{y0} are complex, they are usually written as $k_{x0} = \beta_x - j\alpha_x$ and $k_{y0} = \beta_y - j\alpha_y$, where the real numbers β_x, β_y and α_x, α_y stand for the propagation and the attenuation constants in the $\hat{x}$ and $\hat{y}$ directions, respectively. From (5.1) we can see that complex phase shifts cause an exponentially diverging term to appear, that is $e^{-m\alpha_x d_x}$ in the $\hat{x}$ direction and $e^{-n\alpha_y d_y}$ in the $\hat{y}$ direction.

On the contrary, the spectral series (or plane-wave series) remains convergent for complex phase shifts. The infinite periodic Green's function can be expressed in the spectral domain by:

$$G_p(\vec{r}) = \sum_{n=-\infty}^{\infty} \sum_{m=-\infty}^{\infty} \frac{e^{-jk_x^m x} e^{-jk_y^n y} e^{-jk_z^{mn}|z|}}{2jd_x d_y k_z^{mn}} \tag{5.2}$$

with the following definitions for the wavenumbers:

$$k_x^m = k_{x0} + \frac{2\pi m}{d_x} \tag{5.3}$$

$$k_y^n = k_{y0} + \frac{2\pi n}{d_y} \tag{5.4}$$

$$(k_z^{mn})^2 = k^2 - (k_x^m)^2 - (k_y^n)^2 \tag{5.5}$$

For complex k_{x0}, k_{y0} values, the resulting attenuation-constant exponentials, namely $e^{-\alpha_x x}$ or $e^{-\alpha_y y}$, are independent from m, n, leading to a convergent spectral series (5.2). Nevertheless, it converges very slowly when the observation point is very close to the array plane due to the $e^{-jk_z^{mn}|z|}$ factor, which results in a $e^{-2\pi m|z|/d_x}$ or $e^{-2\pi n|z|/d_y}$ exponential when m or n are large.

- 3-D problems with 1-D periodicity

Let us consider here a one-dimensional infinite array of sources repeated periodically (see Fig. 5.2) along the $\hat{x}$ direction. The periodicity of the sources is denoted by d_x and the propagation constant of the waves travelling in the direction of the array, i.e. $\hat{x}$, is denoted by k_{x0}.

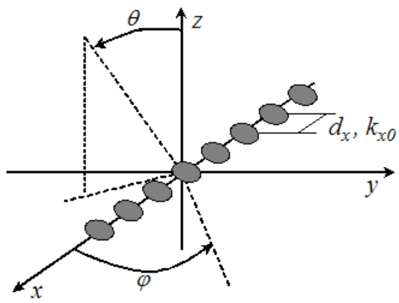

Figure 5.2 *Geometry of the 1-D infinite array of sources under study.*

The spatial Green's function related to a one-dimensional array infinite along $\hat{x}$ can be written as

$$G_r(\vec{r}) = \sum_{m=-\infty}^{\infty} \frac{e^{-jkR_m}}{4\pi R_m} e^{-jmk_{x0}d_x} \tag{5.6}$$

where k stands for the free-space wave-number, and R_m is the distance between the observation point $\vec{r} = (x, y, z)$ and the mth source point $\vec{r}\,' = (md_x, 0, 0)$. The phase shift between two adjacent cells in the x direction is represented by ψ_x and it is related to the corresponding propagating constant k_{x0}, as $\psi_x = k_{x0}\, d_x$.

As happens in 2D-periodicity problems, for the case of complex propagating constants, the spatial series (5.6) does not converge. When k_{x0} is complex, usually written as $k_{x0} = \beta_x - j\alpha_x$, where the real numbers β_x and α_x stand for the propagation and the attenuation constants in the $\hat{x}$ direction, the exponentially diverging factor $e^{-m\alpha_x d_x}$ appears in (5.6).

On the contrary, the spectral series remains convergent for complex phase shifts. The one-dimensional infinite periodic Green's function can be expressed in the spectral domain with the help of the zero-order Hankel function of second kind $H_0^{(2)}$:

$$G_p(\vec{r}) = \frac{1}{4\,j\,dx} \sum_{m=-\infty}^{\infty} e^{-j\,k_x^m\,x} H_0^{(2)}(\gamma_m\,R) \tag{5.7}$$

where $R = \sqrt{y^2 + z^2}$ is the distance to the array axis and

$$\gamma_m^2 = k^2 - (k_x^m)^2 = k^2 - \left(\frac{\psi_x}{d_x} + \frac{2\,\pi\,m}{d_x}\right)^2 \tag{5.8}$$

For real phase shifts ψ_x, γ_m can be a real $\left(\gamma_m^2 > 0\right)$ or a pure imaginary $\left(\gamma_m^2 < 0\right)$ value, with $Im\{\gamma_m\} \leq 0$, depending on the index m. For real values of γ_m, we obtain propagating cylindrical waves described by the Hankel functions $H_0^{(2)}$. For pure imaginary values of γ_m, the Hankel function becomes a rapidly decaying modified Bessel function of the first kind (Eq. (5.9)), which represents evanescent cylindrical waves.

$$H_0^{(2)}\left(\gamma_m\,R\right) = H_0^{(2)}\left(-j\,\alpha'_m\,R\right) = \frac{2\,j}{\pi} K_0\left(\alpha'_m\,R\right) \tag{5.9}$$

with $\alpha'_m = \sqrt{-\gamma_m^2}$ real and positive.

For imaginary phase shifts ψ_x, the Hankel function is evaluated for complex γ_m values. The convergence of (5.7) is exponential for both real and imaginary phase shifts. Nevertheless, it converges very slowly when the observation point is very close to the array axis, i.e. R tending to 0.

In the following sections, we present a new method that combines both computation approaches, spatial and spectral, in order to obtain a simple way to compute the periodic Green's function for complex propagating constants at any distance from the array plane (2-D periodicity problems) or the linear-array axis (1-D periodicity problems). The results exposed in the following sections correspond to the 2D-periodicity case. The parameters tendency and the nature of the results is the same for the 1-D periodicity problem. For simplicity in the exposition of the results, we assume in this study real propagating constants in the $\hat{x}$ direction. The behavior of the method remains the same when considering both complex k_{x0} and k_{y0} values.

5.3 New computation method

The proposed method is based on the observation that, once the contributions of the nearest few source points are extracted from the Green's function, a very smooth function of the distance from the array plane, denoted here by $F(z)$, is obtained. From there, the idea consists of extrapolating the G_p values calculated spectrally at different vertical distances z_i from the array plane (2-D periodicity), to the G_p values for smaller distances z_{ob}, down to $z_{ob} = 0$ (Fig. 5.3), by means of the $F(z)$ function.

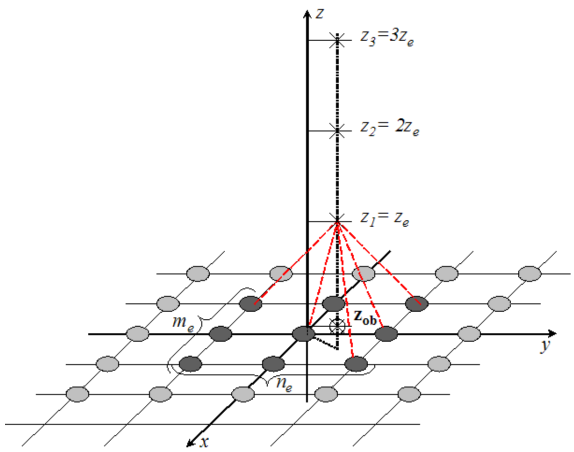

Figure 5.3 *Scheme of the extrapolation procedure. The contributions of the (m_e, n_e) sources, presented in a darker colour, are extracted from the spectral G_p's calculated at distances z_1, z_2 and z_3. The resulting function is then extrapolated to z_{ob}.*

Fig. 5.4 shows the scheme of the extrapolation procedure carried out in the 1D-case.

An extremely simple procedure is then obtained:
1) Compute the Green's function in the spectral domain (5.2) at different vertical distances z_i from the array plane : $G_p(z_i)$.
2) Extract from $G_p(z_i)$ the spatial contributions G_r of the few closest sources (m_e,n_e) at z_i:

$$G_p(z_i) - G_r(z_i)|_{m_e,n_e} = F_i \tag{5.10}$$

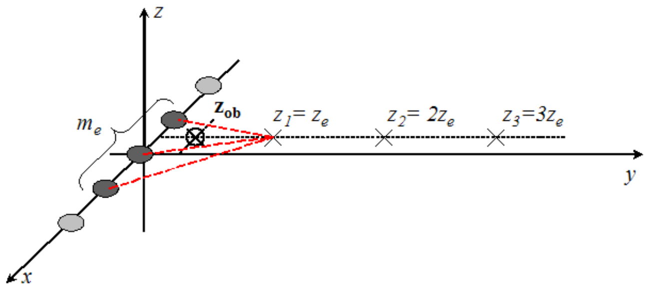

Figure 5.4 *Scheme of the extrapolation procedure carried out. The contributions of the m_e sources, presented in a darker colour, are extracted from the spectral G_p's calculated at distances z_1, z_2 and z_3, for extrapolating at z_{ob}.*

The indices (m_e,n_e) denote the finite number of terms used to compute the extracted sum computed as in (5.1).
3) Extrapolate F_i to the desired height z_{ob}, smaller than the z_i heights, to obtain F_{ob}.
4) Reintroduce the spatial contributions extracted in point (2) at the observation distance z_{ob}, in order to restore the complete Green's function:

$$G'_p(z_{ob}) = F_{ob} + G_r(z_{ob})|_{m_e,n_e} \tag{5.11}$$

It is worth noticing that the number of terms m, n used to calculate the spectral G_p's (5.2), in the first step, has to be sufficient regarding the precision desired. The number of terms necessary for achieving a specified precision p (error smaller than 10^{-p}) in the computation of (5.2) can be approximated analytically with the expressions:

$$n \geq \frac{d_y\, p\, ln10}{2\pi|z|} \tag{5.12}$$

$$m \geq \frac{d_x\, p\, ln10}{2\pi|z|} \tag{5.13}$$

which result from the evaluation of the exponential $e^{-jk_z^{mn}|z|}$ in (5.2) for large m and n indices, so that it reaches a value smaller or equal to 10^{-p}:

$$e^{-jk_z^{mn}|z|} \; (n\to\infty) \quad \rightsquigarrow \quad e^{-2\pi n|z|/d_y} \leq 10^{-p} \tag{5.14}$$

$$e^{-jk_z^{mn}|z|} \; (m\to\infty) \quad \rightsquigarrow \quad e^{-2\pi m|z|/d_x} \leq 10^{-p} \tag{5.15}$$

The expressions (5.14) and (5.15) also show the dependence of the computational load on the distance $|z|$ from the array plane.

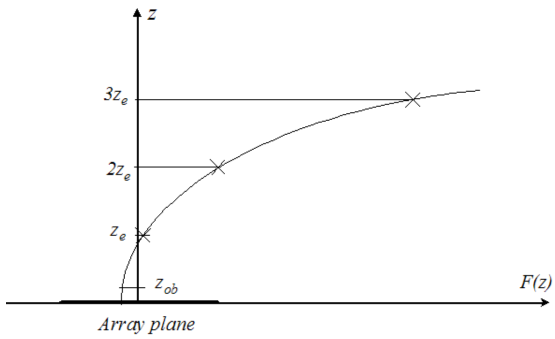

Figure 5.5 *An even-order polynomial is used as extrapolation function after extracting the spatial contributions of the closest sources.*

The smooth function $F(z)$, resulting from the extraction of singularities, can be represented by an even-order polynomial model (see Fig. 5.5), since the Green's function must be even w.r.t. z. If the extrapolating polynomial is written as

$$F(z) = c_0 + c_1 z^2 + c_3 z^4 + ... + c_N z^N \tag{5.16}$$

with N an even positive number. The c_i's are required to satisfy the linear equation [59]:

$$\begin{bmatrix} 1 & z_1^2 & z_1^4 & .. & z_1^N \\ 1 & z_2^2 & z_2^4 & .. & z_2^N \\ : & : & : & & : \\ 1 & z_N^2 & z_N^4 & .. & z_N^N \end{bmatrix} \begin{bmatrix} c_1 \\ c_2 \\ : \\ c_N \end{bmatrix} = \begin{bmatrix} F_1 \\ F_2 \\ : \\ F_N \end{bmatrix} \tag{5.17}$$

Thus, the knowledge of the Green's function at two or three heights z_i, for example, z_e, $2\,z_e$ or z_e, $2\,z_e$ and $3\,z_e$, enables an extrapolation assuming a second and fourth-order models, with a system (5.17) composed of two and three equations, respectively. The F_i values in the right vector correspond to the ones obtained in the Step 2 of the procedure. The coefficients c_i can then be determined from Eq. (5.17) and the extrapolation to the desired z_{ob} values can also then be performed (Step 3).

5.4 Discussion and results

The relative error ϵ between the Green's function value obtained with the extrapolation method and the one resulting from the spectral solution (5.2) has been calculated.

$$\epsilon = |G_p(z_{ob}) - G'_p(z_{ob})| / |G_p(z_{ob})| \tag{5.18}$$

The reference solution $G_p(z_{ob})$ is calculated with the same precision p as the spectral values $G_p(z_i)$ used to perform the extrapolation. The spectral series are computed with precision $p = p' + 1$, where p' corresponds to the order of the desired error $\epsilon \leq 10^{-p'}$. It is important to notice that the error ϵ depends on both the error incurred when computing the spectral G_p values, from which we extrapolate, and the error associated to the extrapolation procedure. The error due to the spectral G_p computations is related to the finite number of terms m, n used to calculate (5.2), as well as the distances ze, $2\,ze$ and $3\,ze$ at which (5.2) is calculated. The error due to the extrapolation procedure is also related to the distance z_e from which we extrapolate, together with the number of spatial contributions extracted before extrapolation, and the order of the polynom used to extrapolate. A parametric study is provided below to better show the evolution and dependence of the error on those parameters. The 2-D array presented in Fig. 5.1 with $d_x = d_y = 0.4\lambda$, where the wavelength λ is equal to 1, is studied. Our goal is to find a suitable combination of parameters so that an error $\epsilon \leq 10^{-5}$, small enough for common numerical purposes, is achieved, with a computational complexity as small as possible. The latter is evaluated here in relation to the number of terms (m, n) in the double sum (5.2), (m, n) being the summation limit parameters $\pm m$, $\pm n$ in (5.2), which results in a total number of terms $(2m + 1) \times (2n + 1)$.

5.4.1 Spatial singularities extraction

The number of extracted terms given by m_e, n_e has to be limited for complex propagating constants, because the spatial sum to extract diverges in that case. Hence, the larger the attenuation constant α_x, α_y, the fewer terms can be extracted without numerical difficulties associated with the extraction and introduction of very large spatial contributions. A very simple rule regarding the number of extractions is obtained by noticing that, versus m or n, the extracted contributions first decrease, because of the $1/R_{mn}$ behaviour (see Eq. (5.1)), and then increase because of the exponential behaviour. A safe choice consists of stopping the series when the exponential behaviour starts to be noticeable; i.e. when successive terms reach a minimum value. Then, a threshold of the number of extractions is applied as a function of α_x or α_y by searching the minimum of the diverging series:

$$\frac{\partial}{\partial m}\frac{e^{-m\alpha_x d_x}}{m}|_{m=m_e} = 0 \tag{5.19}$$

$$\frac{\partial}{\partial n}\frac{e^{-n\alpha_y d_y}}{n}|_{n=n_e} = 0 \tag{5.20}$$

The threshold, which avoids the divergence of the spatial series to extract, corresponds then, to the nearest inferior integer of $1/(\alpha_x\, d_x)$ or $1/(\alpha_y\, d_y)$, with a minimum equal to 2 and a maximum equal to half the number of spectral terms. If both extracted and re-introduced source contributions are considered (steps 2 and 4 above) it can be shown that the denominators of (5.19) and (5.20) should be m^γ and n^γ, respectively, where γ increases with the order of the extrapolation technique. In that case, the minimum occurs for $m \sim \gamma/(\alpha_x\, d_x)$ and $n \sim \gamma/(\alpha_y\, d_y)$. For second-order extrapolation, we have $\gamma = 5$.

5.4.2 Extrapolation distance

Extrapolating from distances z_e closer to the observation point (Fig. 5.3), improves the accuracy of the extrapolation itself. But is is worth noticing that it implies a higher number of spectral terms in (5.2). Hence, it is important to choose an extrapolation distance z_e such that it offers the required accuracy with a minimal computational load.

This is evidenced in Figs. 5.6 and 5.7, which show the relative error obtained at a given observation point, ($x/d_x = 0.5, y/d_y = 0.5, z_{ob}/d_y = 0.0025$), for extrapolation from different heights z_e/d_y, and consequently $2z_e/d_y$ and $3z_e/d_y$ for the second and third extrapolating points (4th order polynomial extrapolation), at $(x/d_x = 0.5,\ y/d_y = 0.5)$. It is presented together with the number of terms needed to compute the spectral G_p used to extrapolate from such distances z_e/z_{ob} to ensure a sufficient given accuracy $p = p' + 1$ in Eqs. (5.12), (5.13), where p' is the desired method accuracy and equal to 5 in this case. This study has been carried out for real (Fig. 5.6) and complex (Fig. 5.7) values of k_{x0}, k_{y0}, with big imaginary parts $\alpha_x d_x$, $\alpha_y d_y$ equal to 1 (the maximum and worst case considered in this work). The number of singularities extracted is given by $m_e = n_e = 2$, the minimum value used by the extrapolation method.

For the case of real phase shifts, the error is also provided for an extrapolation performed with a polynom of 2nd order. A 2nd order extrapolation implies the computation of the spectral G_p for 2 points, i.e. z_e/d_y and $2z_e/d_y$, instead of 3. However, it is interesting to notice that the additional computational load that represents a higher order extrapolation, 4th in this case, can be considered negligible, especially when one knows that computation at larger heights requires fewer terms. We can observe in Fig. 5.6 that high accuracies are obtained for both extrapolating polynoms.

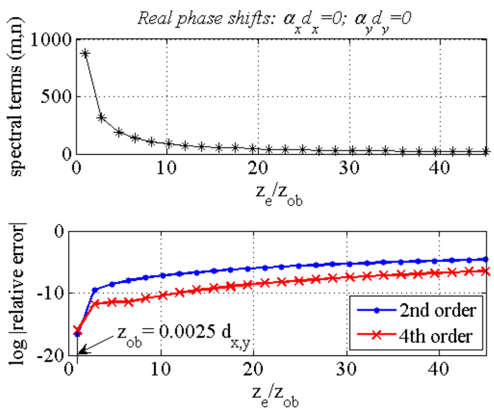

Figure 5.6 *Bottom: error incurred for real phase shifts $\psi_{x0} = \beta_x d_x$, $\psi_{y0} = \beta_y d_y$, versus distance from which extrapolation is carried out. Top: number of spectral terms needed to achieve a precision $p = p' + 1 = 6$ in the G_p computations at the different distances. The number of extracted source points $m_e = n_e$ is equal to 2.*

In Fig. 5.7 we compare the error obtained with a fourth-order extrapolation for different combinations of real and complex phase shifts ψ_{x0}, ψ_{y0}: both real ($\alpha_x d_x = \alpha_y d_y = 0$), one of them complex ($\alpha_y d_y = 1$) and both complex ($\alpha_x d_x = \alpha_y d_y = 1$). It is seen that when dealing with complex phase shifts less precision is obtained. Nevertheless, still high accuracies are achieved, even for both complex phase shifts in $\hat{x}$ and $\hat{y}$ directions.

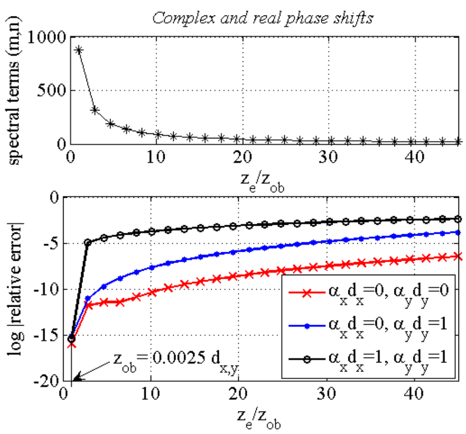

Figure 5.7 *Error incurred for different combinations of real and complex ψ_{x0}, ψ_{y0}, versus distance from which extrapolation is carried out. The number of spectral terms needed to achieve a precision $p = p' + 1 = 6$ in the G_p computations at the different distances, is also provided. The number of extracted source points $n_e = m_e$ is equal to 2.*

We can see then, from Figs. 5.6 and 5.7, that the extrapolation distance has to be fixed before applying the extrapolation method. It has been observed that extrapolating from a distance $z_e = d_y/40 = 0.025\,d_y$ provides a good tradeoff between the accuracy achieved and the computational load.

5.5 Final results

To end this work, we provide the performances achieved with the new extrapolation method. We have first summarized the accuracies achievable versus α_y, together with the number of extractions carried out for such α_y. Fig. 5.8 shows the error vs. the imaginary part, obtained with a 4th-order extrapolation model, performed from distances $z_e/d_y = 0.025$, $2 * z_e/d_y$ and $3 * z_e/d_y$. The number of singularities extracted is dependent on α_y and the computation charge is $m = n = 88$ terms. For complex phase shifts with imaginary parts equal to 1, an accuracy of the order of $10^{-7.5}$ is achieved. For real phase shifts, an error around 10^{-11} is easily obtained.

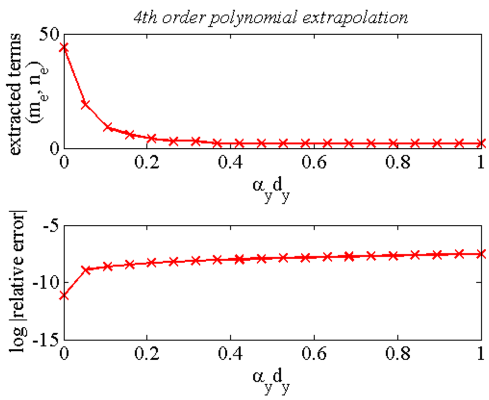

Figure 5.8 *Error incurred vs. the imaginary part of complex phase shifts:* $\psi_{y0} = \beta_y d_y - j\alpha_y d_y$*. The number of extractions is dependent on* α_y *according to* $1/(\alpha_y d_y)$*. The observation point is at distance* $z_{ob}/d_y = 0.0025$*, extrapolated from* $ze/d_y = 0.025$*, with a computation charge of* $m = n = 88$ *spectral terms.*

The error incurred at different distances z_{ob}/d_y from the array plane (see Fig. 5.9) is finally provided. The 4th order polynomial extrapolation is performed from the Green's function values calculated at distances $z_e/d_y = 0.025$, its double and its triple values. The number of singularities extracted is dependent on α_y according to the nearest inferior integer of $1/(\alpha_y d_y)$. We can see that, even if, as expected, the error increases for observation positions tending to 0 (on-plane situation), the accuracies achieved are around $10^{-7.5}$, when only one propagating constant is complex. We have also included the accuracies obtained when both k_{y0} and k_{x0} are complex, with large imaginary parts $\alpha_y = 1/d_y$ and $\alpha_x = 1/d_x$, respectively. Smaller accuracies are obtained, $10^{-3.7}$, but still good enough when treating numerical problems for imaginary parts of phase shifts smaller than 1.

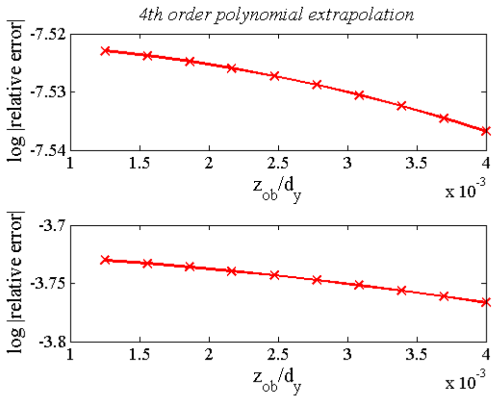

Figure 5.9 *Error incurred at different distances z_{ob}/d_y from the array plane, for complex phase shifts in only the $\hat{y}$ direction (top) and in both $\hat{x}$ and $\hat{y}$ directions (bottom). The minimum extrapolation distance is $z_e/d_y = 0.025$ and the number of extractions corresponds to $1/(\alpha_y\, d_y)$. Phase shifts imaginary parts, $\alpha_y\, d_y$, equal to 1 are considered.*

5.6 Conclusion

A very simple and accurate method for the computation of the periodic Green's function (G_p), evaluated for complex phase shifts, has been developed and presented here. It consists of extrapolating the G_p's calculated spectrally at different distances from the array plane, to the G_p for smaller distances, where the spectral G_p computation is very slowly convergent. Before extrapolating, the contribution of the closest source points is spatially extracted in order to produce smoother functions. After the singularities extraction, a fourth-order polynomial extrapolation is performed. Finally, the sources contributions extracted are reintroduced to obtain the complete G_p. Accuracies of the order of $10^{-7.5}$ are easily obtained when extrapolating from distances $z_e/d_y = 0.025$ and its double and triple values, using $m \times n = 88 \times 88$ terms in the computation of the spectral G_p values. The method can also be applied for real phase shifts and both complex ψ_{x0}, ψ_{y0}, achieving accuracies of the order of 10^{-11} and $10^{-3.7}$, respectively, with the same computational load. It is worth noticing that the latter accuracy concerns phase shifts with large imaginary parts equal to 1. The biggest imaginary parts we have dealed with in Section 4.4.1 are values around 0.4. For the case of complex phase shifts, the number of extracted singularities has to be limited to the nearest integer of $m_e = n_e = 1/(\alpha_y\, d_y)$, in order to control the error incurred. As a final comment, notice that the number of spectral terms can be reduced by using the Levin acceleration technique [60].

Passive RFID tag based on AMCs

6

6.1 Introduction

Radio-frequency identification (RFID) is a rapidly developing wireless technology used for the automatic identification of objects by exploiting the modulated reflectivity of a tag. In a RFID system, data is then exchanged between a reader and a tag (Fig. 6.1). The identification data is contained in an IC chip that is connected to the tag antenna. Data transfer in passive RFID systems is achieved by means of backscatter modulation. RFID technology is already being used in a large range of applications [61].

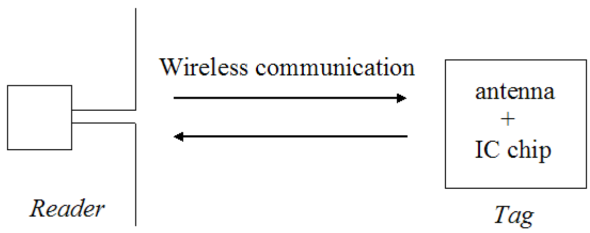

Figure 6.1 *RFID system scheme.*

A number of frequencies have emerged through technology developments and agreements with regional radio regulators that can be used for radio frequency identification (RFID). A number of these frequencies fall under regulations specified for industrial, scientific and medical applications, restricting the amount of power that can be used and, thus, the range of the transmission. The European spectrum for the operation of RFID at UHF frequencies goes from 865 MHz to 868 MHz. The regulatory standard relevant to UHF RFID is the ETSI *EN 302 208*. It proposes UHF covering 100mW, 500mW and 2W devices in the 865.0-868.0 MHz band, with 200kHz channels and a mandatory "listen before talk" (LBT) function. The spectrum mask and the allowed power levels relating to the EN 302 208 regulations are illustrated in Fig. 6.2.

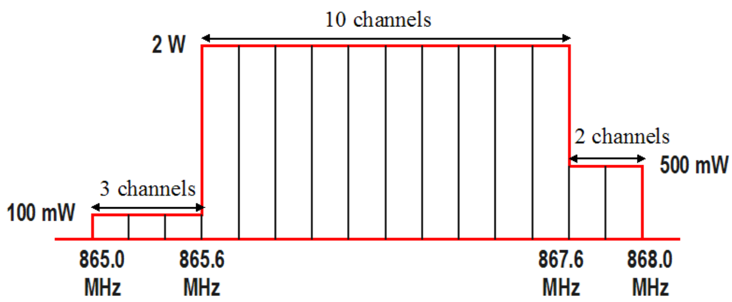

Figure 6.2 *UHF channel allocation and allowed power levels (EN 302 208 standard).*

- RFID in complex environments

Typically, read ranges from 2 to 5 meters are achieved with passive UHF RFID systems [62]. Many challenging features are required from the tag antenna to reach longer read distances. Firstly, the antenna has to be small, preferably low-profile, in order to be usable. Secondly, the fabrication has to be inexpensive, since RFID tags are designed to be disposable. In passive systems, a very good impedance match between the antenna and the RFID microchip is essential to at least sustain the power supply of the chip. A simple adjustment of its dimensions and an impedance bandwidth broad enough are a must. More important is that the matching has to hold in any environment because, in RFID applications, the tags are attached directly to different kind of objects. When the tags are mounted on objects made of reflecting (metallic cans) or absorbing materials (water bottles), they stop working properly (detuning, reduction of radiation resistance...). One of the best known solutions is to increase the distance between the tag and the conflicting material. Wide research has been carried out on RFID tag antennas in the UHF band. Most of the developed tag antennas are dipoles with different shapes, like folded [63] and meandered [64] dipoles. Their main disadvantage is that their impedance bandwidth is narrow and their performances strongly depend on the environment, which can detune the antenna. Microstrip patch [65] and PIFA [66] antennas are proposed as RFID tag antennas for operating in metallic environments because they already contain a metallic ground plane in their design. However, their performances as tag antennas are still too dependent on the dimensions of their metallic planes [65], [67]. By using the PIFA, reduced size tags, with smaller metallic planes, may be achieved, but generally at the cost of reduced tolerance to the environment [67]. In PIFA solutions for RFID tags, the microchip has to be attached vertically at the feed point. This makes the mounting of the chip on the tag difficult. To overcome such a problem, a compact slotted PIFA-type tag working at 911 MHz, mountable on metallic objects is presented in [68]. The microchip can be easily attached on the centre of the slot. The design proposed in [68] can be easily matched to most microchips by adjusting the slot parameters. The use of EBG ground planes in microstrip-tag designs is shown to be advantageous for improving the antenna efficiency, reducing the side lobe levels and increasing the antenna gain by reducing surface waves propagation [65]. A low-profile passive RFID tag antenna including an AMC in its design, working at 911 MHz, is presented in [69]. Although its matching performances are still dependent on the dimensions of a conducting plate placed below it, it is shown to provide reading distances from 2.4 m to 4.8 m in different environments.

The RFID tag presented in this dissertation is also based on the use of artificial magnetic conductors (AMC) in order to overcome the difficulty of working in environments containing metallic or absorbing materials. The AMC helps to isolate the tag antenna from the reflecting or absorbing material. The following sections describe the results of the work carried out towards the design of a platform-tolerant passive RFID system working at the European UHF RFID band (865 MHz to 868 MHz). First, a review of the operation principles of the passive RFID technology is provided. Some preliminary anechoic chambre measurements have been done in order to verify the usefulness of adding an AMC to the tag antenna design. Then, a new tag design is presented, by describing the role and features of the different elements composing it. In order to obtain a competitive tag, a modified design of reduced dimensions is shown in Section 6.4.5. After taking into account some fabrication aspects a final design, provided in Section 6.5, is created, ready for being tested. Finally, the input impedance of the final prototype presented in Section 6.5 has been measured to ensure good matching conditions.

6.2 Operation principles of passive RFID systems

When an electromagnetic traveling wave interacts with the inhomogeneities of the medium, the wave may be randomly dispersed in different directions. Such phenomenon is called *scattering* and tags in a RFID system achieve communications with a reader thanks to it. In sensor systems such as radar or RFID, a transmitter emits a radio-frequency (RF) electromagnetic wave, which will interact with the objects found along its way. Part of the energy that reaches the object is absorbed and the rest is randomly scattered or reflected in different directions. A small part of the reflected energy finds its way back to a receiver, which detects the object's scattered response. While radar technology uses this scatter phenomenon to measure the distance and position of distant objects, RFID systems take advantage of this phenomenon to transmit data from a tag to a reader. When the transmitter and the receiver is the same, scattering is referred to as monostatic or *backscatter*. *Modulated backscatter RFID systems* achieve communications through controlled changes of the tag's backscatter response. Variation of the tag's load impedance causes an intended mismatch in impedance between the tag's antenna and load. The mismatch due to changes in load impedance causes a different level of current to flow in the antenna's radiation resistance, which results in a different level of scattered or re-radiated power. Regardless of a match or mismatch, the tag's antenna will scatter some power as if it was radiating its own signal. The level of match or mismatch causes the level of scattered power to change. The tag's load impedance is altered versus time according to the data stored in the tag to modulate the scattered wave. The return scattered signal is detected and decoded by the reader. This form of communication is called *backscatter modulation*. A useful representation of an object's monostatic scattering characteristics is its backscattering cross section or radar cross section (RCS).

6.2.1 Scattering and radar cross section

The *radar cross section (RCS)* can be seen as a measure of how well an object scatters or reflects electromagnetic waves. It is expressed as an area like an antenna's efficient aperture. The RCS depends on different parameters, such as object size, shape, material, surface structure, but also wavelength and polarisation. Because of the dependence of the RCS on wavelength, scattering can be characterized by three regimes based on the ratio of the wavelength λ to body size. These regimes are the Rayleigh region (not to be confused with the far-field plane wave region), the resonant region and the optics region. In the rayleigh region, the wavelength is much greater than the body size. In the resonant region, the wavelength is on the order of the body size (between 1 and 10 wavelengths). In the optics region, the wavelength is much less than the body. The dominating scattering mechanisms are different in the different regions. In RFID systems we are concerned with scattering in the resonant region.

When analyzing modulated backscatter tags, we are mostly concerned with the scattering characteristics of the tag's antenna. Antennas are generally regarded as having two modes of scattering. On the one hand, the structural mode is the scattering that occurs because a given antenna has a certain shape, size and is made of a certain material. On the other hand, the antenna mode is the scattering that occurs because the antenna is designed to transmit RF energy and has a radiation pattern. That is, the antenna mode scattering results from the current that flows in the antenna's radiation resistance, which results in scattered or re-radiated power. Typically, the antenna mode scattering is the dominant factor in establishing the total scattered power, and it is related directly to the load impedance connected to the antenna. The RCS of the antenna mode scattering (σ) can be given in terms of the well-known familiar antenna parameters.

- Antenna scattering

The maximum received power that can be drawn from an antenna, given optimal alignment and correct polarisation, is proportional to the power density S of an incoming plane wave,

$$P_e = A_e S \tag{6.1}$$

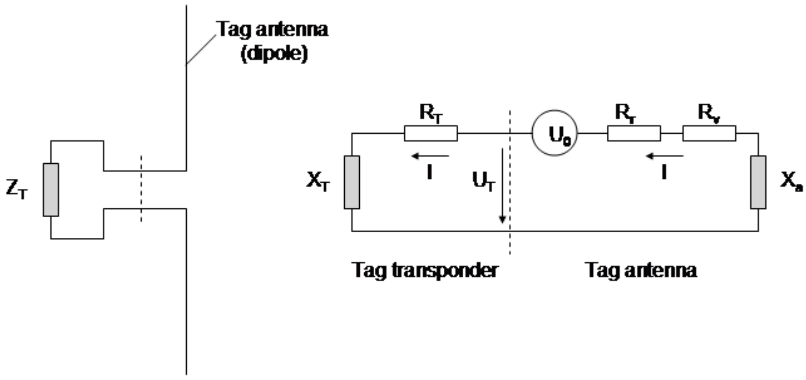

Figure 6.3 *Equivalent circuit of the tag antenna with a connected transponder.*

where A_e is the *effective aperture* of the antenna. The power P_e that passes through the effective aperture is absorbed and transferred to the connected terminating impedance Z_T (see Fig. 6.3) [62]. An effective voltage U_0 is induced in the antenna producing a current I through the antenna impedance Z_A and the load impedance Z_T. The *input impedance* of the antenna Z_A is made up of a complex resistance X_A, a loss resistance R_V and the so-called *radiation resistance* R_r.

$$Z_A = R_r + R_V + jX_A \tag{6.2}$$

The current I can be calculated from the ratio of the induced voltage U_0 to the series connection of the impedances Z_T and Z_A:

$$I = \frac{U_0}{|Z_T + Z_A|} = \frac{U_0}{\sqrt{(R_r + R_V + R_T)^2 + (X_A + X_T)^2}} \tag{6.3}$$

If the received power P_e transferred to Z_T is equal to

$$P_e = I^2 R_T \tag{6.4}$$

we obtain that

$$P_e = \frac{U_0^2 \, R_T}{(R_r + R_V + R_T)^2 + (X_A + X_T)^2} \tag{6.5}$$

and the effective aperture can be expressed as

$$A_e = \frac{P_e}{S} = \frac{U_0^2 \, R_T}{S\left[(R_r + R_V + R_T)^2 + (X_A + X_T)^2\right]} \tag{6.6}$$

If the antenna is operated using power matching and is also loss-free, that is, $R_T = R_r$, $X_T = -X_A$ and $R_V = 0$, the following simplification can be done:

$$A_e = \frac{U_0^2}{4SR_r} \tag{6.7}$$

As can be seen in Fig. 6.3, the current I also flows through the radiation resistance R_r of the antenna. The power converted within it corresponds to the power emitted from the antenna into space in the form of electromagnetic waves, and in the case of a receiving antenna this is the re-radiated or scattered power P_S, which can be calculated from:

$$P_S = I^2 R_r \tag{6.8}$$

Like for the effective aperture, the *scatter aperture* of the antenna, A_S, can be defined and calculated as:

$$\sigma = A_S = \frac{P_S}{S} = \frac{I^2 R_r}{S} = \frac{U_0^2 R_r}{S\left[(R_r + R_V + R_T)^2 + (X_A + X_T)^2\right]}, \tag{6.9}$$

which assumes identical current distributions on transmit and on receive.
If the antenna is again operated using power matching and is also loss-free, then we can simplify:

$$\sigma = A_S = \frac{U_0^2}{4SR_r} \tag{6.10}$$

Thus, in the case of the power matched loss-free antenna $\sigma = A_S = A_e$. This means that the antenna scatters the same amount of power that it absorbs from the incident wave.
The behavior of the scatter aperture A_S at different values of the terminating impedance Z_T is interesting. The scatter aperture can take any desired value in the range 0-4A_e (at the limit cases of Z_T). For the short-circuit case $(Z_T = 0)$ the A_S aperture is found to be:

$$\sigma_{max} = A_{Smax} = \frac{U_0^2}{S\,R_r} = 4A_e|_{Z_T=0} \tag{6.11}$$

The opposite limit case consists of an open-circuit connection, i.e. $Z_T \to \infty$. From Eq. 6.9 it is easy to see that the scatter aperture tends towards zero, as does the current I.

$$\sigma_{min} = A_{Smin} = 0|_{Z_T \to \infty} \tag{6.12}$$

The dependence of the scatter aperture σ on the relationship between Z_T and Z_A is used in RFID systems for the data transmission from the tag transponder to the reader. To this end, the transponder input impedance Z_T is altered in time with the data contained in it. Such procedure is known as *modulated backscatter*.

6.2.2 Link budget

Let us turn our attention to the operation of the tag when it is located in the interrogation zone of a reader. Fig. 6.4 shows a simplified model of a *backscatter system*. The reader emits an electromagnetic wave with radiated power P_1. The tag receives power P_e proportional to the field strength E, at distance R, where R is the distance between the tag and the reader. Power P_S is reflected by the tag antenna, from which power P_3 is again received by the reader at distance R from the tag.

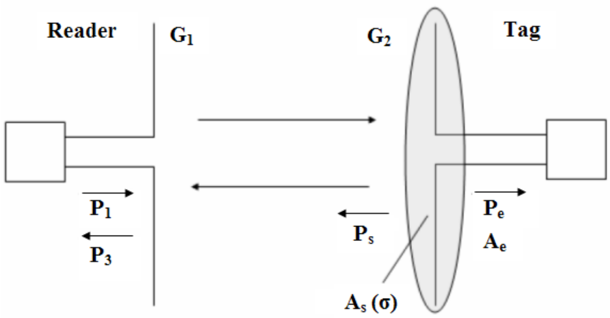

Figure 6.4 *Model of a RFID system: power flow through the entire system.*

- Reader to tag link budget

The power received by the tag when it is interrogated by the reader can be expressed as:

$$P_e = P_1 \frac{G_1 G_2 \lambda^2}{(4\pi R)^2} \tag{6.13}$$

We should introduce to this relation an impedance mismatch factor q given by [62]:

$$q = \frac{4R_A R_L}{(R_A + RL)^2 + (X_A + X_L)^2} \tag{6.14}$$

Hence the power delivered to the transponder resistance R_T can de derived as :

$$P_e = qP_1 \frac{G_1 G_2 \lambda^2}{(4\pi R)^2} \tag{6.15}$$

The polarization mismatch issues have to be also considered. If the receiving antenna has some polarization that is different from that of the incoming wave, only a fraction of the power will be received. For this reason, a polarization mismatch factor, p, is defined. Finally the power available at the tag chip load can be given by :

$$P_e = qpP_1 \frac{G_1 G_2 \lambda^2}{(4\pi R)^2} \tag{6.16}$$

where $G_1 P_1$ is defined as the ERP (Effective Radiated Power).

- Tag to reader link budget

The power scattered by the tag reaches the reader back. Then, the power received by the reader after interrogating the tag can be expressed as:

$$P_3 = \frac{P_1\, G_1^2\, \sigma\, \lambda^2}{(4\pi)^3\, R^4} \tag{6.17}$$

This expression corresponds to the monostatic radar equation, which evidences a fourth-exponential dependence on the read distance between the tag and the reader.

6.3 Preliminary anechoic chamber measurements

An RFID tag based on artificial magnetic conductors is here proposed to work close to metallic planes. The power backscattered by a planar dipole tag antenna is proved to be higher if we use an AMC surface to isolate the tag from the metallic plane. Preliminary anechoic chambre measurements have been done in order to verify the usefulness of adding an AMC to the tag antenna design. The experimental work presented in this section provides a good idea about the figures of merit of an RFID tag based on the use of AMC ground planes. The performance of RFID tags is usually evaluated in terms of detection distance. However, the detection distance does not only depend on the tag characteristics but also on the reader parameters (mainly, its sensitivity) [75]. A more quantitative manner to evaluate the performance of RFID tags is to monitor their radar cross-section (RCS) [76]. It can be obtained by simulating or measuring the power backscattered by the tag when illuminated with a plane wave or a transmitting antenna. So, the single-port measurement method described in [77] has been applied to measure the signal backscattered from a RFID tag based on an artificial magnetic conductor (AMC) consisting of an array of square patches above a back-grounded dielectric slab.

6.3.1 RFID tag design studied

The RFID tag design studied, based on an artificial magnetic conductor (AMC), is presented here. We want the envisaged design to work in the European UHF band (865.7 MHz to 867.7 MHz). However, in a first instance, due to some equipment limitations to measure at low frequencies we have worked at higher frequencies so far. This does not affect the phenomenology studied and the designs proposed here are easily up-scaled to lower frequencies. Actually, a prototype operating at the targeted RFID UHF band has also been fabricated and proved to behave as AMC at lower frequencies, as predicted by simulations.

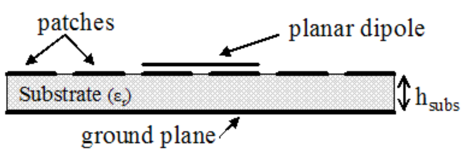

Figure 6.5 *Lateral view of the AMC-based tag design studied and proposed as platform-tolerant passive RFID tag.*

The RFID tag antenna analyzed is composed of a simple planar dipole placed above an AMC consisting of a finite array of square patches on a back-grounded dielectric slab (see Fig. 6.5). So far, the dipole has been made with conducting paper. It has been designed to resonate at a frequency around the AMC resonance. The tested AMC prototypes are composed of the unit cell shown in Fig. 6.6. The length of the patches is 13 mm and they are separated by a 2.5 mm gap. The substrate used is the Rogers RO4003C of 1.52 mm width and relative dielectric constant equal to 3.55. The etching of the copper film layer on the substrate is 35 μm. Such dimensions result in an AMC operating band around 5 GHz.

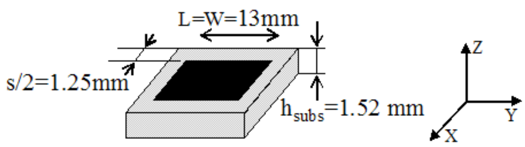

Figure 6.6 *Reference geometry of the unit cell of the AMC composing the tag under study.*

6.3.2 Backscattering measurement technique

The single-port measurement method described in [77] has been applied to measure the signal backscattered from the AMC-based RFID tag described in Section 6.3.1. The measurements here presented have been carried out at the UPC (Universitat Politècnica de Catalunya) facilites. The setup considered is shown in Figs. 6.7 and 6.8. The tested tag is illuminated with normal incidence by a ridged horn (left picture in Fig. 6.9).

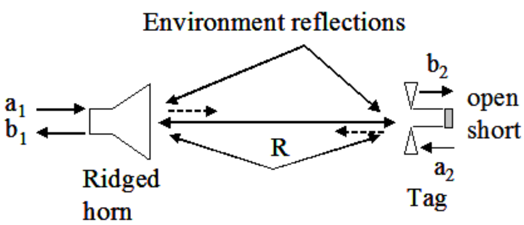

Figure 6.7 *Set up for backscattering measurement [78].*

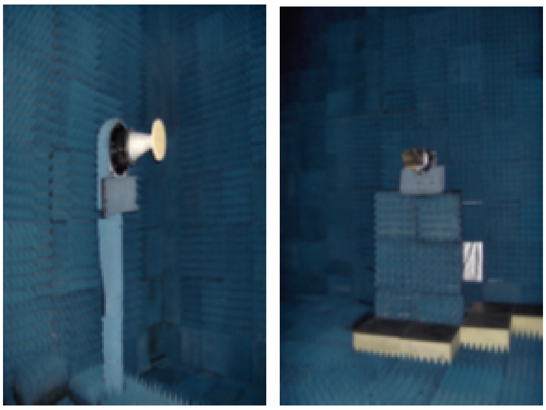

Figure 6.8 *Experimental setup in anechoic chamber. The tested tag is posted in the left and transmitting/receiving antenna in the right.*

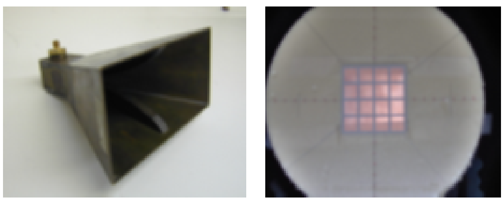

Figure 6.9 *View of the transmitter/receiver horn (left) and AMC of the tag antenna (right) used in the measurements.*

The backscattering measured at the input port of the calibrated horn (reader antenna) is composed of different contributions. On the one hand, the horn receives the power backscattered by the tag antenna, as well as the contribution from background reflections. The wave scattered by the tag can be decomposed in two different contributions. The first one, referred to as the structural mode of the scattered wave, corresponds to the power scattered by the tag antenna in complex conjugate match conditions $z_L = z_a^*$. It is worth noticing that it is independent from the load impedance z_L. The second contribution, called the antenna mode, depends on the load impedance z_L through the reflection coefficient due to the mismatch between the tag antenna impedance and the load impedance.

$$\Gamma(z_L) = \frac{z_L - z_a^*}{z_L + z_a} \tag{6.18}$$

Both, the structural and the antenna mode contributions, are complex quantities, which can therefore be represented in a complex coordinate plane [80]. Let us denote the structural mode of the scattered wave by S, the antenna mode by A, the environment contributions by E and the total backscattered field by T.

The reader of an RFID system has to determine the tag loading state from the measured response. For two impedance states z_{L1} and z_{L2}, a coherent detection method allows an easier differentiation of the two loading conditions [80]. Coherent detection obtains the backscattering level difference of the two loading states by $|T_{L1} - T_{L2}|$ rather than $|T_{L1}| - |T_{L2}|$ (incoherent detection), resulting in greater level differences and better detection performance. For the case of an ASK modulation with total mismatch in one state, the antenna is disconnected or shorted in one state, $\Gamma(z_L) = -1$ or $\Gamma(z_L) = 1$, and matched to the antenna impedance in the other state $\Gamma(z_L) = 0$. We remind that these reflection coefficients are those seen from the circuits, not from the wave side. It is worth noting that the level difference $|T_{L1} - T_{L2}|$ of these two states corresponds to the magnitude of the antenna mode component for the shorted or opened load conditions.

By measuring the power backscattered when the load connected to the tag antenna is both a short circuit ($Z_{L1} = 0$) and an open circuit ($Z_{L1} = \infty$), we can extract the antenna mode contribution obtained for these impedance states if we take the difference between both measurements $(T_{L1} - T_{L2})$. Fig.6.10 shows the vector representation for such a scheme. Comparing the antenna mode scattering obtained from the AMC-based tag and the one for a dipole placed at a certain distance from a PEC, gives us information about the usefulness of using an AMC to isolate the tag from a metallic plane. In order to make a fair comparison, the dipole should be placed at a distance equal to the AMC substrate thickness (see section below).

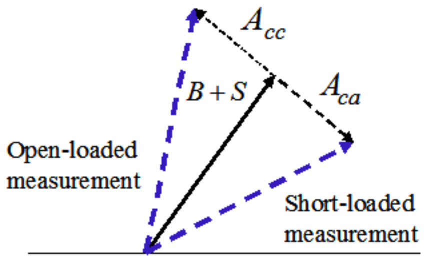

Figure 6.10 *Vector representation of the different backscattering contributions when the load of the tag is a short circuit and an open circuit [78].*

6.3.3 Measurement results

Fig. 6.11 and Fig. 6.12 contain the pictures of the AMC prototypes composing the tested tags. They have been fabricated using standard photo-etching techniques. They only differ by the number of unit cells. In that way, a study on the influence of the AMC size on the power backscattered by the tag has been carried out. Two square structures of different dimensions (2×2 and 4×4 unit cells) have been tested as well as a rectangular 4×2 one. We have observed that the antenna mode backscattering, understood as described in Section 6.3.2, is higher for the 2×2 case. So, the results discussed below refer to the RFID tag composed of the 2×2 AMC surface.

Fig. 6.12 also contains the mesh used for computing the reflection coefficient obtained when illuminating the surface with a plane wave coming from broadside. The commercial Feko software [40], a full-wave simulation tool based on the Method of Moments (MoM), has been used. Fig. 6.13 provides the phase of the simulated and measured reflection coefficient of the

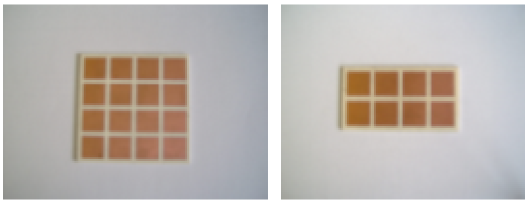

Figure 6.11 *Tested prototypes: 4×4 and 4×2 arrays of square patches above a back-grounded substrate.*

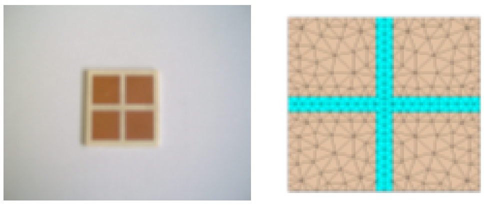

Figure 6.12 *Picture of the 2×2 tested prototype (left). Mesh of the simulated AMC surface shown to the left (right).*

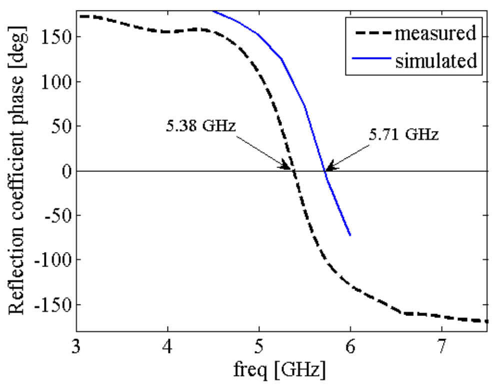

Figure 6.13 *Phase behaviour of the reflection coefficient for the 2×2 finite AMC under study.*

2×2 AMC prototype. The measurement setup described in Section 6.3.2 has been used. We can say that a relatively good agreement between measurements and simulations is observed. A 5.7% shift of the AMC resonance with respect to the predicted value is observed. As was revealed in Section 2.2.3, a 2×2 surface is small enough to notice the truncation effects of the finite AMC dimensions on the computation of the phase of the reflection coefficient.

Fig. 6.14 compares the antenna mode contribution to the backscattered power measured from a dipole placed just above the AMC and above a PEC with the same dimensions but at a distance equal to the height of the AMC (h_{AMC}) surface. At the AMC resonance, we observe a 6 dB improvement. Complementary measurements have been carried out when placing the dipole at different distances from both ground planes. We have observed that if the dipole is placed further from the planes, the benefit of using the AMC as a ground plane is smaller (the improvement observed decreases).

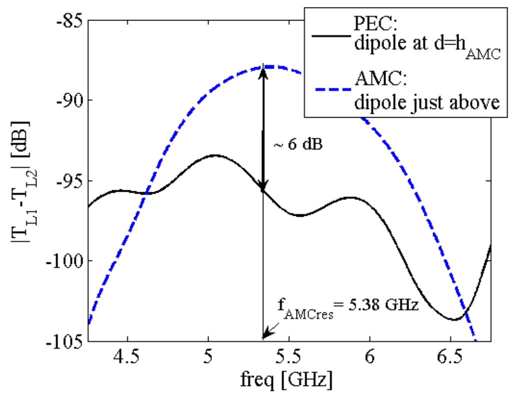

Figure 6.14 *Measured magnitude of the antenna mode backscattering for a dipole above the 2×2 finite AMC under study.*

6.4 New AMC-based tag

A new RFID passive tag based on metamaterials is proposed in this section. It consists on a meandered dipole inductively-fed by a rectangular loop, located horizontally above an AMC ground plane. The IC transponder containing the object data will be attached to the loop-feed. In the following sections, the IC chosen to compose the tag is presented and the different steps towards the conception of the new design are shown. At the end, a final design is provided.

6.4.1 UHF transponder IC ATA5590

The energy reflected by the tag antenna is modulated by changing the impedance presented by the microchip (IC) terminating the tag. An amplitude (ASK) or phase (PSK) modulation can be performed by changing the input resistance (Z_{in} real part) or input reactance (Z_{in} imaginary part), respectively. PSK modulation allows a more robust communication, resulting in greater communication distances between tag and reader. The UHF transponder that we have chosen for composing the tag is the IC ATA5590. When thinking about integrating the IC in the tag design, we need to know the input impedance that the IC requires for working properly. Such information can be found in [70].

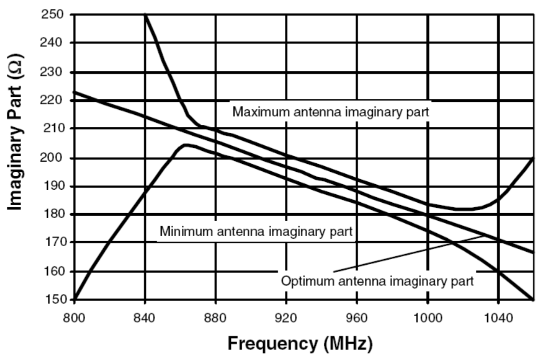

Figure 6.15 *Diagram for optimum antenna imaginary part [70].*

The IC ATA5590 uses PSK modulation, which consists in modulating the signal by alternating the phase of the data signal carrier between two phase states. These states depend on two discrete conditions determined by the IC impedance. As shown at page 3 of [70], by chosing an antenna impedance Z_{ant} with a low resistance and a reactance value in the middle of the reactances of

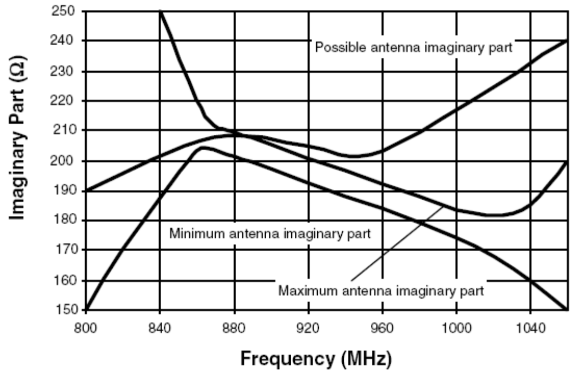

Figure 6.16 *Diagram for possible antenna imaginary part [70].*

the two states impedances, a maximum phase difference between the states is achieved. Diagrams for optimal and recommended matching between the tag antenna and the IC are provided in [70]. The optimum imaginary part of the antenna is matched to the average value of both imaginary states of the IC (see Fig. 6.15). But this optimum antenna imaginary part is only theoretical and can not be achieved in real life. The diagram in Fig. 6.16 contains a suggested and possible approximation of the optimum antenna's imaginary part [70]. We want the envisaged design to work in the European UHF band (865.7 MHz to 867.7 MHz). For the case of the ATA5590 chip at 868 MHz, the chip impedance for its operating states is equal to $Z_{IC1} = 6 - j202$ and $Z_{IC2} = 7 - j216$, which means an antenna impedance matched to $Z_{ant} = 6 + j209$ for an optimum tag operation at 868 MHz. It is worth noting that a deviation of 4Ω from the optimum imaginary part of the Z_{ant} reduces the operation range of the IC by approximately 10% [70]. The real part of Z_{ant} should be between 10Ω and 15Ω for having good IC operation [70]. Lower or higher values would also reduce its operation range.

6.4.2 Tag antenna fed by inductive coupling

Good impedance match between the tag antenna and the IC is needed to activate the tag, on the one hand, and to maximise the read range, on the other hand. An inductively coupled feed method to design UHF RFID tag antennas is presented in [71]. It is a simple and easy way to match an antenna impedance to an arbitrary IC impedance Z_{IC}, because the real and imaginary parts of Z_{ant} can be adjusted almost independently. So, we have followed the same kind of design as the one studied in [71]. It consists of a small rectangular loop and of a radiating body (a meandered dipole in that case), which are coupled inductively. Fig. 6.17 contains a picture of such a design. The red small line seen in the picture connects the loop terminals that would be directly connected to the chip and represents the excitation voltage applied to carry out the simulations. The dimensions are the ones of the dipole studied in [71]. The length L of the dipole is 80 mm and the loop is 7.7 mm $\times$ 14 mm (a $\times$ b). The width of the loop is the same as the meander dipole width w_d, which is equal to 1.5 mm.

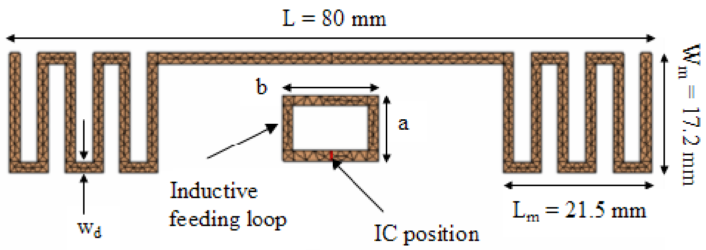

Figure 6.17 *Proposed tag antenna design consisting of a meander dipole fed by inductive coupling.*

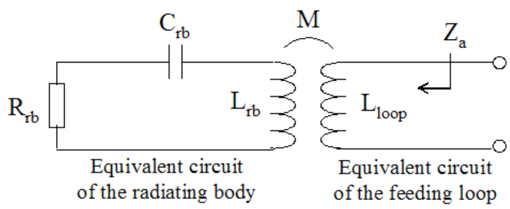

Figure 6.18 *Equivalent circuit for a inductively-fed dipole.*

The strength of the coupling is controlled by the distance between the loop and the radiating body (the meander dipole) as well as the shape of the loop [71]. The inductive coupling is modelled by a transformer (see Fig. 6.18).

As stated in [71], at the resonant frequency f_0 of the radiating body, the resistance $R_{a,0}$ of the input impedance of the antenna Z_a, depends only on M (the mutual inductance between the radiating body and the feed loop). Meanwhile, the input reactance $X_{a,0}$ is dependent only on L_{loop} (the self-inductance of the feed loop). Thus, once the loop is designed ($X(a,0)$ determined), the $R_{a,0}$ can be adjusted mainly by the distance between the loop and the radiating body, resulting in an easy way to match the antenna impedance to an arbitrary complex impedance within a certain range [71]. Since the reactance $X_{a,0}$ only depends on the self-inductance of the loop, the antenna can get very inductive.

6.4.3 Inductively-coupled tag antenna placed above an ideal PMC ground plane

We want our tag design to contain an artificial magnetic conductor (AMC) as a ground plane to isolate the tag antenna from metal planes when working in metallic environments. In order to see if the principles of the inductively-coupled meandered dipole presented above are preserved in presence of an AMC, we have firstly added an infinite ideal PMC to the design (see Fig. 6.19) and studied the performances obtained. So far, the dimensions of the meander dipole and loop are the ones from [71], described in Section 6.4.2, and the PMC is placed below the coupled-dipole design at 0.3 mm.

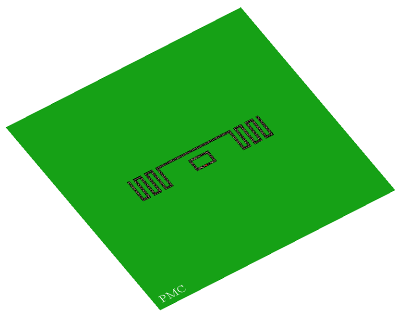

Figure 6.19 *Tag design above an ideal infinite PMC.*

Fig. 6.20 provides the input impedance characteristics obtained for the meander dipole and the loop separately, both located at 0.3 mm from the PMC. It is worth noting that the features observed are the ones expected for a meander dipole and a loop operating without ground plane. For the case of the loop, we can observe a resonance roughly close to ($L_{loop} = \lambda/2$). When

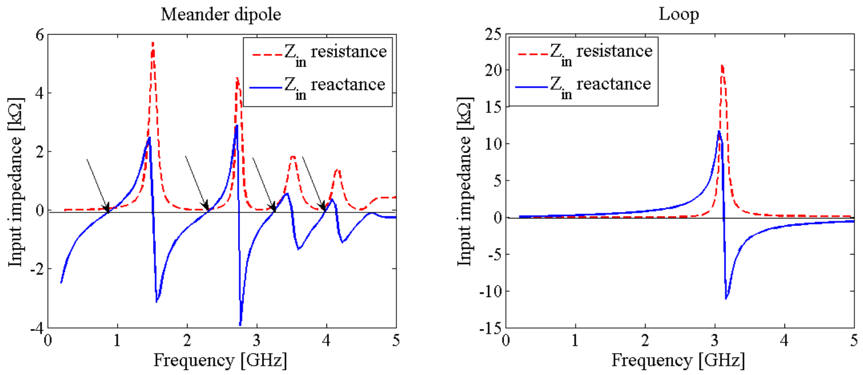

Figure 6.20 *Input impedance characteristics of a meander dipole (left) and a loop (right) placed at 0.3 mm above an infinite ideal PMC.*

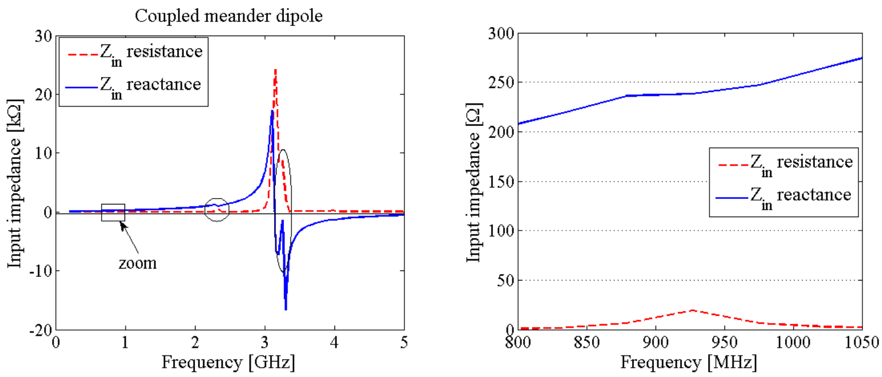

Figure 6.21 *Left: input impedance characteristics of an inductively coupled meander dipole placed at 0.3 mm above an infinite ideal PMC. Right: zoom around the lowest dipole resonance.*

both structures are combined to create the inductively-coupled dipole, the input impedance performance provided in Fig. 6.21 is obtained. It can be seen as the loop impedance characteristics with the inductive coupling effect described in [71], appearing at the resonant frequencies (reactance crossing zero) of the meander dipole. It is interesting to observe that the coupling effect is stronger at the dipole resonant frequencies that are closer to the loop resonance. To better appreciate such effect, a zoom close to the first dipole resonance, which is near the European UHF RFID band, is shown to the right in Fig. 6.21. This is the same kind of behavior and phenomenology observed for the coupled meandered dipole without ground plane [71]. Hence, including a PMC ground plane in the tag design does not disturb the behavior and performances expected from the inductively coupled dipole. This means that, in presence of a PMC, it is still possible to match the tag antenna and the IC impedances easily, by adjusting the loop dimensions and its distance to the dipole. These are encouraging results towards the design of the AMC-based tag antenna. The next section provides some preliminary results concerning the design of the inductively-fed tag when it is backgrounded by an artificial magnetic conductor (AMC).

6.4.4 Inductively-coupled tag antenna placed above a finite AMC ground plane

The AMC used as ground plane consists of a 2x2 finite array of square patches on a backgrounded dielectric slab (see Fig. 6.22). It has been designed to resonate at the European UHF band. As it can be seen in the unit cell depicted in Fig. 6.23, the length of the square patches is 91 mm. They are separated by a gap, *s*, equal to 2.5 mm. The substrate that supports them is the RO4003C of 1.52 mm width and relative dielectric constant equal to 3.55.

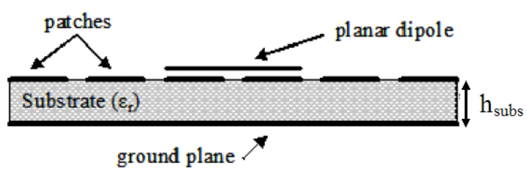

Figure 6.22 *Lateral view of the AMC-based tag design studied.*

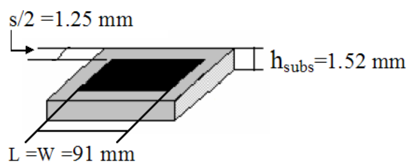

Figure 6.23 *Unit cell and dimensions of the AMC used.*

Fig. 6.24 presents the phase of the reflection coefficient obtained by simulation with FEKO for such a surface. The zero cross has been finely adjusted to 866.6 MHz (the center frequency of the RFID band of interest). We have put the same meander dipole studied in Section 6.4.3, at 0.3 mm from the 2x2 AMC surface. If we look at the input impedance presented in Fig. 6.24, we observe a behavior similar to the one expected from the inductively coupled dipole alone and when placed above an ideal PMC (as described in Section 6.4.3). So, the presence of an AMC ground plane preserves the coupled loop effect. Therefore, by adjusting the dimensions of the feed-coupled meander dipole we should be able to achieve the required input impedance for a proper IC operation, meaning a $Z_{ant} = 6 + j209$ at 868 MHz when working with the IC ATA5590 (see Section 6.4.1).

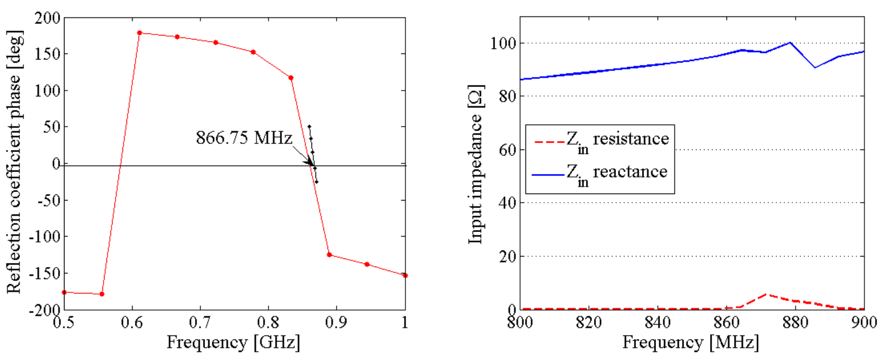

Figure 6.24 *Left: phase of the reflection coefficient obtained for a 2x2 AMC designed to work at the European UHF RFID band. Right: input impedance characteristics of an inductively coupled meander dipole placed at 0.3 mm above the 2x2 AMC mentioned before.*

6.4.5 Reduction of the tag dimensions

The dimensions of the design proposed in Section 6.4.4, working at 866.7 MHz (the Europe UHF RFID central frequency) are $18.45\,cm \times 18.45\,cm$. Such dimensions are normal for antennas operating at low frequencies, which are related to huge wavelengths. But if we want our prototype to be useful and competitive as a tag antenna for RFID applications, we should reduce its size, which specially concerns the reduction of the AMC surface. Some literature has been reviewed, looking for existing compact AMC designs. In [72] and [73], we can find different compact shapes obtained with different design methodologies. However, they are complicated shapes and the results provided concern infinitely periodic surfaces. It means that for finite surfaces we have to expect bigger dimensions than the ones provided in such works. From the study presented in [74], we were confident that patches with a spiral shape would allow us to reduce the AMC dimensions of a factor of 2. However, for finite AMC surfaces, the AMC resonances achieved are higher, resulting in bigger dimensions than the ones provided in [74].

6.4.5.1 Reduction of the AMC horizontal dimensions

In order to reduce the AMC horizontal dimensions, we have inserted a gap in the patch edges, along the direction of the current flow ($\hat{y}$), in order to lengthen the path of the travelling current wave. Fig. 6.25 shows a unit cell of the new AMC together with the mesh of a 2×2 surface. The patch is square with length pt_{len} equal to 91 mm and the separation between patches (g) is the same in both directions ($\hat{x}$ and $\hat{y}$) and equal to 2.5 mm. The width and dielectric constant of the substrate filling the space between the patches and the background plane are equal to 1.52 mm and 3.55, respectively.

As it can be seen in Fig. 6.26, the presence of the gap produces a shift of the frequency resonance f_{res} of the AMC to lower frequencies, which means a reduction of the electrical dimensions of the AMC surface. By varying the dimensions of the gap (gp_w and gp_{len}), the frequency resonance f_{res} at which the structure behaves as an AMC (artificial magnetic conductor) can be tuned. Fig. 6.27 provides the phase curve of the reflection coefficient obtained for different dimensions of the patch gap. It is observed that increasing both the width and the length of the patch gap, reduces even more the horizontal di-

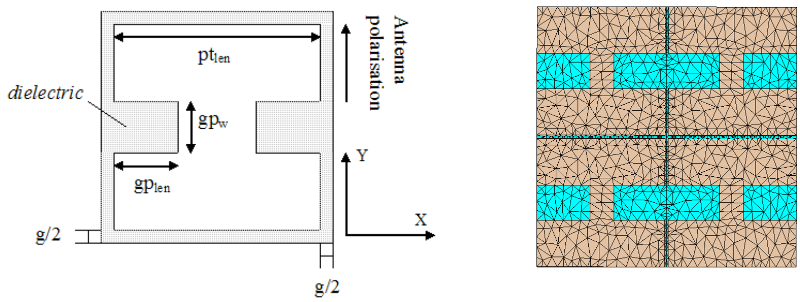

Figure 6.25 *Left: parameters and unit cell shape of the new AMC design proposed. Right: mesh of a 2×2 AMC surface composed of the unit cell pictured in the left.*

mensions of the AMC. A gap with $gp_w = 25mm$ and $gp_{len} = 31.6mm$ provides an AMC design reduced by a factor of 0.61, w.r.t. the initial AMC working at the RFID band (866.7 MHz central frequency). It is worth noticing that even if the bandwidths achieved for AMC operation are narrow (see Figs. 6.26 and 6.27), they are large enough to cover the 0.32% bandwidth needed (from 865.6 MHz to 867.6 MHz) for european UHF RFID applications. An operating bandwidth around 1% is envisaged to take into account possible fabrication imprecisions.

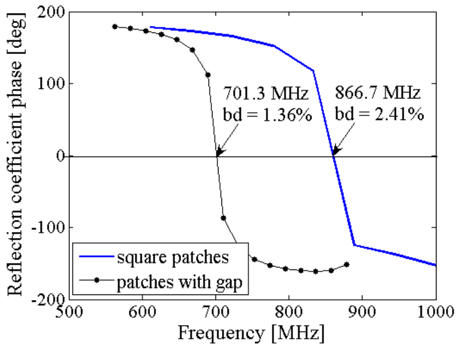

Figure 6.26 *Effect on the AMC f_{res} when adding a gap on the patches of the AMC surface.*

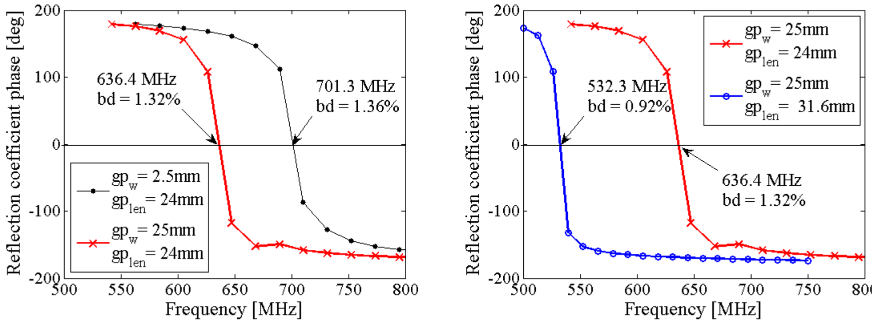

Figure 6.27 *Effect observed on the AMC behavior when increasing the width (to the left) and the length (to the right) of the patch gap.*

- Patches-ground plane connection

Despite the dimensions reduction already obtained, a reduction factor around 0.25 is necessary to achieve a competitive design. By increasing the dielectric permitivity of the material contained between the patches and the background plane, we can reduce the resonant frequency by a factor of $\sqrt{\epsilon_{r1}}/\sqrt{\epsilon_{r2}}$, where $\epsilon_{r1} < \epsilon_{r2}$. Fig. 6.28 shows the additional f_{res} shift obtained if we replace the substrate with $\epsilon_r = 3.55$ by one with $\epsilon_r = 10.2$.

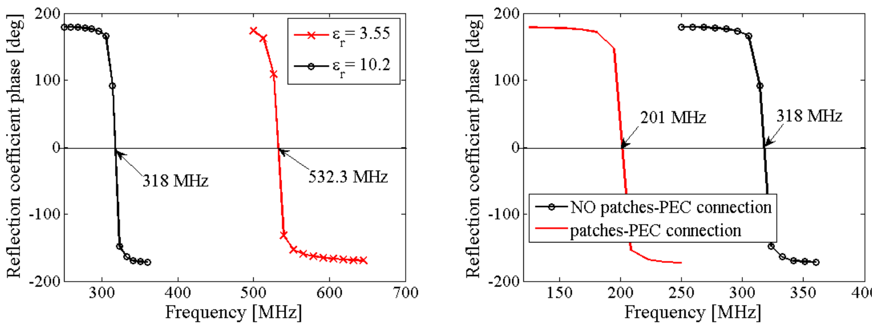

Figure 6.28 *Effect on the AMC f_{res} obtained when increasing the dielectric permitivity of the substrate (left) and when connecting the patches to the ground plane at the end sides of the AMC (right).*

If moreover the patches are connected to the background plane of the finite AMC at its end sides in the $\hat{y}$ direction (the antenna current flow direction), the patch electrical length becomes longer again. Fig. 6.29 contains a picture of the AMC surface with the connected patches. They are easily connected to the back plane by a metal sheet covering the lateral sides of the substrate in the direction of the current flow. Fig. 6.28 also provides the phase curve of the reflection coefficient obtained before and after connecting the patches to the ground plane of the AMC. A further shift to lower frequencies is obtained again. So finally, a reduction factor equal to 0.23 has to be applied to resize the design resonating at 201 MHz (see right picture in Fig. 6.28) to operate again at the RFID band (866.7 MHz central frequency). With a further adjustment of the dimensions of the scaled prototype, a 4.26 cm $\times$ 4.26 cm AMC surface is achieved. Such dimensions are small enough to consider our design competitive for RFID applications.

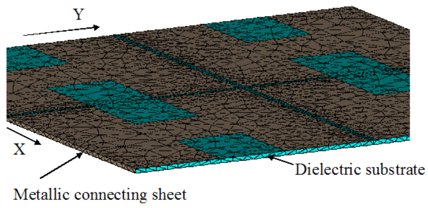

Figure 6.29 *View of the 2 $\times$2 AMC surface showing the end side connection between the patches and the backgrounding PEC plane.*

Fig. 6.30 contains the reflection coefficient curve obtained for the scaled design. The length of the patches and gap between them are now equal to 20.67 mm and 1.22 mm, respectively. The substrate width and relative dielectric constant are 1.28 mm and 10.2. At this point, it is already interesting to study the effect of a metallic plane placed below the AMC. To this end, we have observed the behavior of the reflection coefficient phase curves obtained for an AMC with a finite background plane bigger than the surface containing the patches that compose the AMC (see the mesh in Fig. 6.30). The results for a metallic plane of dimensions equal to $\lambda/4 \times \lambda/4$ and $\lambda/5.35 \times \lambda/5.35$, where λ corresponds to the wavelength at the RFID UHF center frequency

(866 MHz), are also provided in Fig. 6.30. It is seen that having larger metallic ground planes at the back of the surface does not affect the AMC behavior and resonance of the structure. Hence, the new AMC structure can be considered as a platform-tolerant design. It is worth noticing that the relative bandwidth achieved for AMC operation is 1.42%, considering a $\pm 45^\circ$ reflection coefficient phase criteron.

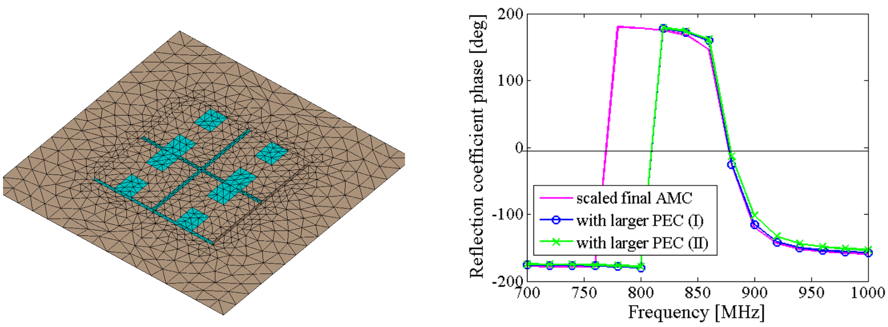

Figure 6.30 *Left: mesh of the tag AMC with a finite metallic plane at its back. Right: comparison of the reflection coefficient phases obtained for the final AMC proposed and the design with larger backgrounding PEC planes.*

6.4.5.2 Reduction of the tag antenna dimensions

Once the AMC has been reduced, the coupled-feed meandered dipole initially proposed and studied in Section 6.4.4 for composing the tag antenna is too large. It takes up to 80 mm $\times$ 17.2 mm and the new reduced AMC is 42.6 mm $\times$ 42.6 mm. A modified smaller version of such dipole has been designed so that it fits in the AMC area. Fig. 6.31 contains the new dipole design, which is composed of wider meanders, resulting in a smaller dipole length dip_{len}. The linear dipole in the middle of the design has been shifted to the middle of the meanders width. This enables a centered design when placing the meander dipole above the AMC (as it can be seen in Figure 6.32). The dimensions of the new meander dipole tag are 35.34 mm length (dip_{len} parameter in the picture) and 32.65 mm width (m_w). The rectangular loop that composes the design is 20.04 mm $\times$ 9.77 mm ($L_y \times L_x$). The length of the linear dipole in the middle is 21.45 mm, its width is equal to 1.46 mm (the same as the meanders one) and the loop's width is equal to 0.98 mm. The dipole is placed at 1.7 mm above the AMC. These dimensions are already adjusted to have a design well matched to the impedance of the IC ATA5590 at 868 MHz, the IC operating frequency for working at the European UHF RFID band.

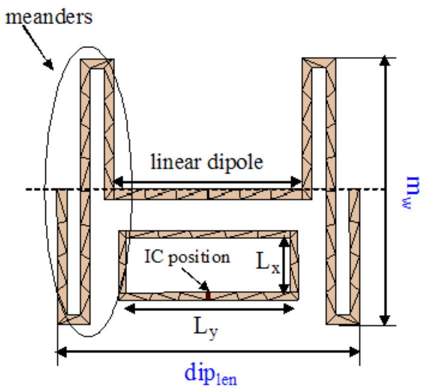

Figure 6.31 *New meander dipole design composing the tag antenna.*

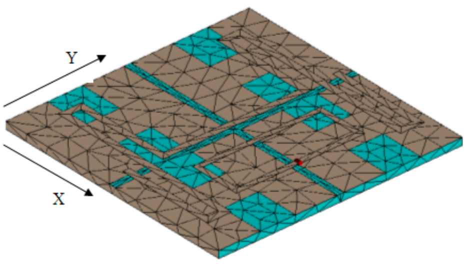

Figure 6.32 *New meander dipole tag at 1.7 mm height from the AMC design of reduced dimensions studied in Section 6.4.5.1.*

Like for the original inductively-fed dipole, a complex input antenna impedance Z_{ant} can be achieved, and its real and imaginary parts can be adjusted easily. By adjusting the dimensions of the new meandered dipole, particularly the loop dimensions and its distance to the dipole, the antenna input impedance can be matched to $Z_{ant} = 6 + j209$ for an optimum ATA5590 chip operation (see Section 6.4.1). Fig. 6.33 shows the input impedance characteristic obtained for the new dipole design, placed at 1.7 mm distance above the final AMC design provided in Section 6.4.5.1 (see Fig. 6.32). As was described in Section 6.4.4 and as can be seen here again, the coupling loop effect is preserved in presence of the AMC, which makes it possible to match the AMC tag design to a desired complex input impedance.

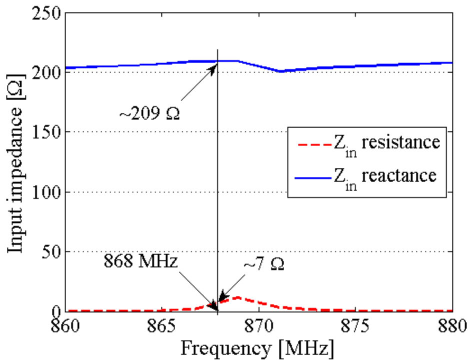

Figure 6.33 *Input impedance characteristic of the new meander dipole placed at 1.7 mm above the AMC presented in Section 6.4.5.1.*

6.4.6 Effectiveness of the AMC-based tag

In order to verify again (see Section 6.3 for a preliminary experimental verification) the advantage of using an AMC ground plane instead of a simple PEC to design the tag, we have computed the input impedance characteristics of the design presented in Section 6.4.5.2 (the previous one), but without the patches of the AMC. The dimensions remain the same. The resulting design consists on an inductively-fed dipole placed above a back-grounded dielectric (see Fig. 6.34). We have preserved the dielectric layer to make the fairest possible comparison. Fig. 6.35 provides the input impedance obtained for such a design. We observe from the input reactance that the inductive coupling effect provided by the dipole's loop, described in Section 6.4.3 or [71], is not present anymore, which is not the case if we use an AMC ground plane (see

Section 6.4.5.2 or the measurement results in Section 6.5). Moreover, as expected for an antenna closely spaced from a PEC ($\lambda/117.5$ in this case), the antenna resistance is very low. It has been reduced from $\sim$7 Ω (see Fig. 6.33) to $\sim$15 mΩ at the operation frequency (see right picture in Fig. 6.35), when the AMC has been replaced by the back-grounded dielectric. This clearly shows the cancellation effect produced by the image currents induced on the PEC when the antenna is very close to it. Consequently, this supports the fact that the AMC allows us to achieve a substantial radiation resistance with a lower profile.

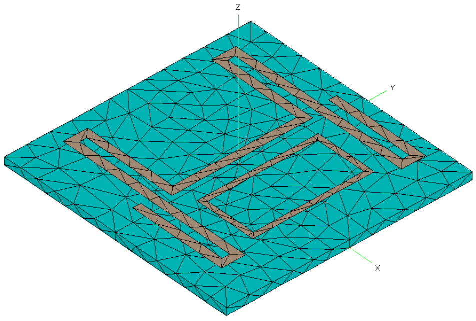

Figure 6.34 *Meander dipole from Section 6.4.5.2, placed at 1.7 mm above a back-grounded dielectric.*

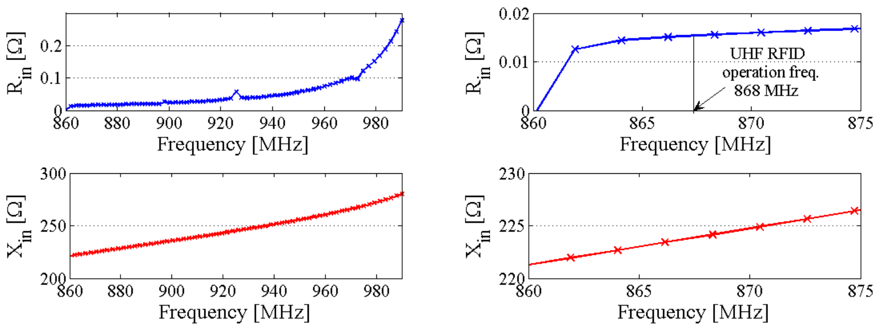

Figure 6.35 *Input impedance characteristic of the meander dipole from Section 6.4.5.2, placed at 1.7 mm above a back-grounded dielectric. A zoom centered on 868 MHz is provided to the right.*

6.5 Final prototype measurements

The integration of the IC in the tag design is not a simple process that can be carried out in our laboratory. The first tag prototypes contain the IC in a TSSOP10 package. This package introduces an additional parallel capacitance that decreases the imaginary part of the IC impedance. Then, the input impedance of the tag has to be matched to a new impedance, $Z_{ant} = 11 + j152$, as suggested in [70]. Moreover, an additional substrate is added between the meander antenna and the AMC surface (see Fig. 6.36) in order to ease the fabrication process of the tag. So far, air filled the space between the dipole and the AMC, but the small dimensions of the meander dipole make the fabrication process difficult if there is no substrate supporting the dipole. The substrate introduced between the meander dipole and the AMC is the RO3003 with thickness equal to 1.52 mm and dielectric constant equal to 3. It enables a further reduction of the tag profile. The total height of the tag is now $\lambda/123.4$, where λ corresponds to the wavelength at 868 MHz. The horizontal dimensions of the tag are 42.6 mm $\times$ 42.6 mm, corresponding to $\lambda/8 \times \lambda/8$ at 868 MHz.

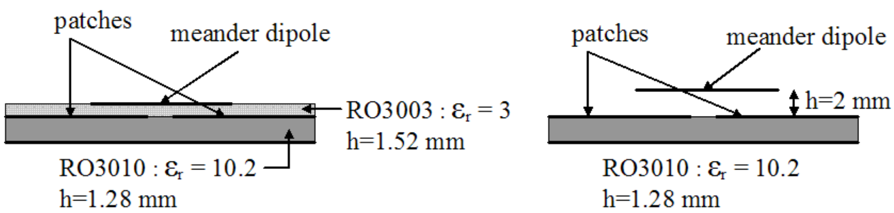

Figure 6.36 *Profile of the final tag with (left) and without (right) a dielectric substrate supporting the meander dipole above the AMC surface.*

The design of the dipole has been slightly modified in order to match its input impedance to the impedance of the TSSOP10 package. It is worth noting that it is more difficult to match the antenna with the additional substrate supporting the dipole. Fig. 6.37 provides the new inductively-fed dipole together with its dimensions. The meanders are now all situated on the same side of the loop, and the whole dipole is wider. The AMC surface remains the same as the one designed in Section 6.4.5.1. Fig. 6.37 also provides a picture of the prototype fabricated for test. Thanks to the symmetry of the design, we could fabricate the half of it and use a metallic sheet to create its image, in order to ease the measurement procedure. In this way, the balanced feed of the tag, placed in the middle of the AMC surface, can be replaced by a coaxial cable at the edge of the half design.

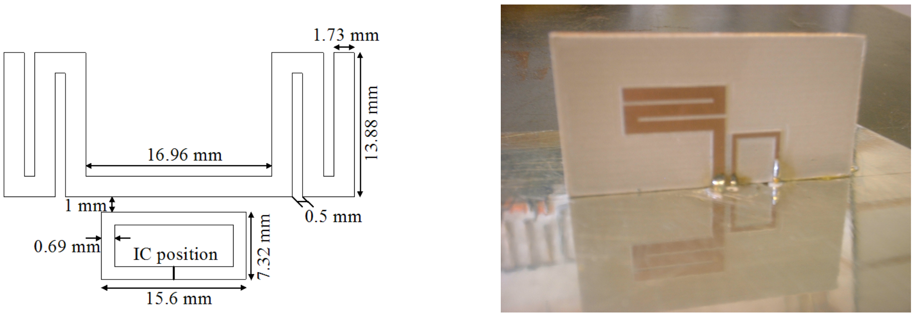

Figure 6.37 *Left: new meander dipole design. Right: view of the tag prototype.*

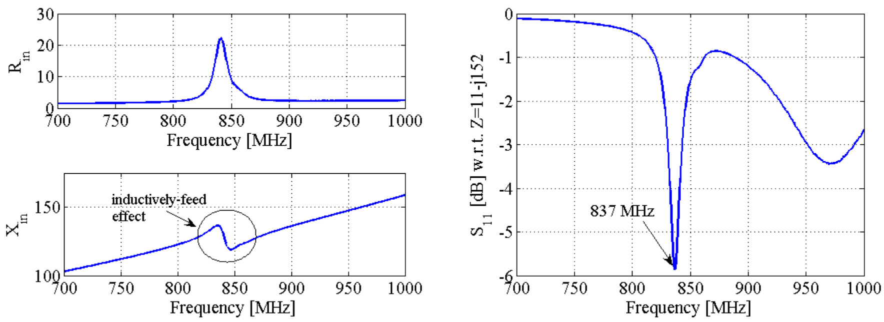

Figure 6.38 *Input impedance (left) and S_{11} coefficient (right) measurements obtained for the prototype shown in Fig. 6.37*

The input impedance of the prototype shown in Fig. 6.37 has been measured and the results are presented in Fig. 6.38. The inductive coupling effect achieved with the feeding loop, described in Section 6.4.3, is clearly observed. This means that the AMC ground plane plays its role correctly, providing a low-profile tag mountable on metallic sheets. If we look at the input reflection coefficient obtained w.r.t. $Z_{TSSOP10} = 11 - j152$, we observe a resonance at 837 MHz instead of 868 MHz, the targeted frequency. The input impedance measured at 837 MHz is equal to $16 + j136\,\Omega$. The dimensions of the dipole should be adjusted to tune the tag at 868 MHz and to obtain a better impedance matching. Nevertheless, these are very encouraging measurement results towards the design of a tag based on the use of an AMC to make it operable on metallic objects.

6.6 Preliminary work toward an even smaller tag

We wondered if we could reduce even more the size of the AMC in order to have an even smaller tag. Some further simulations have been performed to this end. Fig. 6.39 shows the mesh of a modified version of our already reduced design proposed in Section 6.4.5.1. In the same idea of increasing the length of the path followed by the currents induced on the AMC patches, we have added two new inclusions in the interior side of the patches, in the antenna current flow direction ($\hat{y}$). The dimensions of the resulting unit cell are provided in Fig. 6.39. The central patch gap in the middle of the new inclusions has been removed (see the unit cell picture in Fig. 6.39) because we have observed that this produces a further reduction of the AMC size.

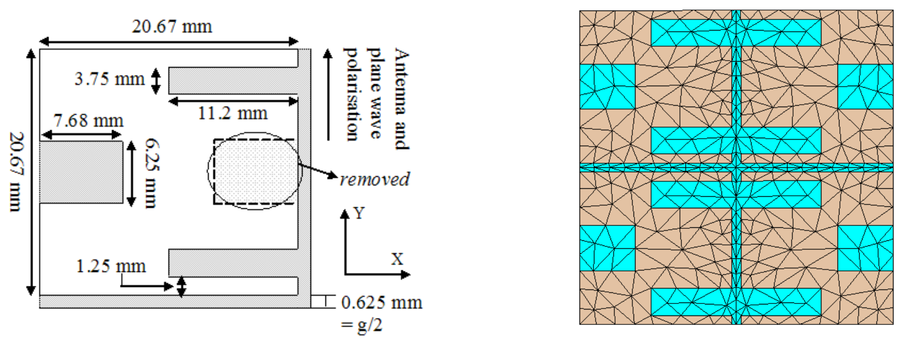

Figure 6.39 *Left: unit cell shape of the new AMC design proposed. Right: mesh of a 2×2 AMC surface composed of the unit cell pictured in the left.*

The phase curve of the reflection coefficient obtained when a $\hat{y}$-polarized plane wave impinges the new surface is shown in Fig. 6.40. We observe a significant shift toward lower frequencies w.r.t. the phase curve for the already reduced design provided in Section 6.4.5.1. This means that a factor equal to 0.84 has to be applied to the dimensions of the AMC (the ones provided in Fig. 6.39) to retune its resonance to 868 MHz. This would result in a design about 35.8 mm$\times$35.8 mm instead of 42.6 mm $\times$ 42.6 mm. These are encouraging results towards the design of a very small and compact tag, but reached such point of reduction we should also study and define which are the minimum tag dimensions necessary to continue having a platform-tolerant design. It is also worth noting that a smaller AMC design will require a new smaller version of the inductively-fed meander dipole.

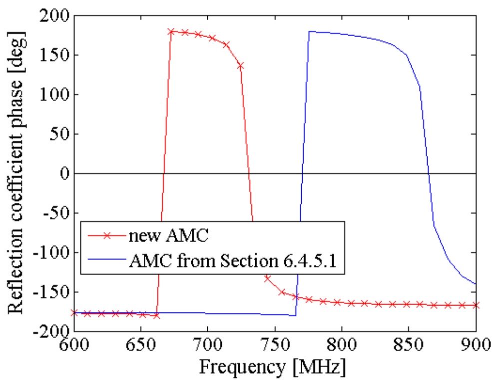

Figure 6.40 *Phase of the reflection coefficient for the new AMC and the one proposed in Section 6.4.5.1*

Conclusions

7

A growing interest in a new kind of periodic structures, often called "metamaterials", has been observed over the last decade. Our interest in this kind of structures was focused on their use as AMC (artificial magnetic conductor) ground plane configurations. Given the narrow bandwidth of AMC surfaces, their application remains a challenge for wideband antennas. The antenna-AMC combination can be optimized to maximize the bandwidth. The design of a compact AMC ground plane is also a challenge. In this work, we presented a new AMC design of small lateral dimensions and used it to design an RFID tag mountable on metallic objects.

7.1 Wideband low-profile antennas

A low-profile antenna based on the use of an AMC ground plane has to be designed taking into account that there exists a coupling between the antenna and the AMC. When an antenna is placed above an AMC, the antenna-AMC combination has to be analysed instead of each single element independently. AMC surfaces are often characterized by the phase curve of the reflection coefficient obtained when a plane wave incides on them. But, it is worth noting that an AMC acts as PMC only for plane propagating waves, and for a limited range of incidence angles, which is not a fair approximation for the fields associated to an antenna placed close to an AMC. The fields near an AMC surface consisting of an array of square patches have been analyzed, paying special attention to the evanescent waves scattered by the surface. It has been evidenced that these evanescent waves are stronger, with a non-negligible vertical component at small distances from the surface, near the resonance frequency of the AMC. For the case of a finite AMC surface, the evanescent waves are going to be reflected by the edges, resulting in strong array truncation effects also near the AMC resonance. These reactive fields are going to affect the input impedance of an antenna placed close to the AMC surface. We have observed some unexpected additional resonances for a planar bow-tie dipole placed above an AMC ground plane. It has been shown that they depend on the size of the AMC and on the distance between the antenna and the AMC ground plane, which corroborates the influence of the evanescent waves on the antenna input impedance. Then, a trade-off should be found between the proximity of the antenna to the artificial ground plane on one side, and the immunity of the antenna reactance to the evanescent waves scattered by the ground plane, on the other side.

The AMC surface also has an influence on the radiation performances obained for an antenna placed above it. It has been observed that the radiation patterns split at broadside such that the directivity strongly decreases in this direction when we work close to the AMC resonance. This limits the useful operation bandwidth, i.e. the bandwidth at which good radiation and matching conditions are achieved at the same time. It has been suggested in [17] that the useful operation bandwidth corresponds to the band where the reflection phase of the AMC is within the range $90^\circ \pm 45^\circ$ instead of $0^\circ \pm 90^\circ$. In the present work we have proposed two different solutions to overcome the radiation problems. The first one concerns the design of the antenna that is placed above the AMC surface. The second one concerns the design of the AMC ground plane.

A new antenna configuration has been proposed as an alternative to the planar bow-tie dipole antenna. It consisted of two planar dipoles stacked above the AMC ground plane. They resonated at two close frequencies at different distances from the AMC ground plane. The largest dipole, resonating at the AMC resonance, was placed close to the surface to obtain a lower profile than if it were placed on top. The initial idea of having dipoles of different lengths did not finally help to improve the broadside directivity over the whole input impedance bandwidth. Then, a design of dipoles with identical lengths was proposed. The distance of the dipoles to the AMC determined the performances achieved. The closer to the AMC the higher directivities obtained, but narrower impedance bandwidths are achieved. A prototype providing more than 8.12 dB over a 17.15% bandwidth was presented. The profile of the design was $\lambda_{min}/4.64$, where λ_{min} corresponds to the wavelength of the highest operation frequency. The profile was defined from the ground plane backing the whole design, i.e. antenna and AMC combination, and measured as a factor of λ_{min} because it represents the worst profile of the operation bandwidth. Good radiation patterns were obtained over the whole useful band. However, the proposed solution did not solve the problem for designs with desired bandwidths wider than 20%.

A new non-periodic structure acting as an AMC and as a leaky-wave antenna at the same time was designed and studied, to recover the broadside directivity near and beyond the AMC resonance. The structure consists of a rectangular array of patches with different lengths along the E-plane direction. The surface was cut in the H-plane direction in order to avoid the propagation of surface waves in this direction. The central patches of the surface allow us to take advantage of the AMC properties to create low-profile designs, while the patches of different sizes away from the center help to create a guiding structure with homogeneous phases along successive patches. An eigenmodes analysis for an AMC consisting of a periodic array of square patches and for the new non-periodic structure was carried out. It revealed the appearence of a bound mode corresponding to a 180° phase shift at the frequency at which the splitting patterns problem was most dramatic, for a double-dipole antenna placed horizontally above the periodic AMC. The excitation of such a trapped mode resulted in surface currents induced on the AMC patches that contributed destructively to the radiation patterns. It is worth noting that having trapped modes traveling along the AMC surface implies evanescent fields near the AMC, which coincides with the evanescent waves study mentioned before. It was shown that such bound modes were shifted to higher frequencies (out of the operation band) when the periodic AMC surface was cut in the H-plane and made non-periodic by decreasing the length of the patches in the E-plane direction. In addition, leaky waves radiating with a β/α ratio approaching the condition $\beta/\alpha \leq 1$ were supported by the new non-periodic surface. These leaky waves, radiating at small angles from the broadside direction with wider beams than their tilt, contributed constructively to the broadside directivity. The new AMC surface allowed us to design an antenna with a broadside directivity better than 9.2 dB, close to the maximum achievable value in view of the antenna size, over a 32.65% impedance bandwidth. The total height of the antenna was $\lambda_{min}/6.7$, where λ_{min} corresponds again to the wavelength at the highest operation frequency.

A very simple method for the computation of the periodic Green's function (G_p), evaluated for complex phase shifts, was developed since we needed to deal with leaky waves in the modal analysis concerning the new AMC structure. It consists of extrapolating the G_p's calculated spectrally at different distances from the array plane, to the G_p for smaller distances, where the spectral G_p computation is very slowly convergent. Before extrapolating, the contribution of the closest source points is spatially extracted in order to produce smoother functions. After the singularities extraction, a polynomial extrapolation is performed. Finally, the extracted sources contributions are reintroduced to obtain the complete G_p. Accuracies of the order of 10^{-11}, $10^{-7.5}$ and $10^{-3.7}$ were easily obtained with a fourth-polynomial extrapolation, for different combinations of real and complex phase shifts ψ_x, ψ_y: both real, only one of them complex (ψ_y), and both complex, respectively.

7.2 Compact AMC design for RFID applications

One of the goals of our work was to design an RFID tag able to work on metallic objects, without being short-circuited, with the help of an AMC ground plane. The usefulness of including an AMC in the tag design to isolate it from a metallic plate was proven experimentally. But having a compact AMC ground plane was essential for having a competitive RFID tag. Then, a new AMC surface of reduced dimensions (42.6 mm $\times$ 42.6 mm) was designed. It supported an inductively-fed meander dipole above it that helped to obtain the complex input impedance required to activate the microchip (IC) terminating the tag. It is worth mentioning that good impedance match between the tag antenna and the IC, which is highly capacitive, is necessary to ensure the correct operation of the tag. It was shown that the operation principles of the meander dipole were preserved in presence of the AMC ground plane. A prototype was fabricated in our laboratory and its input impedance measured. The inductive coupling effect achieved with the feeding loop of the meander dipole was clearly observed. The dimensions of the dipole should be adjusted to tune the tag exactly at 868 MHz (the european UHF RFID operation frequency), instead of the 837 MHz resonance obtained for the measured prototype. However, the results obtained were very encouraging measurement results towards the design of an AMC-tag operable on metallic objects. It is worth noting that the profile of the tag is $\lambda/123.4$, where λ corresponds to the wavelength at 868 MHz, the European UHF RFID operation frequency.

7.3 Further prospects

The new aperiodic AMC structure proposed in this dissertation opens new perspectives in the design of wideband low-profile antennas. Its finite dimensions and its capability to avoid surface waves makes it a promising solution to create operative wideband antennas with low profiles. The size of the surface could be further reduced by using other shapes for the patches composing it, which would provide attractive compact antenna designs. Its behavior as leaky wave guiding surface makes it also suitable for the design of leaky wave antennas.

A very simple method was proposed for the computation of the periodic Green's function when it is evaluated for complex phase shifts. It may help us to ease the analysis of leaky waves concerning periodic structures.

Some further work can still be carried out concerning the design of the AMC-tag. Measurements concerning the test of a complete RFID system would provide a further knowledge about the performances, in terms of reading distance achievable with the new tag. A more flexible design that could be placed on curved surfaces, provided with different soldering points to accommodate chips with different impedances, would enlarge its range of applications.

List of acronyms

A

AMC: Artificial Magnetic Conductor
DNG: Double Negative Material
EBG: Electromagnetic Bandgap
EFIE: Electric Field Integral Equation
ERP: Effective Radiated Power
HIS: High Impedance Surface
IC: Integrated Circuit
LHM: Left-Handed Material
LWA: Leaky-Wave Antenna
MoM: Method of Moments
NIM: Negative-Index Material
PEC: Perfect Electric Conductor
PMC: Perfect Magnetic Conductor
RCS: Radar Cross Section
RF: Radio-frequency
RFID: Radio-frequency Identification
UHF: Ultra High Frequency

List of publications

B

B.1 Conference papers

- R.M. Mateos, P. Ferrer, C. Craeye and X. Dardenne, "Reactive fields above an artificial PMC", *Proc. of the 2005 IEEE Symposium on Antennas and Propagation*, Washington, July 2005.

- R.M. Mateos, C. Craeye and G. Toso, "Design of a non-periodic artificial magnetic conductor to obtain a high-gain wideband low-profile antenna", *Proc. of the First European Conference on Antennas and Propagation*, Nice, November 2006.

- R.M. Mateos and C. Craeye, "Eigenmode analysis of an AMC ground plane for wideband high-gain antennas", *Proc. of the 2007 International Conference on Electromagnetics in Advanced Applications*, Torino, September 2007.

- R.M. Mateos, J.M. González, C. Craeye and J. Romeu, "Backscattering measurement from a RFID tag based on artificial magnetic conductors", *Proc. of the Second European Conference on Antennas and Propagation*, Edinburgh, November 2007.

- F. Muge Tanyer-Tigrek, R.M. Mateos and C. Craeye,"Design of a AMC plane for a unidirectional, low-profile tulip antenna", *Proc. of the Third European Conference on Antennas and Propagation*, Berlin, March 2009.

B.2 Journal papers

- R.M. Mateos, C. Craeye and G. Toso, "High-gain wideband low-profile antenna", *Special Issue on Metamaterials of Microwaves Optical and Technology Letters*, 48, pp.2615-2619, 2006.

Bibliography

[1] Simovski, C.R., Belov, P.A. and Sailing He, "Backward wave region and negative material parameters of a structure formed by lattices of wires and split-ring resonators", *IEEE Trans. Antennas and Propag.*, Vol.51, pp.2582-2591, Oct. 2003.

[2] Dardenne X. and Craeye C., “Analysis of infinite and finite broadband low-profile arrays", at the 26th ESA Antenna Workshop on Satellite Antenna Modelling and Design Tools, Noordwijk, The Netherlands, 12-14 November 2003.

[3] Best S.R., “Improving the performance properties of a dipole element closely spaced to a PEC ground plane", *IEEE Antennas and Wireless Propag. Lett.*, Vol.3, pp.359-363, 2004.

[4] Sievenpiper D., Zhang L., Broas R., Alexopolous N.G., and Yablonovitch E., “High-impedance electromagnetic surfaces with a forbidden frequency band", *IEEE Trans. Microwave Theory and Techniques*, Vol.47, pp.2059-2074, Nov. 1999.

[5] Best S.R. and Hanna D.L., “Design of a broadband dipole in close proximity to an EBG ground plane", *IEEE Anten. and Propag. Magazine*, Vol.50, pp.52-64, Dec. 2008.

[6] http://www.feko.co.za

[7] Veselago V.G., "The electrodynamics of substances with simultaneously negative values of ε and μ,", *Soviet Physics Uspekhi*, Vol.10, pp.509-514, Jan. 1968.

[8] Pendry J.B., "Negative refraction makes a perfect lens", *Physical Review Lett.*, Vol.85, pp.3966-3969, Oct. 2000.

[9] Smith D.R., Schurig D., Rosenbluth M., Schultz S., Ramakrishna S.A. and Pendry J.B., "Limitations on subdiffraction imaging with a negative refractive index slab", *Applied Physics Lett.*, Vol.82, pp.1506-1508, March 2003.

[10] Yang F. and Rahmat-Samii Y. "Microstrip antennas integrated with electromangentic band-gap(EBG) structures: a low mutual coupling design for array applications", *IEEE Trans. Antennas and Propagation*, Vol.51, pp.2936-2946, Oct. 2003.

[11] Gonzalo R., de Maagt P. and Sorolla M., "Enhanced patch-antenna performance by suppressing surface waves using photonic bandgap substrates", *IEEE Trans. Microwave Theory and Techniques*, Vol.47, pp.2131-2138, Nov. 1999.

[12] Zhang Y., von Hagen J., Younis M., Fischer C. and Wiesbeck W., "Planar artificial magnetic conductors and patch antennas", *IEEE Trans. Antennas and Propagation*, Vol.51, pp.2704-2712, Oct. 2003.

[13] Fei-Ran Yang, Kuang-Ping Ma, Yongxi Qian and Itoh T., "A novel TEM waveguide using uniplanar compact photonic-bandgap (UC-PBG) structure", *IEEE Trans. Microwave Theory and Techniques*, Vol.47, pp.2092-2098, Nov. 1999.

[14] Goussetis G., Feresidis A.P. and Vardaxoglou J.C., "Tailoring the AMC and EBG characteristics of periodic metallic arrays printed on grounded dielectric substrate", *IEEE Trans. Antennas and Propagation*, Vol.54, pp.82-89, Jan. 2006.

[15] Burghignoli P., Lovat G., Capolino F., Jackson D.R. and Wilton D.R., "Leaky modes on a grounded wire-medium slab", *Microw. Symp. 2007, IEEE/MTT-S Int.*, pp.1663-1666, June 2007.

[16] Fei-Ran Yang, Kuang-Ping Ma, Yongxi Qian and Itoh T., "A uniplanar compact photonic-bandgap (UC-PBG) structure and its applications for microwave circuit", *IEEE Trans. Microwave Theory and Techniques*, Vol.47, pp.1509-1514, Aug. 1999.

[17] Yang F. and Rahmat-Samii Y., "Reflection phase characterizations of the EBG ground plane for low profile wire antenna applications", *IEEE Trans. Antennas and Propagation*, Vol.51, pp.2691-2703, Oct. 2003.

[18] Kern D.J., Werner D.H., Monorchio A., Lanuzza L. and Wilhelm M.J., "The design synthesis of multiband artificial magnetic conductors using high impedance frequency selective surfaces", *IEEE Trans. Antennas and Propagation*, Vol.53, pp.8-17, Jan. 2005.

[19] Hosseini M., Pirhadi A. and Hakkak M., "Design of a novel AMC with little sensitivity to the angle of incidence and very compact size", *Antennas and Propagation Society International Symposium (APS) 2006*, pp.1939-1942, Albuquerque, July 2006.

[20] Simovski C.R., de Maagt P. and Melchakova I.V., "High-impedance surfaces having stable resonance with respect to polarization and incidence angle", *IEEE Trans. Antennas and Propagation*, Vol.53, pp.908-914, March 2005.

[21] Kim Y., Yang F. and Elsherbeni A.Z., “Compact artificial magnetic conductor designs using planar square spiral geometries", *Progress in Electromagnetics Research*, *PIER 77*, pp.43-54, 2007.

[22] Ferrer P.J., Gonzalez-Arbesu J.M. and Romeu J., “Design and measurement of a spiral-cell PMC for metamaterial applications", *Antennas and Propagation Society International Symposium (APS) 2006*, pp.31-34, Albuquerque, July 2006.

[23] Feresidis A.P., Apostolopoulos G., Serfas N. and Vardaxoglou J.C., “Closely coupled metallodielectric electromagnetic band gap (CCMEBG) structures formed by double layer dipole and tripole arrays", *IEEE Trans. Antennas and Propagation*, Vol.52, pp.1149-1158, May 2004.

[24] Abhari R. and Eleftheriades G.V., “Metallo-dielectric electromagnetic bandgap structures for suppression and isolation of the parallel-plate noise in high-speed circuits", *IEEE Trans. Microwave Theory and Techniques*, Vol.51, pp.1629-1639, June 2003.

[25] Coccioli R., Fei-Ran Yang, Kuang-Ping Ma and Itoh T., “Aperture-coupled patch antenna on UC-PBG substrate", *IEEE Trans. Microwave Theory and Techniques*, Vol.47, pp.2123-2130, Nov. 1999.

[26] Kuang-Ping Ma, Hirose K., Fei-Ran Yang, Qian Y. and Itoh T., “Realisation of magnetic conducting surface using novel photonic bandgap structure", *Electron. Lett.*, Vol.34, No.21, Oct. 1998.

[27] Rumsey V., “Frequency independent antennas", *New-York and London: Academic Press*, 1966.

[28] Mushiake Y., “Self-Complementary Antennas", *IEEE Antennas Propagat. Magazine*, Vol.34, pp.23-29, Dec. 1992.

[29] McGrath D.T. and Baum C.E., “Scanning and Impedance Properties of TEM Horn Arrays for Transient Radiation", *IEEE Trans. Antennas Propagat.*, Vol.47, pp.469-473, March 1999.

[30] Dardenne X. and Craeye C., “Analysis of infinite and finite broadband low-profile arrays", *Proc. of the 26th ESA Antenna Technology Workshop on Satellite Antenna Modelling and Design Tools*, pp.167-174, Noordwijk, November 2003.

[31] Pozar D.M., *Microwave Engineering*, Addison-Wesley, Reading, 1990, pp.726.

[32] Harrington R.F., "Field computation by moment methods", *IEEE Press Series on Electromagnetic Wave Theory*, 1993.

[33] Lee R.T. and Smith G.S., “A design study for the basic TEM horn antenna", *IEEE Antennas and Propagat. Magazine*, Vol.46, pp.86-92, Febr. 2004.

[34] Mateos R.M. and Craeye C., “Wideband low-profile antennas", *final report, ESA/ESTEC contract n° 17576/03/NL/LvH*, Nov. 2005.

[35] Dardenne X., “Method of Moments simulation of infinite and finite periodic structures and application to high-gain metamaterial antennas", *Ph.D dissertation*, March 2007.

[36] Dardenne X. and Craeye C., “Method of moments simulation of infinitely periodic structures combining metal with connected dielectric objects", *IEEE Trans. Antennas and Propag.*, Vol.56, pp.2372-2380, August

2008.

[37] Simovski C.R., de Maagt P. and Melchakova I.V., "High-impedance surfaces having stable resonance with respect to polarization and incidence angle", *IEEE Trans. Antennas and Propagat.*, Vol.53, pp.908-914, March 2005.

[38] Best S.R. and Reid R., "The application of RF MEMS and metamaterials in the design of advanced antenna systems", *slides presented at NATO Workshop on EBG and MEMS technologies for antennas and front-ends*, Siena, Oct. 2005.

[39] Akhoondzadeh-Asl L., Kern D.J., Hall P.S. and Werner D.H., "Wide-band dipoles on electromagnetic bandgap ground planes", *IEEE Trans. on Antennas and Propagation*, Vol.55, pp.2426-2434, Sept. 2007.

[40] Akhoondzadeh-Asl L. and Hall P.S., "Broadband dipole antenna on electromagnetic bandgap ground planes", *Proc. of the European Conf. on Antennas and Propagation 2006*, Nice, Nov. 2006.

[41] Mateos R.M. and Craeye C., "Wideband Low-Profile Antennas", *final report, ESA/ESTEC contract n° 17576/03/NL/LvH*, Nov. 2005.

[42] Yang H-Y.D., Kim R. and Jackson D.R., "Design Consideration for Modeless Integrated Circuit Substrates Using Planar Periodic Patches", *IEEE Trans. Microw. Theory Tech*, Vol. 48, pp.2233-2239, Dec. 2000.

[43] Joannopoulos J., Meade R. and Winn J., "Photonic Crystals: Molding the Flow of Light", *NJ:Princeton Univ. Press*, Princeton, 1995.

[44] Craeye C. and Dardenne X., "Element pattern analysis of wide-band arrays with the help of a finite-by-infinite array approach", *IEEE Trans.*

Antennas and Propagation, Vol.54, pp.519-526, Feb. 2006.

[45] Jorgenson R.E. and Mittra R., “Efficient calculation of the free-space periodic Green’s function", *IEEE Trans. Antennas and Propagation*, Vol.38, pp.633-642, May 1990.

[46] Rao S.M., Wilton D.R. and Glisson A.W., "Electromagnetic scattering by surfaces of arbitrary shape", *IEEE Trans. Antennas and Propagation*, Vol.30, pp.409-418, May 1982.

[47] Ip A. and Jackson D.R., “Radiation from cylindrical leaky waves", *IEEE Trans. Antennas and Propagation*, Vol.38, pp.482-488, April 1990.

[48] Das N.K. and Pozar D.M.,“Full-wave spectral-domain computation of material, radiation, and guided wave losses in infinite multilayered printed transmission lines", *IEEE Trans. on Microw. Theory and Techniques*, Vol.39, pp.54-63, Jan. 1991.

[49] Lovat G., Burghignoli P. and Jackson D.R., “Fundamental Properties and Optimization of Broadside Radiation From Uniform Leaky-Wave Antennas", *IEEE Trans. Antennas and Propagation*, Vol.54, pp.1442-1452, May 2006.

[50] Sievenpiper D.F., "Forward and backward leaky wave radiation with large effective aperture from an electronically tunable textured surface", *IEEE Trans. Antennas and Propagation*, Vol.53, pp.236-247, Jan. 2005.

[51] F. Muge Tanyer-Tigrek, R.M. Mateos and C. Craeye,"Design of a AMC plane for a unidirectional, low-profile tulip antenna", *Proc. of the Third European Conference on Antennas and Propagation*, Berlin, March 2009.

[52] Valerio G., Baccarelli P., Burghignoli P. and Galli A., “Comparative Analysis of Acceleration Techniques for 2-D and 3-D Green’s Functions in Periodic Structures Along One and Two Directions", *IEEE Trans. Antennas and Propagation*, Vol.55, pp.1630-1643, June 2007.

[53] Valerio G., Baccarelli P., Burghignoli P. and Galli A., “3-D Green’s Functions in 1-D Periodic Structures: a Comparative Analysis of the Acceleration Techniques", *Proc. of the European Conf. on Antennas and Propagation 2006*, Nice, Nov. 2006.

[54] Singh S., Richards W.F., Zinecker J.R. and Wilton D.R., “Accelerating the Convergence of Series Representing the Free Space Periodic Green’s Function", *IEEE Trans. Antennas and Propagation*, Vol. 38, pp.1958-1962, Dec. 1990.

[55] Craeye C., Smolders A.B., Schaubert D.H. and Tijhuis A.G., “An Efficient Computation Scheme for the Free Space Green’s Function of a Two-Dimensional Semiinfinite Phased Array", *IEEE Trans. Antennas and Propagation*, Vol. 51, pp.766-771, April 2003.

[56] Singh S. and Singh R., “On the Use of ρ-Algorithm in Series Acceleration", *IEEE Trans. Antennas and Propagation*, Vol. 39, pp.1514-1517, Oct. 1991.

[57] Capolino F., Wilton D.R. and Johnson W.A., “Efficient Computation of the 2-D Green’s Function for 1-D Periodic Structures Using the Ewald Method, *IEEE Trans. Antennas and Propagation*, Vol. 53, pp.2977-2984, Sept. 2005.

[58] Mathis A.W and Peterson A.F., “A Comparison of Acceleration Procedures for the Two-Dimensional Periodic Green’s Function", *IEEE Trans. Antennas and Propagation*, Vol. 44, pp.567-571, Apr. 1996.

[59] William H. Press, "Numerical Recipes in C", *The Art of Scientific Computing*, Second Edition, Cambridge University Press, Chapter 3.5, pp. 120.

[60] Craeye C. and Capolino F., "Accelerated Computation of the Free Space Green's Function of Semi-Infinite Phased Arrays of Dipoles", *IEEE Trans. Antennas and Propagation*, Vol. 54, pp.1037-1040, March 2006.

[61] http://www.rfidexchange.com

[62] Finkenzeller K., "RFID Handbook", 2nd ed. New York: Wiley, 2003.

[63] Qing X., Yang N.. "A folded dipole antenna for RFID", *Proc. of the IEEE Ant. and Propag. Int. Symp. 2004*, pp.97-100, June 2004.

[64] Marrocco G., Fonte A. and Bardati F., "Evolutionary design of miniaturized meander-line antennas for RFID applications", *Proc. of the IEEE Ant. and Propag. Int. Symp. 2002*, pp.362-365, June 2002.

[65] Ukkonen L., Sydnheimo L. and Kivikoski M., "Effects of Metallic Plate Size on the Performance of Microstrip Patch-Type Antennas for Passive RFID", *IEEE Ant. and Wireless Propag. Lett.*, Vol.4, pp.410-413, Dec. 2005.

[66] Hirvonen M., Pursula P., Jaakkola K. and Laukkanen K., "Planar inverted-F antenna for radio frequency identification", *Electronics Lett.*, Vol.40, pp.848-850, July 2004.

[67] Huynh M.-C. and Stutzman W., "Ground plane effects on planar inverted-F antenna (PIFA) performance", *IEE Proc. Microw., Antennas and Propag.*, Vol.150, pp.209-213, Aug. 2003.

[68] Kwon H. and Lee B., "Compact slotted planar inverted-F RFID tag mountable on metallic objects", *Electronics Lett.*, Vol.41, pp.1308-1310, Nov. 2005.

[69] Dongho K. and Yeo J., "Low-profile RFID tag antenna using compact AMC substrate for metallic objects", *IEEE Ant. and Wireless Propag. Lett.*, Vol.7, pp.718-720, 2008.

[70] "ATA5590 Tag Antenna Matching: Application Note", ATMEL.

[71] Son H.-W. and Pyo C.-S., "Design of RFID tag antennas using an inductively coupled feed", *Electronics Letters*, Vol.41, No.18, Sept. 2005.

[72] Kern D.J., Werner D.H., Monorchio A., Lanuzza L. and Wilhelm M.J., "The design synthesis of multiband artificial magnetic conductors using high impedance frequency selective surfaces", *IEEE Trans. on Antennas and Propagation*, Vol.53, pp.8-17, Jan. 2005.

[73] Hosseini M., Pirhadi A. and Hakkak M., "Design of a novel AMC with little sensitivity to the angle of incidence and very compact size", *IEEE Int. Symposium on Antennas and Propagation*, pp.1939-1942, July 2006.

[74] Y. Kim, F. Yang and A.Z. Elsherbeni, "Compact artificial magnetic conductor designs using planar square spiral geometries", *Progress In Electromagnetics Research*, PIER 77, pp.43-54, 2007.

[75] Nikitin P.V. and Rao K.V.S., "Performance Limitations of Passive UHF RFID Systems", *Proc. of the IEEE Ant. and Propag. Int. Symp. 2006*, pp. 1011-1014, July 2006.

[76] Lee B. and Kwon H., "Meander Line RFID Tag at UHF Band Evaluated with Radar Cross Sections", *Proc. of the Asia-Pacific Microw. Conf. 2005*,

Dec. 2005.

[77] Nikitin P.V. and Rao K.V.S., “Theory and Measurement of Backscattering from RFID Tags", *IEEE Anten. and Propag. Magazine*, Vol.48, pp. 212-218, 2006.

[78] Serrano R., Romeu J., Blanch S. and Jofre L., ´´Evaluation of two novel non-invasive measurement methods for small antennas", *Proc. of the European Conference on Ant. and Propag. 2006*, Nov. 2006.

[79] Ruck G.T., Barrick D.E., Stuart W.D. and Krichbaum C.K., “Radar Cross Section Handbook", *Plenum Press*, 2, 1970.

[80] Li H-J., Lo C-Y. and Chen J-Y., “Impedance Loading State Determination for UHF Passive RFID Applications", *Proc. of the IEEE Ant. and Propag. Int. Symp. 2007*, June 2007.